Design Optimization and Fatigue Analysis of Laser Stake Welded Connections

Project Report for the
Structural Response of Hybrid Ship Connections Subjected to Fatigue Load Project

by

Anshuman Singh, Graduate Research Assistant
Senthil S. Vel, Ph.D., Associate Professor and Principal Investigator
Vincent Caccese, Ph.D., P.E., Professor and Co-Principal Investigator

Prepared for:

Office of Naval Research
800 N Quincy St.
Arlington VA. 22217-5660

Grant No. N00014-05-1-0735
Dr. Roshdy G.S. Barsoum,
Program Manager

University of Maine
Department of Mechanical Engineering
Orono, ME 04469-5711

June 2008

Report No. C-2004-015-RPT-02

ABSTRACT

This report summarizes research on the design and fatigue analysis of laser-stake welded connections performed at the University of Maine from January 2006 to December 2007 for the Structural Response of Hybrid Ship Connections Subjected to Fatigue Loads (HSCF) project. The HSCF project, funded by the Office of Naval Research, is part of a joint effort between the University of Maine, Lehigh University of Bethlehem, PA and Applied Thermal Sciences Inc. (ATS) of Sanford, ME an engineering research and development consulting company with extensive experience in implementation of laser welding for ships.

Laser welding for ship structural connections is a maturing technology that offers much promise for increasing productivity and reducing fabrication costs. Past fabrication methods for ship structures have relied upon fastening methods such as periodically spaced bolts or rivets, adhesive bonding or conventional welding. Laser welding provides an extremely robust method to connect steel components and it can be performed at speeds 5-10 times that of conventional welding, thus requiring less manufacturing time. Furthermore, dimensional accuracies far superior to that obtained by conventional welding have been realized through laser welding. Laser welding can also be used in metal/composite hybrid connections wherein modular composite panels with embedded steel inserts are welded to a steel ship hull.

Since ships are complex structures which are subjected to dynamic loads, a thorough study of the static and dynamic load resistance is essential to the proper design of laser welded connections. Accordingly, the major objective of our research is to analyze the static and fatigue response of laser welded connections. We focus on continuous laser welded lap joints under different loading conditions. The analyses are based on the principles of linear elastic fracture mechanics due to the singular stress fields at the edges of the laser welds. The computational model presented here will enable engineers to design robust laser welded lap joints for prescribed loads.

A static stress analysis is performed to obtain the stress intensity factors and the failure load of laser welded lap joints. The geometry and nonlinear contact conditions of lap joints make it difficult to obtain an analytical closed-form solution. Therefore, the commercial finite element software ABAQUS is used to perform a stress analysis of various joint configurations and obtain the stress intensity factors and joint strength. It is found that the overlap length, weld width and plate thicknesses play a major role in determining the joints behavior under different loading conditions. The results are utilized to construct a metamodel that can be used to estimate the fracture strength of lap joints of arbitrary dimensions without having to perform a detailed finite element analysis every time. The parameters in the metamodel are optimized using a real-coded single objective genetic algorithm. The metamodels, which are validated and found to be quite accurate, are very useful for designing lap joints for prescribed static loads.

The fatigue response of laser welded lap joints is also investigated for different weld geometries and loading conditions. Fatigue failure is often a complex process due to numerous factors that influence crack growth. Nevertheless, it is important to develop a fatigue model for purposes of scheduling inspection at regular intervals, determining required maintenance, conducting a failure analysis, and minimizing the problem of crack propagation in future designs. A fracture specific finite element program FRANC2D is used to analyze crack growth, obtain the crack propagation trajectories and compute the corresponding stress intensity factor histories for the lap joint geometries under consideration. The Paris fatigue growth law is used to obtain the S-N curves for constant amplitude cyclic loads. It is found that the weld width has a significant effect on the crack trajectory and fatigue life.

ACKNOWLEDGEMENTS

The authors gratefully acknowledge funding for this project through the Office of Naval Research under grant number N00014-05-1-0735. Dr. Roshdy G.S. Barsoum of ONR is the cognizant program officer.

TABLE OF CONTENTS

LIST OF TABLES

LIST OF FIGURES

1. INTRODUCTION

This report for the Structural Response of Hybrid Ship Connections Subjected to Fatigue Loads (HSCF) project covers research on the design and fatigue analysis of laser-stake welded connections performed at the University of Maine from January 2006 to December 2007. In this effort, the University of Maine (UMaine) is partnered with Lehigh University of Bethlehem, PA and Applied Thermal Sciences Inc. (ATS) of Sanford, ME an engineering research and development consulting company with extensive experience in implementation of laser welding for ships.

The U.S. Navy currently has an objective to investigate the use of lightweight materials to enhance the future naval capabilities. Composite/metal hybrid systems offer a solution that meets this criterion. The HSCF program at the University of Maine is focused on the study of the fatigue response of combined composite and metal systems and innovative connection methods such as laser welding. The ultimate goal is to achieve an efficient, cost-effective durable ship hull. An efficient hull-form structure must be lightweight and stiff if it is to maintain its shape while resisting the applied loads. It also must be fatigue, impact and shock resistant. One of the primary cost drivers in developing advanced hull-forms with conventional techniques is in the metal forming of complex shapes. Composite materials have an inherent ability to perform complex shaping at relatively little incremental cost compared to flat panels. Material cost is a strong consideration in Navy ships, which are massive complex structures with large amounts of material used in their hulls. For this reason, when choosing composites for ships, the relatively inexpensive fiberglass reinforced polymer (GRP) composite systems

using a vacuum assisted resin transfer molding (VARTM) process are feasible and much research effort has focused on this material system.

The long-term goal of the research performed at UMaine is to develop and implement robust techniques for evaluation of the fatigue and environmental response of hybrid construction for use in U.S. Navy ships. Current design goals for the new class of navy ships are for vessels that are much faster and stealthier than currently available in the fleet. These newer vessels will dictate the use of advanced materials in their design that, among other characteristics, are lightweight and nonmagnetic. Although the original direction for use of new materials focused on composites, it was quickly determined that glass reinforced polymer (GRP) composites alone lack the stiffness and connectability required in the medium to long length modern ships. In these circumstances the use of a hybrid composite/metal structure can combine the benefits of traditional steel construction while using the low-density nature of composites in weight critical areas. Recently, the application of hybrid metal-to-composite structures is found in a widening number of engineering disciplines due to the inherent benefits of such systems.

A ship is a dynamically loaded vessel and mitigation of structural failures is essential. More often than not structural failures occur due to fatigue at connections and interfaces. Therefore, study of connection fatigue is essential in a robust structural design. An accurate appraisal of structural integrity depends primarily on proper assessment of the structural response of the connections and interfaces and a sound estimate of the dynamic nature of the loads that induce failure. Accordingly, one must perform a thorough investigation into the mechanics of the connections and interfaces of the vessel.

Understanding connection response and development of connections with highly efficient structural response is an essential part of this research.

Shipbuilders are showing increasing interest in laser welding as a means of reducing fabrication costs and distortion in ship construction and repair. Current interest lies in laser welded fabricated shapes and Laser welded Sandwich panels. It is ultimately envisioned that laser welding will be as common in the shipyard as other processes such as MIG, TIG and SMAW. Laser stake-welding of the outer shell of a ship structure to its frame is depicted in Fig. 1(a). Laser welding can also be used in metal/composite hybrid connections. In this method, modular composite panels with embedded steel inserts are welded to a steel ship hull as shown in Fig. 1(b). However, the high heat input from conventional welding techniques can be detrimental to the polymer matrix composite material. In comparison, the laser welding process allows welding to occur much closer to the composite material due to localized heating.

Cao and Grenestedt (2003) and Clifford et al. (2002) performed a study on a particular hybrid joint ideal for laser welding. In order to improve the strength and mechanical interlock properties of embedded hybrid joints, Melograna and Grenestedt (2002) investigated the effect of perforations in the steel on the strength of such joints. Joints were manufactured in which steel inserts with a hole pattern patented by Unden and Ridder (1985) were laminated into the GRP. It was found that the use of perforations significantly aided the strength of the joints. There were multiple reasons for this, including reduction in stiffness mismatch in the elastic properties of the steel and composite attributed to the progressively widening hole pattern in the steel. Additionally, the holes provided significant mechanical interlock whereas embedded joints without

holes rely strictly on the adhesion between the insert and the composite for strength. Understanding the dynamic response of laser welded connections in hybrid composite/metal connections is critical if they are to be used successfully in ship building.

The major objective of the present research is to evaluate the static and fatigue response of laser welded connections. We focus on continuous laser welded lap joints under different loading conditions. A static stress analysis is performed first to obtain the stress intensity factors and the failure load of laser welded lap joints. Subsequently, the fatigue response of laser welded connections is studied using a fracture specific finite element model. The computational model presented here will enable engineers to design robust laser welded lap joints for ship structures.

(a)

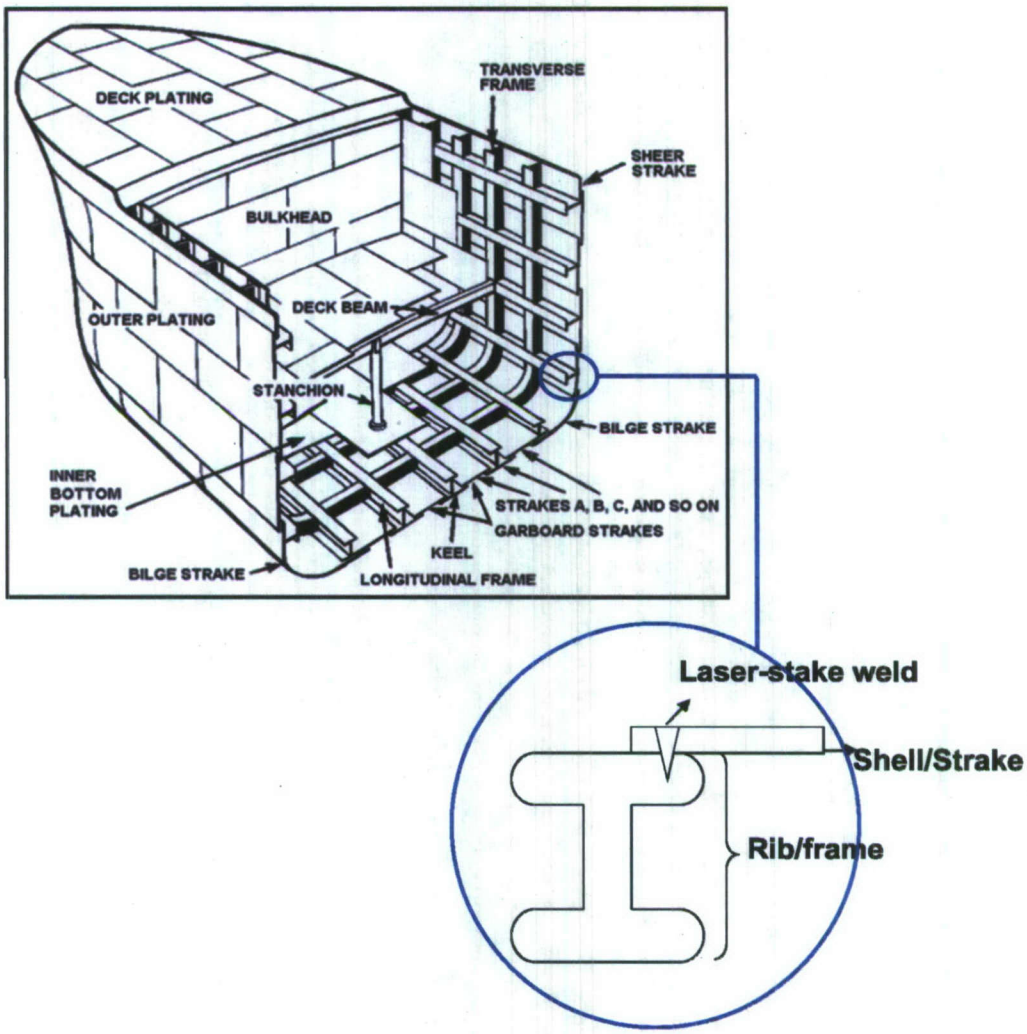

(b)

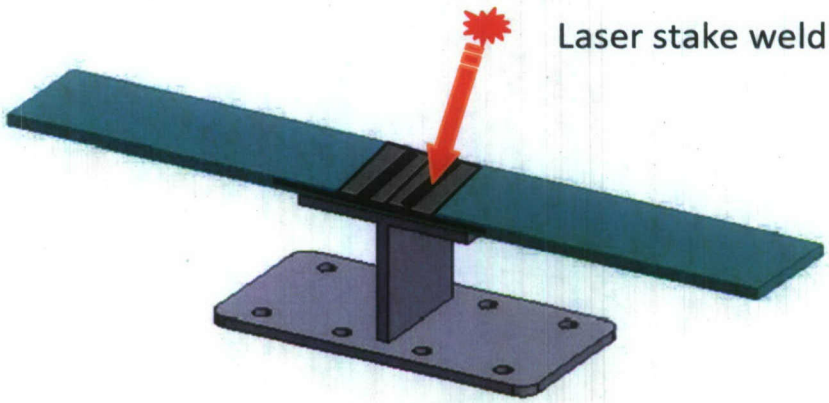

Figure 1.1: Laser stake welds in (a) ship construction (b) metal/composite hybrid connection.

1.1 Background and Research Motivation

In recent years, high power density welding technologies like laser welding have been increasingly utilized in industrial manufacturing. This is due to localized energy input, increased welding speed, high penetration, easy automation, excellent accuracy and small heat affected zones. These qualities lead to smaller dimensional and shape distortion of the welded pieces. With this in mind, the task of analyzing laser stake welded connections to determine their load carrying capacity and fatigue response is undertaken. In addition, the information obtained by performing various failure analyses is cleverly utilized to design optimal laser welded joint configurations.

1.1.1 Laser Welding

The term LASER is an acronym for "Light Amplification by Stimulated Emission of Radiation" and is defined as a device that emits highly amplified and coherent radiation of one or more discrete frequencies. In the laser welding process, the photons are targeted on the work piece surface which needs to be welded. Highly concentrated photon energy gets converted into thermal energy, which causes the materials to melt and fuse together as the laser energy is removed. Laser beam welding (LBW) is a type of fusion welding that is used to produce selective area spot welds or linear continuous seam welds. LBW is capable of welding carbon steels, HSLA steels, stainless steel, aluminum, and titanium. Due to high cooling rates, cracking is a concern when welding high-carbon steels. The weld quality is high, and is similar to that of electron beam welding. High power gas lasers are especially suitable for high volume applications, and as a result, LBW is rather prevalent in the automotive industry.

There are two types of laser welding processes, conduction and penetration. Laser conduction welding relies on the conductivity of a material. It is used for spot, continuous and partial penetration seam welding. Laser penetration welding, on the other hand, is carried out by focusing the laser beam energy at a single location until the abutted materials are heated to a liquid state. The laser energy is removed and the liquid material begins to cool, thus joining the previously separate pieces as the liquid metal solidifies. Another important process is hybrid laser arc welding (HLAW) which combines laser with conventional gas metal arc welding processes. This increases the speed of performing the weld and provides higher strength bonds with less potential for undercutting.

The two types of lasers commonly used in metal working are solid-state lasers and gas lasers (especially CO_2 lasers). The first uses any solid media, including synthetic ruby and chromium in aluminum oxide, neodymium in glass, and the most common type being crystal YAG (composed of yttrium, aluminum, and garnet) doped with neodymium. Gas lasers use mixtures of gases like helium, nitrogen, and carbon dioxide as a medium. Solid-state lasers operate at wavelengths of 1.06 μm, much shorter than gas lasers. Both lasers can operate in both pulsed and continuous modes. Typical power output for ruby lasers is 10–20 W while the YAG laser outputs between 0.04 and 600 W. To deliver the laser beam to the weld area, fiber optics is usually employed. Gas lasers pertaining to this project, use high-voltage, low-current power sources to supply the energy needed to excite the gas mixture used as a lasing medium. These lasers have wavelengths of 10.6 μm. As there are no waveguides used for gas systems, a lens and mirror delivery system is used. Power outputs for gas lasers can be much higher than

solid-state lasers, reaching 25 kW. It is hopeful that modular fiber lasers can achieve the same power output.

1.1.2 Stresses due to Welding

The technique of laser welding, which can join steel plates at speeds of several meters per minute in a single weld pass, is very promising. This type of technology could prove very useful for huge structures like naval ships, oil tankers, etc. However, the fast cooling rates in the welded zone produce a very hard and brittle microstructure which may produce structural integrity problems. This area is called the heat-affected zone (HAZ). The size and strength of the HAZ depends on the material's thermal properties and the power and speed of weld process being used. The thermal diffusivity of the base material plays a large role. If the diffusivity is high, the material cooling rate is high and the HAZ is relatively small. Conversely, a low thermal diffusivity leads to slower cooling and a larger HAZ. Laser beam welding gives a highly concentrated and limited amount of heat, resulting in a small HAZ, which is desirable. While welding, the heat flows from high temperature metal to the surrounding metal which generates thermal gradients causing thermal stresses. When this material cools and solidifies it retains residual stresses. There are processes available to alleviate these residual stresses, for example, annealing. In this work, any connection being analyzed is assumed to have been already stress relieved.

1.1.3 Fracture Mechanics

Fracture mechanics is comprised of a series of models used to describe the influence of cracks or defects on material failure. The aim for a portion of this work is to use fracture mechanics to analyze a laser welded lap joint model under static and fatigue

loads. To demonstrate the need for doing this, the joint is modeled using a commercial finite element package ABAQUS. When certain unit moments are applied at the free ends of the welded plates, it is observed that the joint opens up and stresses at the weld-ends start approaching infinity. Thus, it is reasonable to say that the non-welded overlapped lengths act as cracks or notches and the weld ends as left and right crack tips.

Griffith (1920) performed fundamental experiments on the strength of thin glass fibers. He concluded that thinner fibers failed at higher stresses than thicker fibers, an outcome not predicted by conventional stress-based strength theory. Griffith considered the thermodynamic equilibrium of a crack system and stated that a crack will grow when the total energy of the system starts reducing. In a classic paper, Inglis (1913), came up with an expression in which the magnitude of stress at the tip of a hole varies both with the size of the hole and sharpness of the tip, thus providing a first means in determining the larger stress gradients around the crack tips.

Irwin (1956) developed an energy release rate concept which is an extension of the Griffith's theory, albeit in a more useful form. Before that, Westergaard (1939) developed a semi-inverse technique for analyzing stresses and displacements ahead of a sharp crack. Irwin used Westergaard's approach to show that the stresses and displacements near the crack tip could be described by a single parameter that was related to the energy released rate, which is called as the stress intensity factor (SIF). Over time, there have arisen two fundamental approaches to fracture problems; the strain energy release rate method, which is based on global energy balance of the whole system, and the stress intensity factor method, which is based on the local stress distribution around a crack tip. For the sake of ease, simplicity, clear demarcation of the various fracture

modes and their individual effects on the failure strength of the joint, and ultimately to be able to develop a simple method of predicting fatigue behavior of the joints, the stress intensity factor approach will be used throughout this work.

1.1.3.1 Stress Intensity Factor

The traditional problem with the strain energy release rate method is that it depends on the total energy state of the whole structure before and after the crack growth. For complex problems which typically involve large models and numerical solution techniques, this approach is not very feasible. As a result, the stress intensity factor method can be used as a simple to implement alternative.

Consider the tip of a crack in a uniform tension field σ, as shown in Fig. 1.2. In a polar coordinate system, the general two dimensional solution for the stresses near the tip of the crack at an angle θ and radial distance r are:

$$\begin{aligned}
\sigma_x &= \frac{K_I}{\sqrt{2\pi r}} \cos\frac{\theta}{2}\left(1 - \sin\frac{\theta}{2}\sin\frac{3\theta}{2}\right), \\
\sigma_y &= \frac{K_I}{\sqrt{2\pi r}} \cos\frac{\theta}{2}\left(1 + \sin\frac{\theta}{2}\sin\frac{3\theta}{2}\right), \\
\tau_{xy} &= \frac{K_I}{\sqrt{2\pi r}} \sin\frac{\theta}{2}\cos\frac{\theta}{2}\cos\frac{3\theta}{2}.
\end{aligned} \tag{1}$$

Note that each stress component is proportional to K_I which is known as mode-I stress intensity factor. K_I can be defined as the intensity of the stress singularity that occurs at

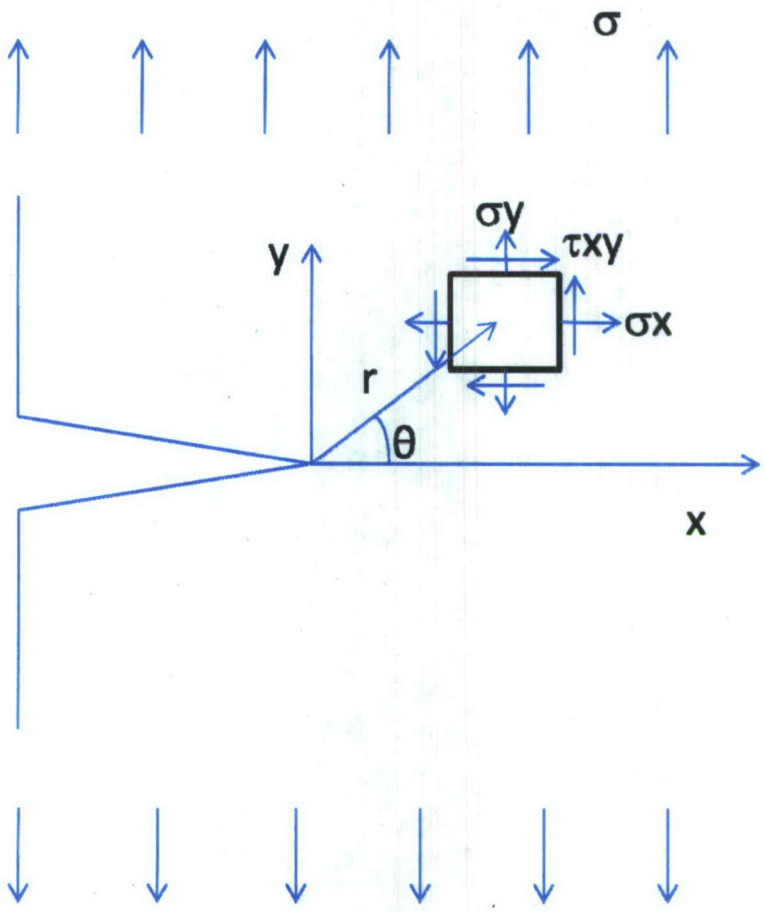

Figure 1.2: Crack tip in a uniform tension field.

the tip of a sharp crack due to a pure transverse loading. If K_I is known, then the entire stress distribution at the crack tip can be computed by equation (1). K_I can thus be said is a function of the applied load, the crack length and the specimen's geometry. Using the concept of dimensional analysis, K_I can be evaluated as:

$$K_I = \beta \sigma \sqrt{cl}, \tag{2}$$

where β is a dimensionless geometry parameter, σ is the far field stress magnitude and cl is the crack length. The unit of stress intensity factor is Psi$\sqrt{}$in. Because K_I is defined as a measure of stress intensity at the crack tip, it can be said that a crack will grow when K_I reaches a critical value $K_I = K_{Ic}$, where K_{Ic} is the critical stress intensity factor for a material. K_{Ic} is thus considered a material property (analogous to yield strength) that defines the material's resistance to crack growth. It is often referred to as fracture toughness of the material.

Three modes of fractures can be defined; the previously mentioned mode-I which is due to in-plane tension, mode-II due to in-plane shear and mode-III where there is out of plane shear load. These modes are illustrated in Fig. 1.3. Mode-I is typically seen as the dominant mode in many structural materials and receive more attention in literature. Each mode has its own independent critical stress intensity factor, these being K_{Ic}, K_{IIc} and K_{IIIc} respectively.

1.1.3.2 Other Fracture Criteria

The basic assumption of Linear Elastic Fracture Mechanics (LEFM) is that all available strain energy goes into propagating a crack or, according to Griffith, in creating

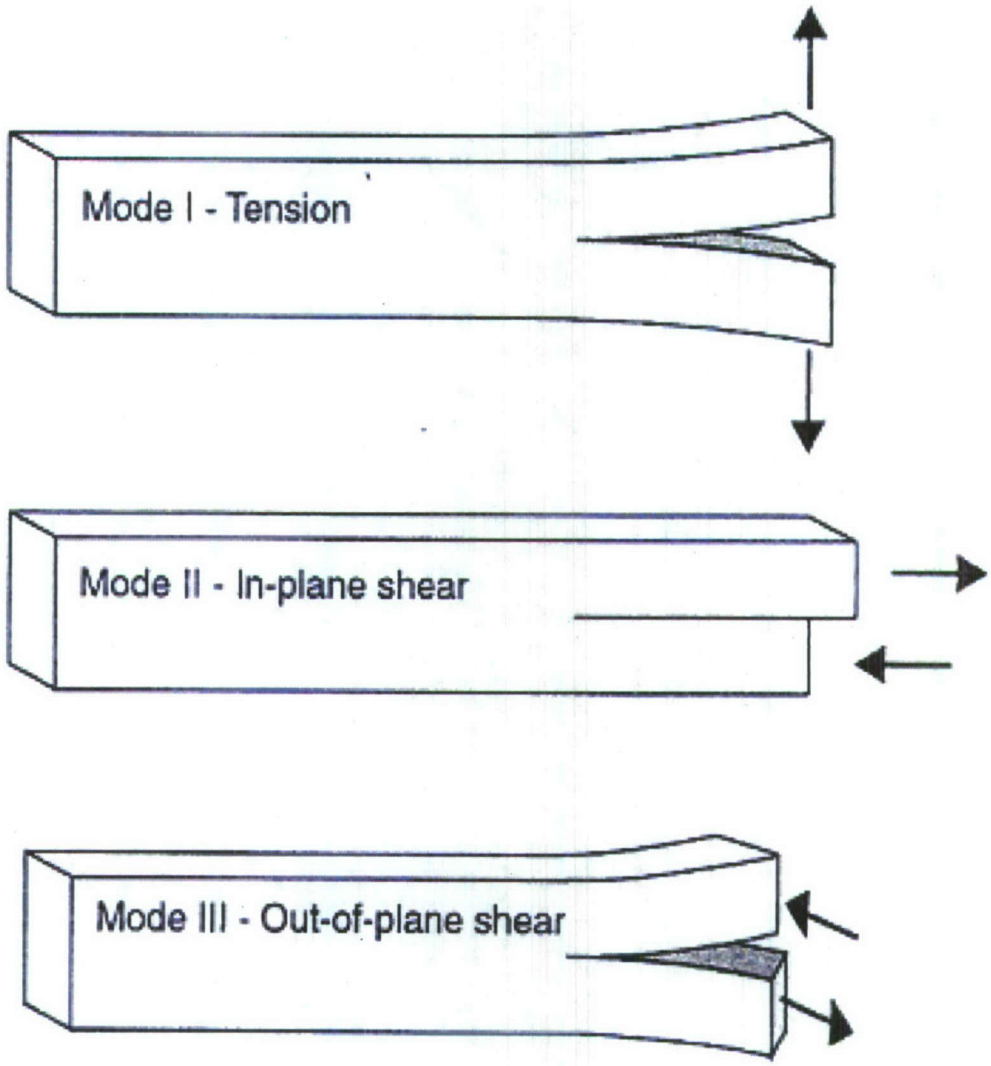

Figure 1.3: Illustration of the three fracture modes.

new surfaces. In reality, however, many materials have some micro structural mechanisms that dissipate the available energy, for instance:

- Plastic deformation around the crack tip in metals.
- Micro-cracking and friction in concrete and rock.
- Fiber bridging in wood and fibrous composites.
- Inclusions.

These phenomena can be referred to as toughening mechanisms. The only toughening mechanism seen in isotropic metals is plastic deformation. Although in metals, LEFM concepts can be slightly altered in order to tolerate limited plasticity in the crack tip region, the validity of LEFM ceases when significant plastic deformation occurs. At high loads in a lap joint configuration made of steel, it is safe to assume that the energy loss is due to plastic deformation. Beyond the elastic limit, another concept, Elastic-Plastic Fracture Mechanics (EPFM) comes into the picture. Although it is an extension to the elastic deformation, EPFM cannot be applied for yield leading to plastic collapse. Wells (1961) attempted to apply LEFM to low and medium carbon steels and noticed the displacement of crack surfaces near the crack tip due to plastic deformation preceding failure. As a result, he proposed an alternative fracture criterion known as Crack Tip Opening Displacement (CTOD).

Rice (1968) in a seminal paper idealized plastic deformation as a nonlinear elastic process and developed another parameter to characterize nonlinear material behavior ahead of a crack. He expressed energy release rate for non-linear materials as a line integral which he termed as the J-Integral. The J-Integral can be evaluated along any arbitrary contour around the crack tip as it is path independent.

Linear elastic fracture mechanics has proven to be very useful for the fatigue process in the near-tip region of a crack under cyclic loading. The idea of using LEFM is that the stress intensity factor can still be used to analyze progressive crack propagation in the fatigue process zone. In the case of a constant amplitude cyclic load, experimental studies have shown that the crack growth rate is a function of the amplitude of the stress intensity factor. One such fatigue crack growth law was proposed by Paris and Erdogan (1960). The theoretical predictions of the Paris Law compare favorably with experimental results for moderate loads considered in this research. Realistically, micro structural mechanisms (like plasticity) also affect the prediction of the fatigue life of a joint. This requires the consideration of an elasto-plastic failure criterion into the fatigue equation. Since such an analysis is complicated, the present research utilizes a simpler and reasonably correct approach based on LEFM to outline the procedure of predicting fatigue life of elastic and moderately plastic materials.

1.1.4 Single-objective Genetic Algorithms

The mathematical model for the computation of the fracture strength of arbitrary joint dimensions is optimized using real-coded single objective GA. Several techniques have been created for optimizing a given objective function. These include the linear least squares method, the steepest descent method, the Levenberg-Marquardt method, and the Gauss-Newton method among many others. These methods, unlike the genetic algorithm (GA), tend to hone in on local minima or maxima and are only efficient when the objective function possesses continuous derivatives and is not too complex. Genetic algorithms are used when the search space is either too large or too complex for an analytical method. Genetic algorithm, an optimization methodology,

introduced and investigated by Holland (1975), is inspired by evolutionary processes and the "survival of the fittest" concept. In broader terms, a GA is a stochastic global search method that mimics the concept of natural biological evolution.

To begin the GA procedure, a solution space is first provided and a population of random potential solutions is generated. The fitness of each individual is evaluated and a fitness rating is assigned to individuals reflecting the designer's goals. Applying the principle of "survival of the fittest", this fitness rating is used to select and keep multiple copies of better performing individuals and eliminate poor design solutions. Individuals are chosen from among the better solutions retained, to "mate" and create child solutions using recombination operators borrowed from natural genetics, namely crossover and mutation, which in general leads to a child population of mostly improved designs. The new child population is often compared with the previous parent population and only the best of the parent and child populations is retained. This process is called elitism and is often used for increasing the performance of the genetic algorithm. The process of selecting the best individuals for mating, creating child offspring populations and so on is repeated over many generations until one is satisfied with the final result or some established convergence criteria is met. Fig. 1.4 illustrates the GA process in a simple flowchart.

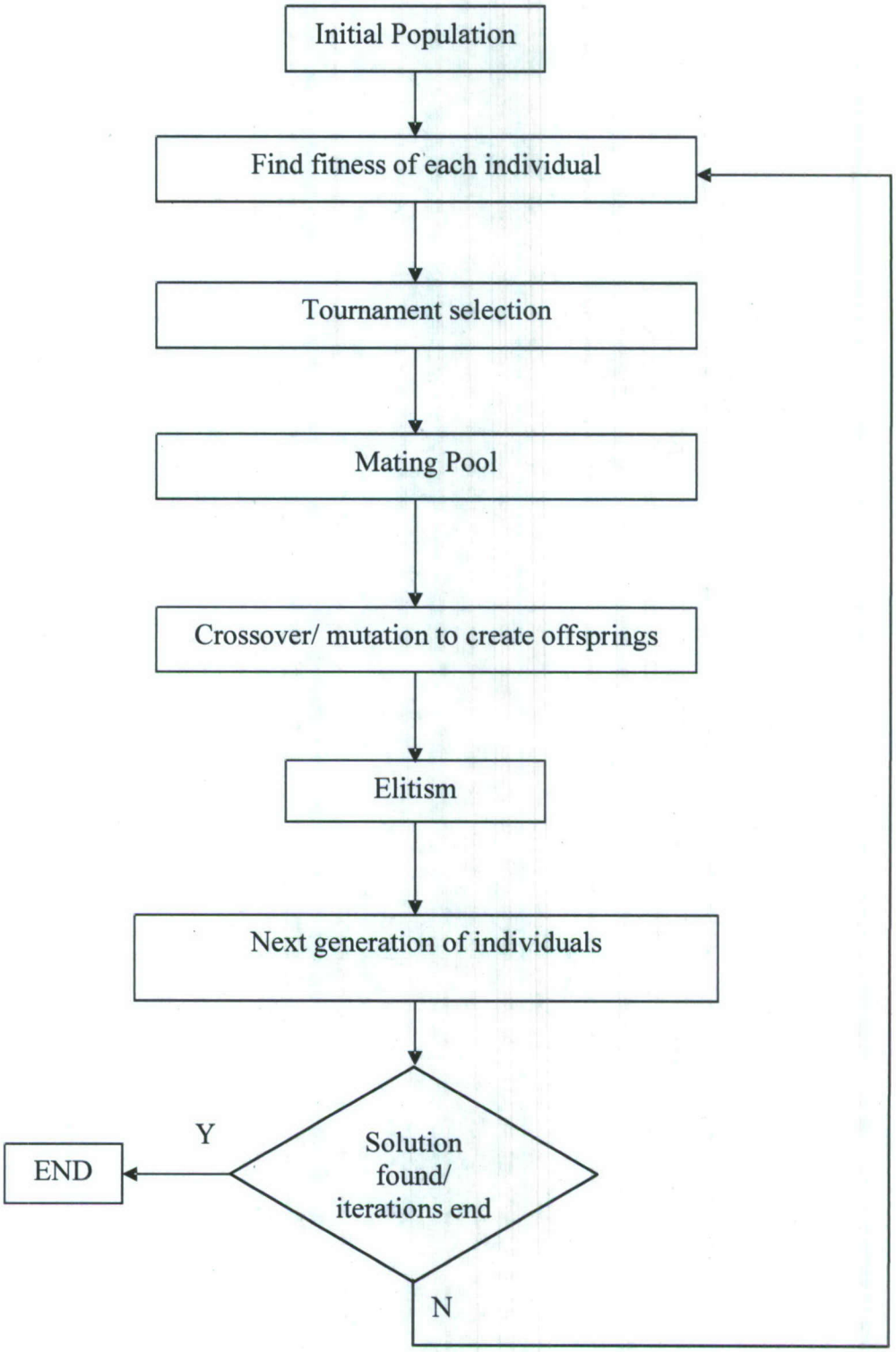

Figure 1.4: Genetic algorithm procedure.

1.2 Literature Review

There is an increasing interest by ship builders to incorporate laser welding technology in their operations to reduce fabrication costs. Before one can start using laser welding processes in the construction of ship structures, one must first know the durability or fracture toughness and fatigue resistance of a laser welded structure. Sumpter (1996), studied the cause of fractures in ship structures on the microscopic level. The quality of laser welding is discussed in the work which garners its insights with the help of experiments that place cracks at different locations in the structure. These locations include cracks at the weld centerline, at heat affected zone or in the plate material. The obtained results are then compared with those obtained by similar experiments where arc welding was used. During the tests the major objective was to avoid cleavage fracture, the occurrence of which is strongly influenced by temperature. The toughness of a laser welded mild steel ship plate was measured by dynamic fracture mechanics testing at a temperature of 0°C. The elastic-plastic fracture criterion is found to be the smallest when the crack was located at the HAZ, and is similar in numerical value as compared to material joined by typical arc welding. All in all, the work provided helpful insights on the process of determining K_{Ic} of laser welded materials.

Caccese et al. (2006) compared the effect of weld geometries on laser welded HSLA-65 steel cruciforms. New welding techniques were employed, specifically a combined laser and gas-metal-arc welding (GMAW) procedure. A number of fatigue tests were run on laser-welded cruciforms of different weld geometries available with laser welding, as well as some conventionally welded specimens. It was found that if weld geometry is carefully controlled, the hybrid laser welded specimens performed

better than the conventionally welded specimens and what the currently accepted fatigue life equations would predict.

In a typical lap joint geometry, it can be said that there exists two interface cracks between the two plates. An approach at tackling the problem is given by Suo and Hutchinson (1990). They considered a semi-infinite interface crack between two infinite isotropic elastic layers under general edge loading and presented a mathematical model for its analysis. Their study is concentrated mainly on interface cracks between thin films and substrates. They have introduced expressions for the stress intensity factors for the geometry similar to the geometry and loading conditions under consideration. Furthermore, their computation of stress intensity factors involved the principle of superposition and thus, the technique is not suitable for geometrically non-linear structures such as the ones we consider here where interface contact is present. Further discussion of this topic is given in Section 2.6.4.

When the crack length is comparable to the characteristic dimensions of the structure, it becomes difficult to compute an analytical expression for the stress intensity factor (Sun, 2001). In such cases numerical techniques become very useful. One such technique, created by Irwin (1956), is the Crack Closure Integral which utilizes nodal force and displacement information at the crack tip to compute the stress intensity factors. This force and displacement data can now easily be obtained from any finite element package. Several researchers have found the technique useful, but a little onerous. The method requires two separate analyses to obtain the desired results, one with the original geometry to get the nodal forces and a second with an extended crack to get the displacements. Improving upon this concept, Rybicki and Kanninen (1977) came up with

a more efficient technique for evaluating stress intensity factors using finite element calculations called the Modified Crack Closure Technique. The method falls under the category of indirect methods and permits evaluation of both mode-I and II stress intensity factors from the results of a single analysis. In their work they define the limitations of the method and a correction factor for the case where unequal element lengths are present before and after the crack tip. This method proved to be very helpful in this work with regard to computing stress intensity factor values for different joint dimensions.

Unlike Rybicki and Kanninen, Krueger (2002) referred to the aforementioned technique as the Virtual Crack Closure Technique (VCCT) and presented it with reference to the delamination of composite structures and used the method to compute damage tolerance. In addition, Krueger also presented several ways in which the VCCT can be applied. For example, Krueger has supplied equations for two-dimensional quadrilateral elements with linear and quadratic shape functions, formulae for using the VCCT method with three-dimensional solid elements and also expressions for using the method with plate/shell elements. While the correction factor for unequal element length was already established, he has presented an analogous correction for unequal element widths.

A work that uses a very similar approach to the one adopted here, is performed by Gowhari and Anaraki (2005). They analyzed the fatigue response of spot-welded lap joints for shear-tension loading. A combination of EPFM and LEFM techniques were used and results were presented in the form of structure, notch and crack configuration factors. Their main aim was to present fracture data in terms of non-dimensional geometric parameters in order to provide a direct method for weld life prediction. In their

work they also assumed the non-welded overlapped plate length as a notch, and since the welds under consideration resembled a nugget, the notch was considered a three dimensional crack. A finite element parametric study was performed which used normalized forms of some of the influential geometric dimensional parameters. Predictive equations for the SIF and the J-integral are given by employing a statistical multiple non-linear regression model on the results obtained from the parametric study. Unlike our work, they used three-dimensional finite element models and used over 1000 analyses to obtain accurate prediction equations.

Terasaki and Kitamura (2004) presented a procedure for prediction of static fracture strength of laser welded lap joints by numerical analysis is presented. In their work, the finite element model is compared with the experimental results at several steps, even to decide the appropriate boundary conditions for the model. They have established a numerical method which conforms to the experimental load-displacement curves of tensile-shear tests, and then used that method to investigate whether the experimentally determined static fracture strength of lap joints can be predicted by the equivalent plastic strain. The analyses were performed on ABAQUS with CPS8R (8-node two dimensional reduced integration) elements using large deformation theory where plane-stress conditions prevail.

The analytical expressions for standard cracked geometries, like the edge crack and center crack models with tensile and shear loading, are helpful for assessing the accuracy of finite element models by performing convergence studies that compare the analytic and numerical results. The analytical expressions for stress intensity factors for several standard configurations are provided in books by Broek (1978) and Irwin (1985).

A very clear explanation of the mixed mode plastic zone size is given in a book by Gdoutos (2005), both for plane-stress and plane-strain conditions. Crack growth, elastic-plastic fracture mechanics and fatigue have also been discussed in detail, some topics of which are pursued in this work in Chapter 3.

Assessing the strength of a connection design requires not only analyzing the joints resistance to static loads but also for determining its response to fatigue conditions as well. Recent experiments in the fatigue performance of laser welded lap joints show that the performance of the connection is dependent upon the weld pattern. Multiple longitudinal welds possess higher fatigue strength than simple transverse welds. Hsu and Albright (1991) established a technique for predicting the fatigue response of laser welded lap joints. A static stress analysis was combined with a cyclic stress-strain analysis to establish a model for calculating joint stresses under cyclic loading.

Laser welded lap joints suffer from defects like notch effects, surface cracks, residual stresses, etc. Cho et al. (2004) performed finite element analyses and fatigue tests to estimate the fatigue strength of laser welded lap joints. They determined that residual stresses and welding direction were two major factors that affected the fatigue strength of the joint. When a fatigue load is applied to a laser welded joint containing residual stresses the applied and residual stresses combine, thus reducing the fatigue strength of the joint significantly. To arrive at these conclusions, three dimensional models with longitudinal and transverse weld directions and eight node quadrilateral elements are constructed and analyzed. Using temperature distribution data from a heat flow analysis, a thermo-elastic-plastic stress analysis is performed which simulates the complete cooling process all the way down to the ambient temperature. Next, the equivalent fatigue

strength is calculated using the elastic-plastic stress analysis with the residual stress effect in place. The work was performed using the finite element program ABAQUS utilizing a few key user-defined subroutines.

Computation of stress intensity factors with numerical methods is typically carried out using the finite element methodology. The reader is referred to Logan (2001) for an explanation of the basic and applied concepts of finite element analyses which have been helpful in completing this work. ABAQUS documents (Analysis & Theory manuals Version 6.5) have been extensively referred to for information pertaining to mesh type, mesh control features, element types and the compatibility between the quadratic and triangular elements.

When the results obtained by a parametric study exhibit a strongly non-linear behavior, it becomes difficult to create useful predictions by using simple curve fits on the data. A more robust technique, namely metamodels, allows one to construct an approximate model using function values at a few sampling points typically derived from experimental design methods. A few of the most popular metamodeling techniques are the response surface methodology (RSM), the kriging method, multivariate adaptive regression splines, neural networks and radial basis functions (RBF). Fang et al. (2005) performed a comparative study of two metamodeling methods, RSM and RBF, by considering multi-objective optimization of a vehicle body subjected to a frontal collision. The RSM and RBF models were validated via finite element simulations of the full scale vehicle model. The main objective of the work is to assess the ability of the RSM and RBF methods as applied to the study and optimization of vehicle crashworthiness, a highly non-linear problem. In their findings, Fang et al. note that RSM

may not be suitable for modeling highly non-linear responses using only a limited number of response samples. Radial basis functions, on the other hand, were found to be very promising. Although the RBF models are computationally more expensive, the optimization results were found to be more accurate. Based on the findings of Fang et al., we utilize the augmented radial basis function method to construct the metamodel (Krishnamurth, 2003) for this work. Further details concerning this process will be discussed in Section 2.7.

1.3 Outline and Research Approach

The second chapter of the report presents a method for the evaluation of stress intensity factors at the notch tips in laser welded lap joints. Throughout the work, we limit our focus to steel materials. Residual stresses and material alterations due to the laser welding process have been neglected in the present analysis for the sake of simplicity. We assume that all contacts are hard and frictionless and confine ourselves to working within the realm of linear elastic fracture mechanics. Crack propagation and fatigue analyses of lap joints under bending and tensile loads are presented in the third chapter of the report.

1.4 Contributions of Research

The specific contributions of the present research are:

1. A numerical model is presented to compute the static failure strength of laser-welded lap joints. The stress intensity factors at the sharp notches between the welded plates are determined using linear elastic fracture mechanics principles.
2. Parametric studies of the fracture strength of several different laser-welded lap configurations are conducted and the results are used to develop a metamodel for

the rapid analysis of lap joints based on its geometric dimensions. A methodology is presented for designing lap joints under prescribed loads using the metamodel.

3. Crack propagation and fatigue analysis of lap joint configurations is performed using a finite element program called FRANC2D. Parametric studies of the crack trajectories have been conducted for different weld-widths and loading conditions.
4. The fatigue life of laser-welded lap joints has been analyzed using the Paris Law. It is demonstrated that the weld-width plays a significant role on the fatigue strength of the lap joint.

2. ANALYSES OF LAP JOINT CONFIGURATIONS

2.1 Introduction

In this section a metamodel is presented for the evaluation of the fracture strength of a laser welded lap joint of arbitrary dimensions without having to perform a dedicated finite element analysis for the geometry in question every time. This is achieved by performing detailed finite element analyses of a limited number of joints of varying dimensions and utilizing the results to develop a higher dimensional curve fit using radial basis functions.

It is difficult to obtain a closed-form analytical expression for the fracture strength of the laser welded lap joints considered here. A finite element model is used to compute the stress intensity factors at the notches and determine the fracture strength of the joint. First, convergence studies are performed on representative model to establish requirements for obtaining accurate results from the finite element analyses. The dependence of stress intensity factor on joint dimensions and load-type is then investigated by performing parametric studies using finite element models. To compensate for the lack of an analytical expression, a metamodel is formed to interpolate the results obtained from the parametric studies. The metamodel is optimized using a single-objective genetic algorithm and validated by finite element results evaluated at sample joint dimensions which were not used in construction of the metamodel.

2.2 Problem Formulation

Fig. 2.1 depicts the type of connection geometry under consideration which is referred to as a simple lap joint. The dimensional parameters here are welded length (w), non-welded length (a) and the thicknesses of the top (h) and bottom plates (H). The width

of the joint in the x_3-direction is assumed to be much larger than the plate thickness and the loads are assumed to be independent of the x_3-coordinate. The finite element analyses will be based on linear elasticity. Frictionless hard contact is assumed over the non-welded segments of the plates. It is anticipated that the fracture strength will have a nonlinear dependence on the applied load due to the contact conditions. The material of the connection plates is chosen to be steel as previously mentioned.

2.3 Stress Analysis of Laser Welded Lap Joints

A detailed analysis of a representative laser welded lap joint is performed using the finite element program ABAQUS, to quantify the stresses in the welded region. The element type used is CPE4R, a four-noded element which is discussed in further detail in Section 2.6.2. The dimensions of the representative joint are chosen as $h = H = w = a =$ 1". Other joint configurations will be considered later in this chapter. The plates are chosen to be sufficiently long in the x_1-direction in order to minimize the influence of the edge effects on the stresses in the welded region. The entire structure is subjected to an applied counter-clockwise moment of $M^+ = 1$ lb-in/in, direction of which is shown in Fig. 2.2(a). Hard contact conditions are enforced in the non-welded regions between the two welded plates. This is accomplished by specifying contact surfaces on

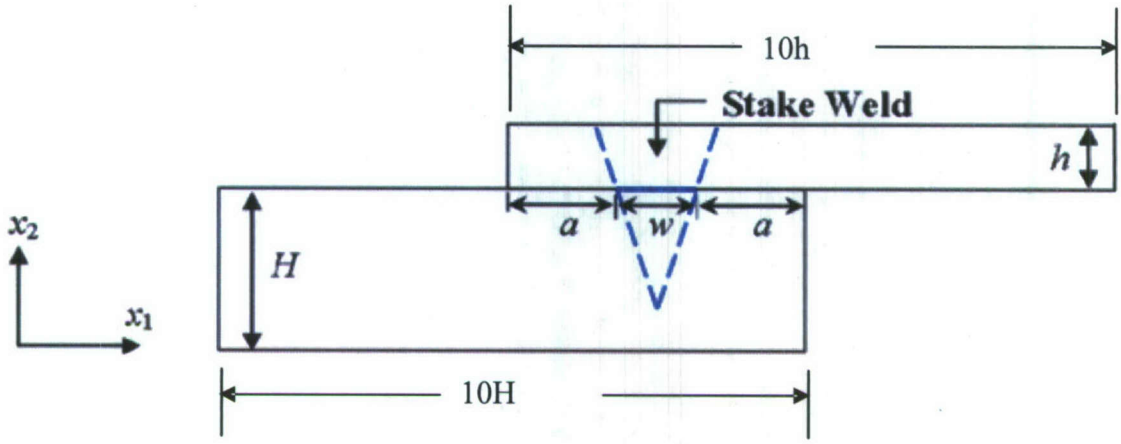

Figure 2.1- Laser welded lap joint configuration.

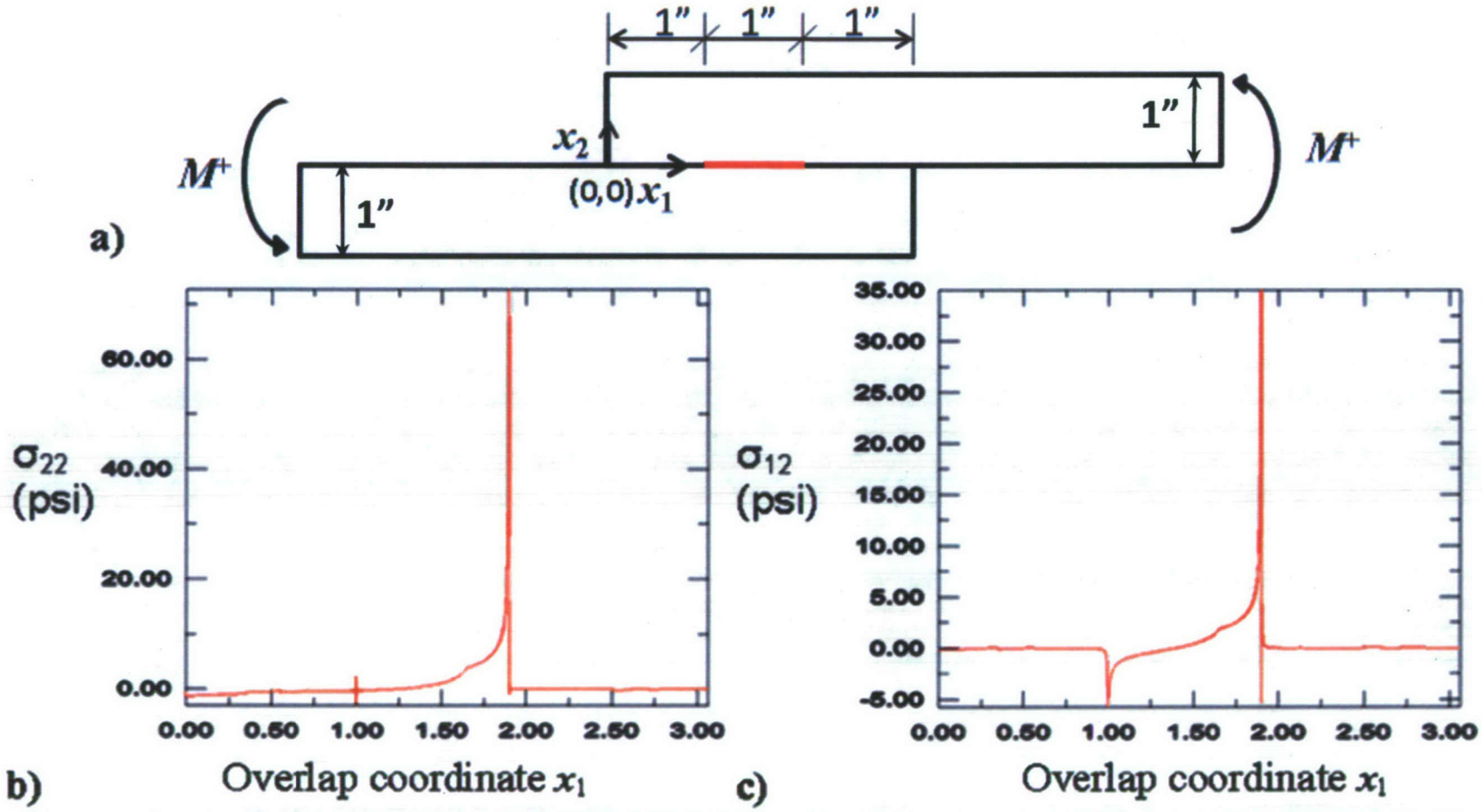

Figure 2.2: Stress analysis of a laser welded lap joint under an applied moment: a) loading configuration, b) transverse normal stress and c) transverse shear stress.

the two sides of the interface, and thus, penetration of one surface into another is prevented. A very fine mesh is used to ensure that the results have converged. Fig. 2.2(b) and (c) depict the transverse normal and shear stresses, respectively, at the interface between the plates as a function of the overlap coordinates x_1. It is observed that the stresses are singular at the edges of the weld due to the sharp notches created by the nature of the geometry. The sharp notches induce large local stresses even at low applied loads. These observations justify the use of fracture mechanics concepts for this joint analysis.

2.4 Fracture Criterion

The fracture behavior of a lap joint is determined by the stress intensity factors at the notches located at the left and right edges of the laser welded region. The high transverse normal stress σ_{22} and transverse shear stress σ_{12} at those locations may result in fracture which is governed by both mode-I and II stress intensity factors (K_I and K_{II}). A combination of fracture modes is referred to as a mixed mode. Under mode-I conditions, growth occurs in the direction of the crack. Under mixed mode conditions, experimental observations indicate that both K_I and K_{II} play a major role in crack growth and that the crack does not grow in its original direction. Both energy and near tip stress approaches are commonly used in the study of mixed mode fracture. In the energy approach, the crack is assumed to grow in the direction that maximizes the energy release rate. This approach becomes very tedious for crack branching under mixed mode fracture. Several failure theories have been proposed for modeling mixed mode fracture that provides results consistent with experimental observations. These include:

- Elliptical model.
- Maximum tensile stress criterion (MS-criterion).
- Strain energy density criterion (S-criterion).
- Maximum energy released rate criterion (ME-criterion).

We utilize the maximum tensile stress criteria proposed by Erdogan and Sih (1963) which assumes that (i) crack extension occurs in the direction at which the circumferential stress $\sigma_{\theta\theta}$ takes the maximum value with respect to θ and (ii) fracture takes place when the intensity of the maximum circumferential stress $\sigma_{\theta\theta}$ is equal to a value that leads to mode-I fracture. For mixed mode fracture the stresses near the crack tip are

$$\begin{aligned}
\sigma_x &= \frac{K_I}{\sqrt{2\pi r}}\cos\frac{\theta}{2}(1-\sin\frac{\theta}{2}\sin\frac{3\theta}{2}) - \frac{K_{II}}{\sqrt{2\pi r}}\sin\frac{\theta}{2}(2+\cos\frac{\theta}{2}\cos\frac{3\theta}{2}),\\
\sigma_y &= \frac{K_I}{\sqrt{2\pi r}}\cos\frac{\theta}{2}(1+\sin\frac{\theta}{2}\sin\frac{3\theta}{2}) + \frac{K_{II}}{\sqrt{2\pi r}}\sin\frac{\theta}{2}\cos\frac{\theta}{2}\cos\frac{3\theta}{2},\\
\tau_{xy} &= \frac{K_I}{\sqrt{2\pi r}}\sin\frac{\theta}{2}\cos\frac{\theta}{2}\cos\frac{3\theta}{2} + \frac{K_{II}}{\sqrt{2\pi r}}\cos\frac{\theta}{2}(1-\sin\frac{\theta}{2}\sin\frac{3\theta}{2}).
\end{aligned} \tag{3}$$

where r and θ are the polar coordinates with respect to the crack tip of the material point, as shown in Fig. 1.1. Using the direction cosine matrix, the stresses can be transformed from Cartesian to polar coordinates resulting in

$$\begin{aligned}
\sigma_{\theta\theta} &= \frac{1}{\sqrt{2\pi r}}\cos\frac{\theta}{2}\left[K_I\cos^2\frac{\theta}{2} - \frac{3}{2}K_{II}\sin\theta\right],\\
\sigma_{r\theta} &= \frac{1}{\sqrt{2\pi r}}\cos\frac{\theta}{2}\left[\frac{1}{2}K_I\sin\theta + \frac{1}{2}K_{II}(3\cos\theta - 1)\right].
\end{aligned} \tag{4}$$

From equation (4) we deduce that

$$\frac{\partial\sigma_{\theta\theta}}{\partial\theta} = -\frac{3}{2}\sigma_{r\theta} \tag{5}$$

This shows that at some value $\theta = \theta_o$, $\sigma_{\theta\theta}$ reaches its maximum when $\frac{\partial \sigma_\theta}{\partial \theta} = \sigma_{r\theta} = 0$. The crack initiation angle θ_o will be such that $\sigma_{r\theta} = 0$, and thus, from the second equation in (4) the following condition is obtained for θ_o:

$$K_I \sin\theta_o + K_{II}(3\cos\theta_o - 1) = 0. \tag{6}$$

According to the assumption of Erdogan and Sih (1963), fracture takes place when $(\sigma_{\theta\theta})_{max}$ becomes $K_{Ic}/\sqrt{2\pi r}$. This yields the fracture criterion

$$K_I \cos^2\frac{\theta_o}{2} - \frac{3}{2}K_{II}\sin\theta_o = \frac{K_{Ic}}{\cos(\theta_o/2)}, \tag{7}$$

Equation (7) represents the mixed mode fracture criterion where K_{Ic} is the critical mode-I stress intensity factor and θ_o is obtained from the auxiliary equation (6). It is noted that only one material property K_{Ic} is involved in the criterion. If the first of the two extremes of θ_o is computed, this being associated with mode-I or when $K_{II} = 0$, then $\theta_o = 0$ is obtained implying that the crack extends in its original direction. For the other extreme when pure mode-II conditions exist ($K_I = 0$), the computed crack extension direction is $\theta_o = -70.5°$. Thus it can be inferred that for a mixed mode condition, the crack initiation angle will be between -70.5° and 0°.

2.4.1 Critical Load Calculations

No fracture mechanics study is complete without discussing the critical load for fracture initiation. Under linear elastic fracture mechanics theory, it can be said that the stress intensity factors are directly proportional to the applied load. This assumes that no nonlinearity is present in the structure. The stress intensity factors K_I^{Mo} and K_{II}^{Mo} are obtained via analysis of the structure when a moment M_o is applied at the free end of the upper plate and the other end is restrained. According to linearity, the mode-I stress

intensity factor for a moment M_c is $M_c \cdot K_I^{Mo}/M_o$. By substituting this expression for stress intensity factor in equation (7), the critical moment can be computed as:

$$M_c = \frac{K_{Ic}}{\cos\frac{\theta_o}{2}\left[\frac{K_I^{M_o}}{M_o}.\cos^2\frac{\theta_o}{2} - \frac{3}{2}\frac{K_{II}^{M_o}}{M_o}.\sin\theta_o\right]}. \quad (8)$$

This critical moment represents the failure load of the structure. This expression is very useful for designing joints so that a desired factor of safety for a fracture type failure can be achieved.

2.5 Stress Intensity Factor for a Finite Specimen

The stress intensity factor solution for some basic infinite media is presented in equation (2). The solution presented there is valid when the crack length is much smaller than the in-plane dimensions of the specimen. If the crack length is similar in magnitude to characteristic specimen dimensions, however, the stress intensity factor becomes influenced by the geometry and size of the part. In these cases analytical results are difficult to obtain and thus numerical methods (e.g. the finite element method) are employed to calculate stress intensity factors at the cracks in finite size media.

2.5.1 Stress Intensity Factor by the Finite Element Method

The finite element method has become a useful technique for solving fracture mechanics problems of various types including those of the linear elastic or elasto-plastic variety. Finite element approaches to fracture mechanics problems can be described as either direct or indirect. In the direct method, stress intensity factors are calculated directly from the solution, while in the indirect method, the strain energy release rate is calculated and stress intensity factors are inferred from it. Among the two, the indirect

technique is the most popular and efficient. There are several methods discussed in the literature for evaluating the energy release rate for finite element models. These methods are based on changes in potential energy, compliance or stiffness for the crack before and after crack extension. Irwin created a technique called the Crack Closure Integral in which he defined the energy released as

$$G_I da = 2\int_0^{da} \frac{1}{2}\sigma_{yy} u_y dx. \tag{9}$$

The above expression simply states that the work done by σ_{yy} (the far field stresses in the transverse direction) in closing the extended crack length *da* by the displacement u_y is equal to the energy released, $G_I.da$. A graphical depiction of these quantities is shown in Fig. 2.3. The factor 2 in the preceding expression signifies that both the crack surfaces are taken into account.

This method is not widely used, perhaps because it required two separate analyses to determine the stress intensity factor K_I. Regardless, this method is based on the assumption that the energy ΔE released when the crack is extended from a to $a+\Delta a$, is equal to the energy required to close the crack between location l and i shown in Fig. 2.4(a). For a crack modeled with two-dimensional, four-noded elements as shown in Fig. 2.4(a), the work ΔE required to close the crack along one element side can be expressed as

$$\Delta E = \frac{1}{2}\left[F_y.\Delta v_l + F_x.\Delta u_l\right], \tag{10}$$

where F_x and F_y are the shear and opening forces at the crack-tip node l and Δv^l and Δu^l are the differences in the shear and opening displacements at node l shown in Fig. 2.4(b).

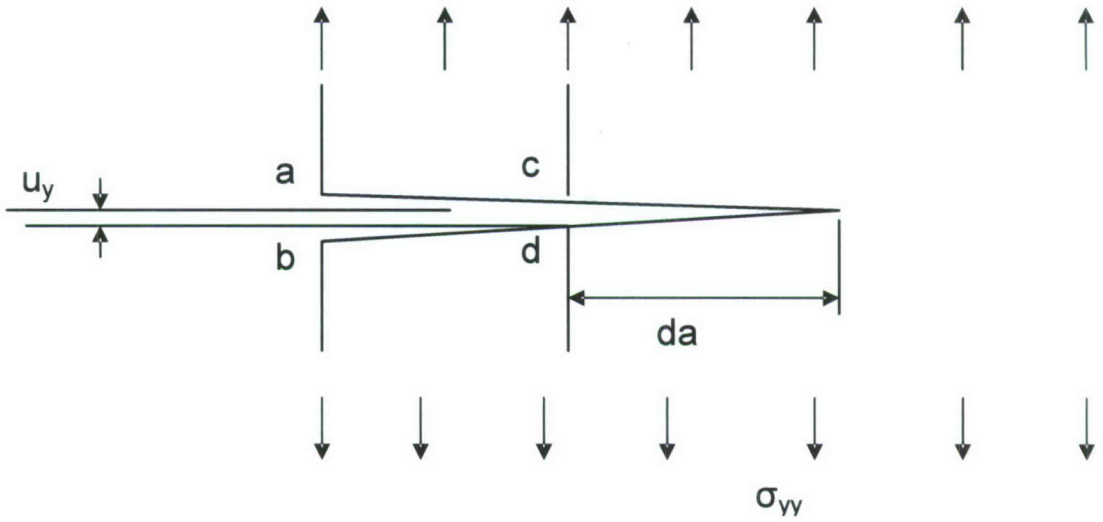

Figure 2.3: Depiction of crack closure integral.

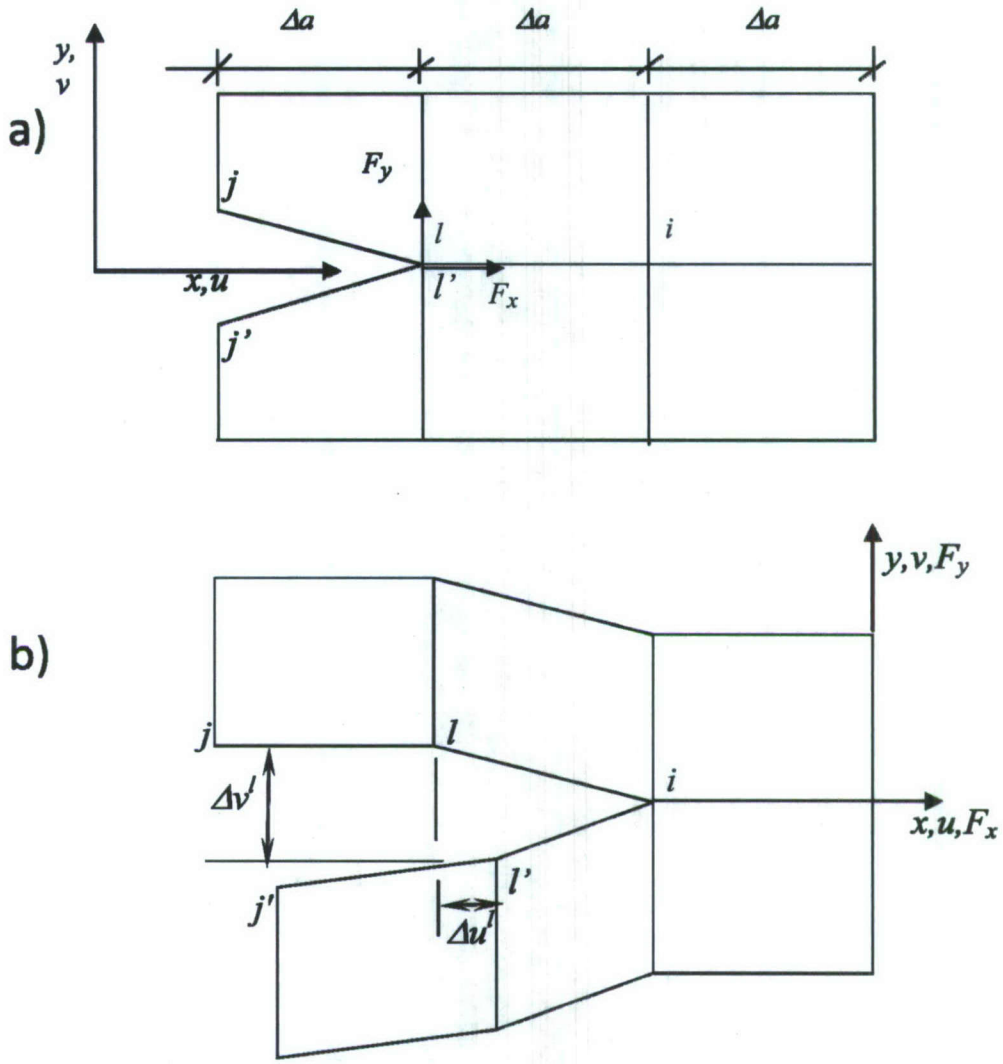

Figure 2.4: Irwin's Crack Closure Technique, a) step-I and b) step-II.

In the first analysis, a finite element model of the cracked structure is created with the desired loads and boundary conditions, and the forces F_x and F_y are computed at the crack-tip l, shown in Fig. 2.4 (a). In the second analysis, the model is re-run with the crack being extended to $a+\Delta a$ and displacement of point l is noted. It follows that if the forces F_x and F_y were not present, then point l would displace by the amounts Δv^l and Δu^l in the vertical and horizontal directions respectively.

To eliminate the need for multiple analyses the crack closure technique is modified in such a fashion that only one analysis is required to obtain values of both K_I and K_{II}. This method is called the Modified Crack Closure Technique and it also falls into the category of indirect methods. The method does not require the calculation of stresses and conventional constant strain elements can be used successfully.

In Fig. 2.4(a), if F_y^l and F_x^l are vertical and horizontal forces at node l before extension and u^l, $u^{l'}$, v^l and $v^{l'}$ are the respective horizontal and vertical displacements of nodes l and l' after crack extension (Fig. 2.4(b)), then equation (10) can be manipulated to express the strain energy release rate in terms of nodal quantities, giving

$$G_I = \frac{1}{2\Delta a} F_y^l (v^l - v^{l'}),$$
$$G_{II} = \frac{1}{2\Delta a} F_x^l (u^l - u^{l'}). \tag{11}$$

The superscripts in this equation denote the node location as shown in Fig. 2.4. For the modified crack closure technique, a very small Δa is required and should be on the order of $\Delta a/a < 0.05$. Rybicki and Kanninen (1977) assumed that if $\Delta a/a$ is small and Δa kept the same before and after the crack-tip, the nodal displacements at l and l' after crack

extension can be approximated by the nodal displacements at j and j' before the crack extension. Thus, equation (11) can now be written as

$$G_I = \frac{1}{2\Delta a} F_y^l (v^j - v^{j'}),$$
$$G_{II} = \frac{1}{2\Delta a} F_x^l (u^j - u^{j'}). \tag{12}$$

With this method, only a single analysis needs to be run in order to obtain K_I and K_{II} for any crack in the structure.

2.5.1.1 Correction for Unequal Element Lengths at the Crack Tip

While evaluating F_y^l and F_x^l it is convenient to maintain $l_1 = \Delta a$ and also to keep elements (1), (2), (3) and (4) the same size (Fig. 2.5). It is not difficult to maintain equal length elements around the crack tip by controlling the finite element mesh. One might do this by simply creating a square mesh partition around the crack tip. However, when unequal length elements cannot be avoided, a modification to equation (12) allows one to use elements of differing lengths around the crack tip. Referring to Fig. 2.5, $\underline{F}_x$ and $\underline{F}_y$ are the required nodal forces at i for $l_1 = \Delta a$, but for the case of unequal element lengths this is not exactly true and F_x and F_y are simply the nodal forces obtained from the finite element model. To obtain the correct required nodal forces, the following correction factors can be used (Rybicki and Kanninen, 1977):

$$\underline{F}_x = \sqrt{\frac{\Delta a}{l_1}}.F_x, \quad \underline{F}_y = \sqrt{\frac{\Delta a}{l_1}}.F_y. \tag{13}$$

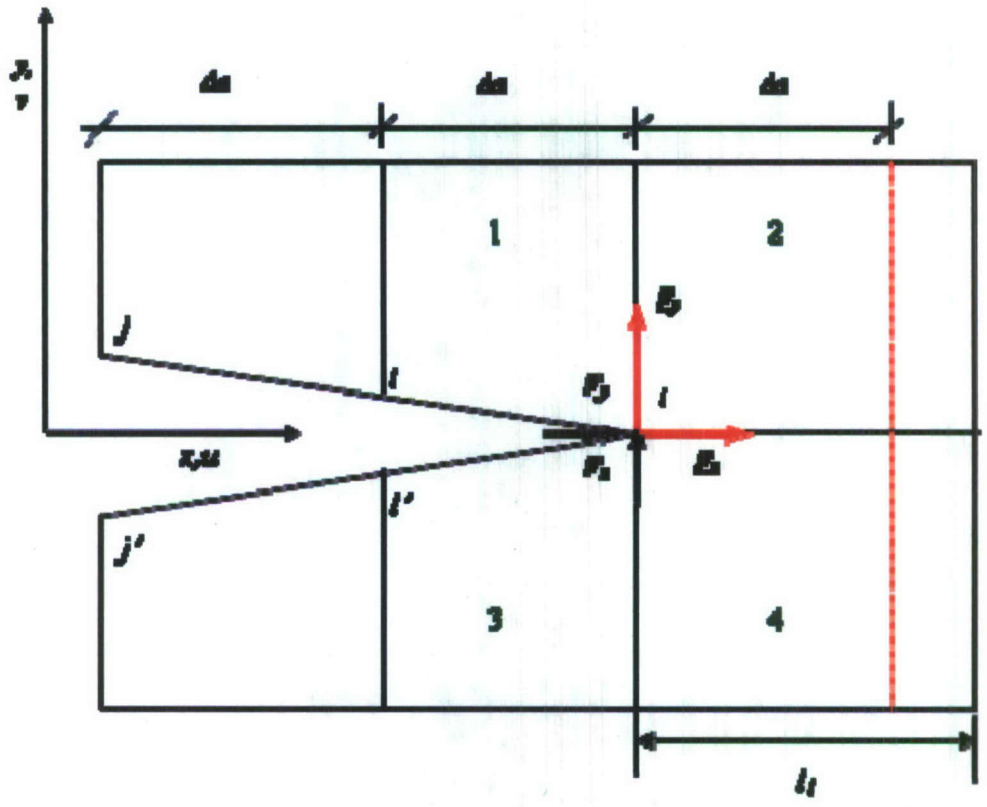

Figure 2.5: Correction method in the Modified Crack Closure Technique for unequal length elements.

Substituting these expressions into equation (12) gives the required result, which is

$$G_I = \frac{1}{2\Delta a} F_y^l (v^j - v^{j'}).\sqrt{\frac{\Delta a}{l_1}},$$
$$G_{II} = \frac{1}{2\Delta a} F_x^l (u^j - u^{j'}).\sqrt{\frac{\Delta a}{l_1}}. \tag{14}$$

2.5.1.2 Relationship between G and K by Crack Closure Method

As stated by Irwin, if a crack extends by a small amount Δa, the change in energy in the process is equal to the work required to close the crack to its original length. This can be expressed as

$$G = \lim_{\Delta a \to 0} \frac{1}{2\Delta a} \int_0^{\Delta a} \sigma_y .v.dr + \lim_{\Delta a \to 0} \frac{1}{2\Delta a} \int_0^{\Delta a} \tau_{xy} .u.dr, \tag{15}$$

where σ_y and τ_{xy} are the tensile and shear stresses, respectively, at node l before extension and u and v are sliding and opening displacements at node l after the crack extension (Fig. 2.4(a)). The first and second parts of the total energy release rate G are essentially two separate contributions for mode-I and mode-II, respectively. Noting that Westergaard's expressions for σ_y, τ_{xy}, u and v are

$$\sigma_{yy} = \frac{K_I}{\sqrt{2\pi r}} Cos\frac{\theta}{2}\left(1 + \sin\frac{\theta}{2}.\sin\frac{3\theta}{2}\right), \qquad v = \frac{K_I}{8\mu\pi}\sqrt{2\pi r}\left[(2\kappa - 1)\sin\frac{\theta}{2} - \sin\frac{3\theta}{2}\right],$$
$$\tau_{xy} = \frac{K_I}{\sqrt{2\pi r}} \sin\frac{\theta}{2}\cos\frac{\theta}{2}\cos\frac{3\theta}{2}, \qquad u = \frac{K_I}{8\mu\pi}\sqrt{2\pi r}\left[(2\kappa - 1)\cos\frac{\theta}{2} - \cos\frac{3\theta}{2}\right].$$

and then substituting these expressions into equation (15) will give

$$G_I = \frac{\kappa + 1}{8\mu} K_I^2, \; G_{II} = \frac{\kappa + 1}{8\mu} K_{II}^2 \tag{16}$$

$$\kappa = \begin{cases} 3-4\nu & \text{plane strain} \\ \dfrac{3-\nu}{1+\nu} & \text{plane stress} \end{cases} \qquad \text{(16-a)}$$

2.5.2 Stress Intensity Factor and its Dependence on Geometry

Obtaining closed form solutions for the stress intensity factors K_I and K_{II} for the lap joint configuration would entail the solution of complex two-dimensional elasticity problem. It is particularly difficult to obtain an analytical solution to the governing partial differential equations due to the hard contact conditions at the interface of the non-welded regions of the joint. In the present work, the finite element package ABAQUS (v. 6.6) is utilized to evaluate the stresses and the stress intensity factors at the crack tips. A two-dimensional model with plane strain conditions is analyzed with a very fine mesh consisting of approximately 300,000 elements. The non-welded interface between the plates is modeled with hard normal contact conditions with negligible friction. The left end of the lower plate is held fixed.

The stress intensity factors at the notch tips are computed using the Modified Crack Closure Technique and the finite element method. In the MCC technique, a regular mesh of four-noded quadrilateral elements is used around the crack tip. According to equations (12) and (16), the stress intensity factors are computed from the nodal forces at the notch tip and the relative displacement of the nodes adjacent to the notch tip.

By executing several analyses with different joint dimensions and load types it is found that the stress intensity factors at the notch tips vary with the change in the dimensional parameters (w, a, H and h) of the joint. This fact gives credence to the statement in Section 2.4 that stress intensity factors are functions of the geometric

dimensions of the lap joint and the nature of the applied loads. To aid in determining the dependence of the stress intensity factor on joint dimensions, the four aforementioned parameters are normalized with respect to h, thus reducing the number of variables from four to three. Similar to β in equation (2), a geometric configuration factor f is defined which depends on the three non-dimensional geometric variables,

$$f_i^{M^+,l}\left(\frac{H}{h},\frac{w}{h},\frac{a}{h}\right). \tag{17}$$

where the subscript $i = I, II$ denotes the fracture mode. The first superscript of the function f_i indicates the direction of the applied moment which can either be M^+ for a positive moment (counter-clockwise) or M^- for a negative moment (clockwise). The second superscript of the function f_i indicates the location of the notch which can either be l for the notch on the left edge of the weld or r for the notch on the right edge. In a work by Suo and Hutchinson (1990), an analytical solution for the stress intensity factors for a semi-infinite crack between two infinite elastic layers was obtained that provided some insight as to how to properly construct a mathematical model for defining K_I and K_{II}. Based on the functional form of the stress intensity factors obtained by Suo and Hutchinson (1990) and other dimensional considerations, the following expressions for the stress intensity factors are assumed:

$$K_i = \frac{M}{h^{3/2}} f_i^{M^+,l}\left(\frac{H}{h},\frac{w}{h},\frac{q}{h}\right), \tag{18}$$

where M is the magnitude of the applied moment and f_i are previously defined geometric configuration factors. In the present work, the functions f_i are evaluated using the finite element method at discrete values of the geometric parameters. The values obtained from

the parametric studies are later used to construct a three-dimensional metamodel to predict stress intensity factors for arbitrary joint dimensions.

2.5.3. Critical Load Scenario for a Fixed Joint Dimension

The objective of this study is to check if LEFM is valid for our mathematical model. To do that, one needs to know the plasticity effects in a specific joint due to application of the critical moment. In order to obtain a converged critical moment of a joint, a convergence study is performed. A particular joint geometry (H/h = 1, w/h = 0.6, a/h = 1) is selected with upper plate thickness h = 1", and critical moment is calculated utilizing the stress intensity factors obtained by applying the unit positive moment. The finite element model with boundary conditions and load is shown in Fig. 2.6. The critical moment thus obtained is applied to the joint and a new critical moment is evaluated based on new stress intensities. The process is iterated until convergence is established and variation in the results reaches less than 0.01%. Data corresponding to this study is tabulated and shown in Table 2.1. A graphical depiction of the convergence results is shown in Fig. 2.7. According to the assumed linear relation between stress intensity factor and applied load (shown in equation (18)), if the stress intensity factors obtained at unit load be extrapolated, one should get very close values to the stress intensity factors obtained at critical load. However, these values would not be close due to the non-linearity enforced due to contacts.

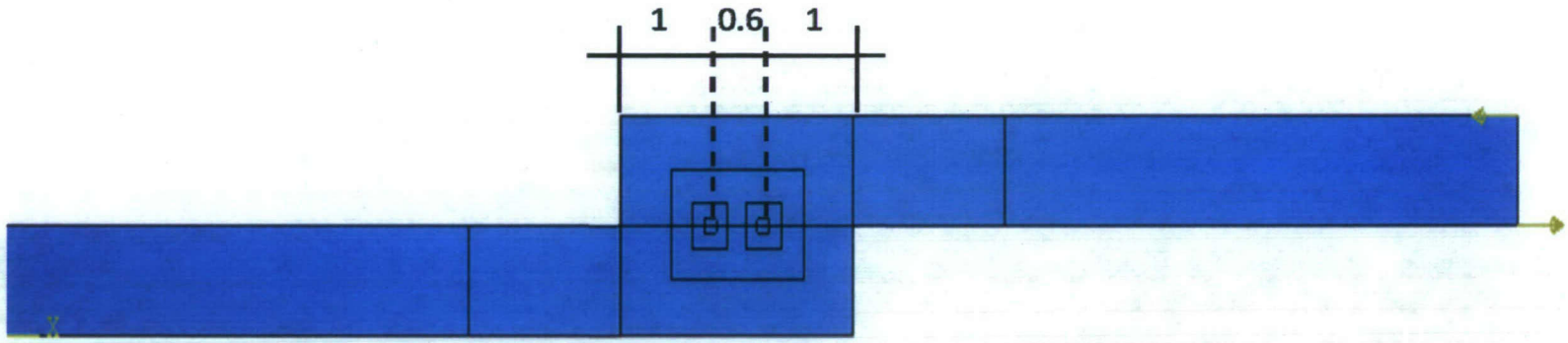

Figure 2.6: Finite element model of the joint (*H/h* = 1, *w/h* = 0.6, *a/h* = 1).

M_o	K_I	K_{II}	K_I/M_o	K_{II}/M_o	Mc	Iteration	Variation
1	2.113	1.299	2.113	1.299	37085	1	
37085	82320	47380	2.220	1.278	36288	2	2.196
36288	80470	46390	2.218	1.278	36299	3	0.030
36299	80480	46400	2.217	1.278	36305	4	0.017
36305	80300	46400	2.212	1.278	36357	5	0.143
36357	80550	46470	2.216	1.278	36321	6	0.099
36321	80510	46430	2.217	1.278	36309	7	0.033
36309	80490	46400	2.217	1.278	36310	8	0.003

Table 2.1: Convergence study of critical moment for the joint ($H/h = 1$, $w/h = 0.6$, $a/h = 1$).

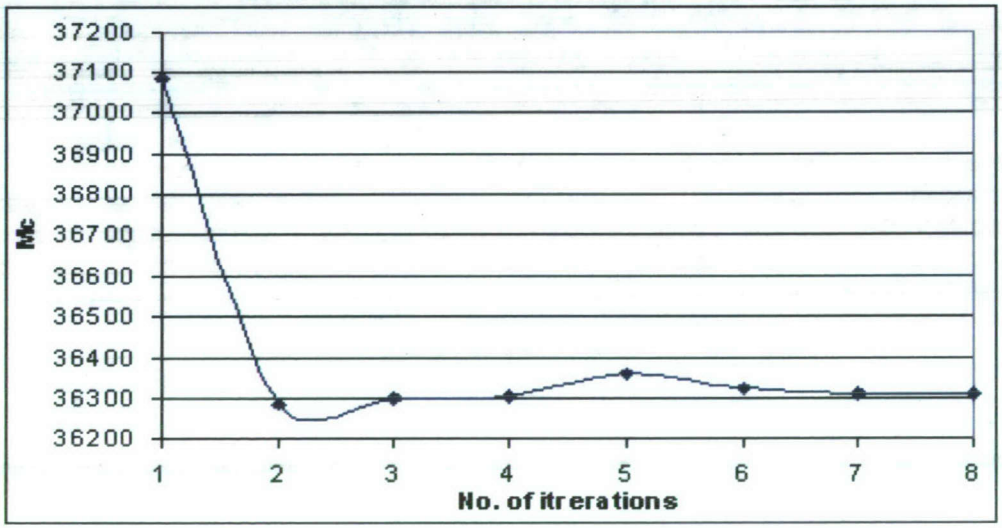

Figure 2.5: Convergence of the critical moment for the joint.

is on finding the amount of load which should be applied to the joint which gives lowest extrapolated error but would still follow LEFM principles. If the stress intensities at an initial moment of M_o = 1 lb-in/in are extrapolated, it is seen that the actual stress intensities for mode-I at the true critical load are 4.9% higher than those obtained from the extrapolation. This explains that for this particular geometry, extrapolating the results of a unit applied moment gives underestimated fracture calculations. However, if the analysis is re-run with higher load, the extrapolated stress intensity factors come closer to the actual values obtained at that load. A set of such analyses have been performed on the same geometry with increasing moments up to the critical moment of the joint, to recognize the appropriate moment to be applied for better predictions. The results of this study are shown in Tables 2.2(a) and (b) for K_I and K_{II} respectively.

As seen in the tables, each load step is selected one by one and stress intensities are extrapolated based on the selected load. Errors from the true stress intensity values are computed in each increment case. With these results in hand, it is then at the discretion of the analyst as to how much error can be tolerated. Selecting the moment of 20,000 lb-in/in, gives 1.9% underestimated and 0.7% overestimated values for K_I and K_{II} respectively. Prior to moving forward, one must check to see if LEFM is still applicable. Von Mises stress contour plots have been obtained for 4147 steel in order to check the plastic zone size at around 55% of the critical moment (20,000 lb-in/in) of the joint.

(a)

				Extrapolated-K_I									
Mo	K_I	K_I/Mo	Mc	K_I,Mo=1	Error%	K_I,Mo=100	Error%	K_I,Mo=5000	Error%	K_I,Mo=10000	Error%	K_I,Mo=20000	Error%
1	2.113	2.113	36878										
1000	2114	2.114	37098	2113	0.047								
5000	10650	2.130	36963	10565	0.805	10570	0.757						
10000	21440	2.144	36860	21130	1.467	21140	1.419	21300	0.657				
20000	43500	2.175	36613	42260	2.934	42280	2.886	42600	2.113	42880	1.446	Selected	
30000	65850	2.195	36488	63390	3.881	63420	3.832	63900	3.052	64320	2.379	65250	0.920
36310	80490	2.217	36308	76723.03	4.910	76759.3	4.860	77340.3	4.073	77848.64	3.393	78974.25	1.919

(b)

				Extrapolated-K_{II}									
Mo	K_{II}	K_{II}/Mo	Mc	K_{II},Mo=1	Error%	K_{II},Mo=100	Error%	K_{II},Mo=5000	Error%	K_{II},Mo=10000	Error%	K_{II},Mo=20000	Error%
1	1.299	1.299	36878										
1000	1297	1.297	37098	1299	-0.154								
5000	6475	1.295	36963	6495	-0.308	6485	-0.154						
10000	12920	1.292	36860	12990	-0.539	12970	-0.386	12950	-0.232				
20000	25740	1.287	36613	25980	-0.924	25940	-0.771	25900	-0.618	25840	-0.387	Selected	
30000	38440	1.281	36488	38970	-1.360	38910	-1.208	38850	-1.055	38760	-0.826	38610	-0.440
36310	46400	1.278	36308	47166.69	-1.625	47094.1	-1.474	47021.45	-1.322	46912.52	-1.093	46730.97	-0.708

Table 2.2: Moment selection: Extrapolated stress intensity factor for a) mode-I b) mode-II for different initial positive moments, and their variation from actual values obtained.

the plastic zone is larger (0.059") than the left lobe (0.0243") due to the apparent stress distribution. It is quite obvious but worth mentioning that the plastic zone size will increase for a more ductile material.

Gdoutos (2005) has derived a relation for the plastic zone radius as a function of θ which is in the form

$$r_p(\theta) = \frac{1}{2\pi\sigma_y^2}\left[\begin{array}{l} K_I^2\cos^2\frac{\theta}{2}\left\{(1-2\nu)^2+3\sin^2\frac{\theta}{2}\right\}+K_I K_{II}\sin\theta\left\{3\cos\theta-(1-2\nu)^2\right\}+ \\ K_{II}^2\left\{3+\sin^2\frac{\theta}{2}\left\langle(1-2\nu)^2-9\cos^2\frac{\theta}{2}\right\rangle\right\} \end{array}\right]. \quad (19)$$

This relation is valid for mixed mode, plane strain conditions. Fig. 2.9 depicts the shape of the theoretical plastic zone in polar coordinates for the stress intensities obtained at an applied moment of 20,000 lb-in/in. As expected, the zone size changes for different material strengths as evinced by the fact that r_p depends on the yield strength (σ_y). The theoretical plastic zone size and shape is compared with the one shown in the contour plots from the joint analysis. The gross dimensions of the plastic zone computed from the analytical and finite element models are relatively similar.

a)

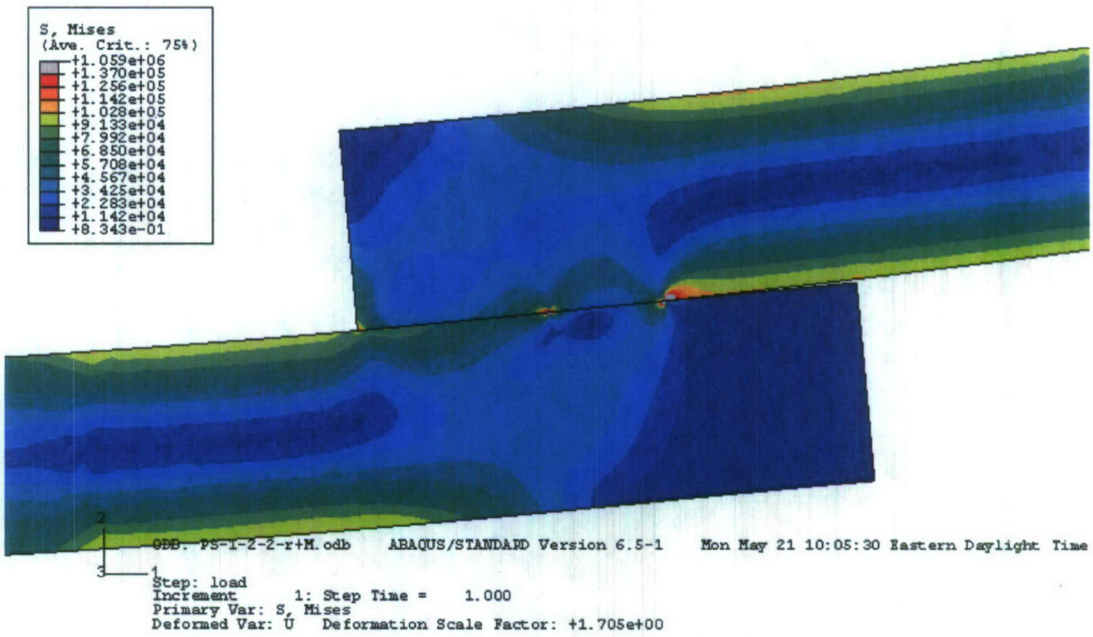

b)

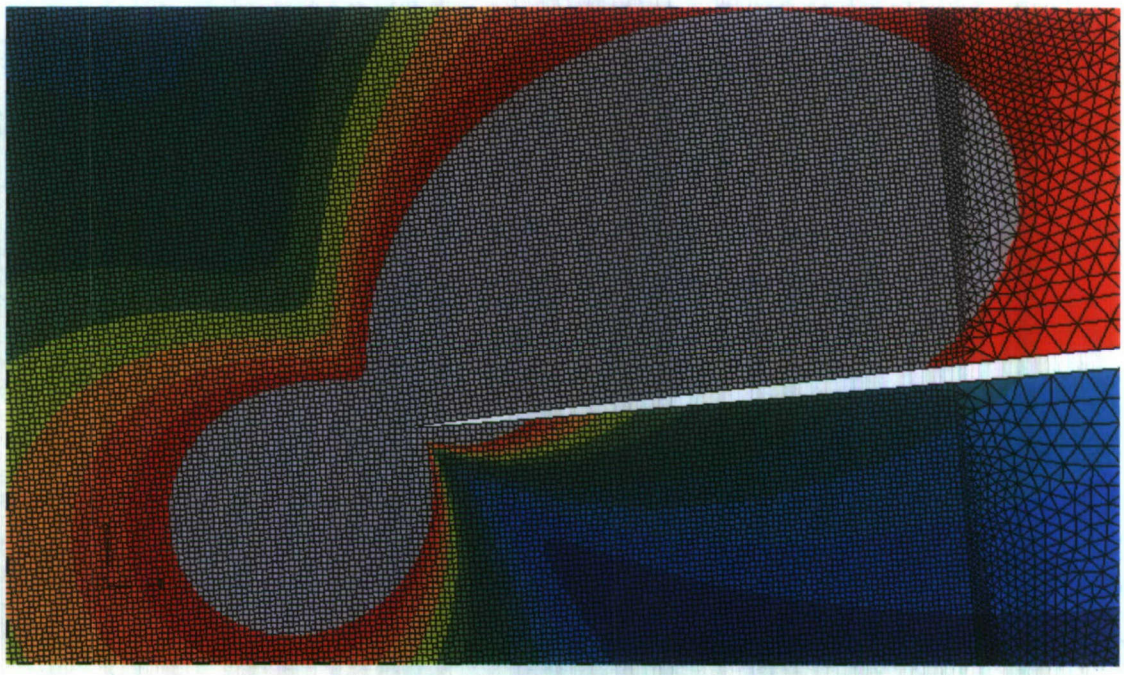

Figure 2.8: Contour plot showing gray plastic zone for 4147 steel of yield strength 137ksi.

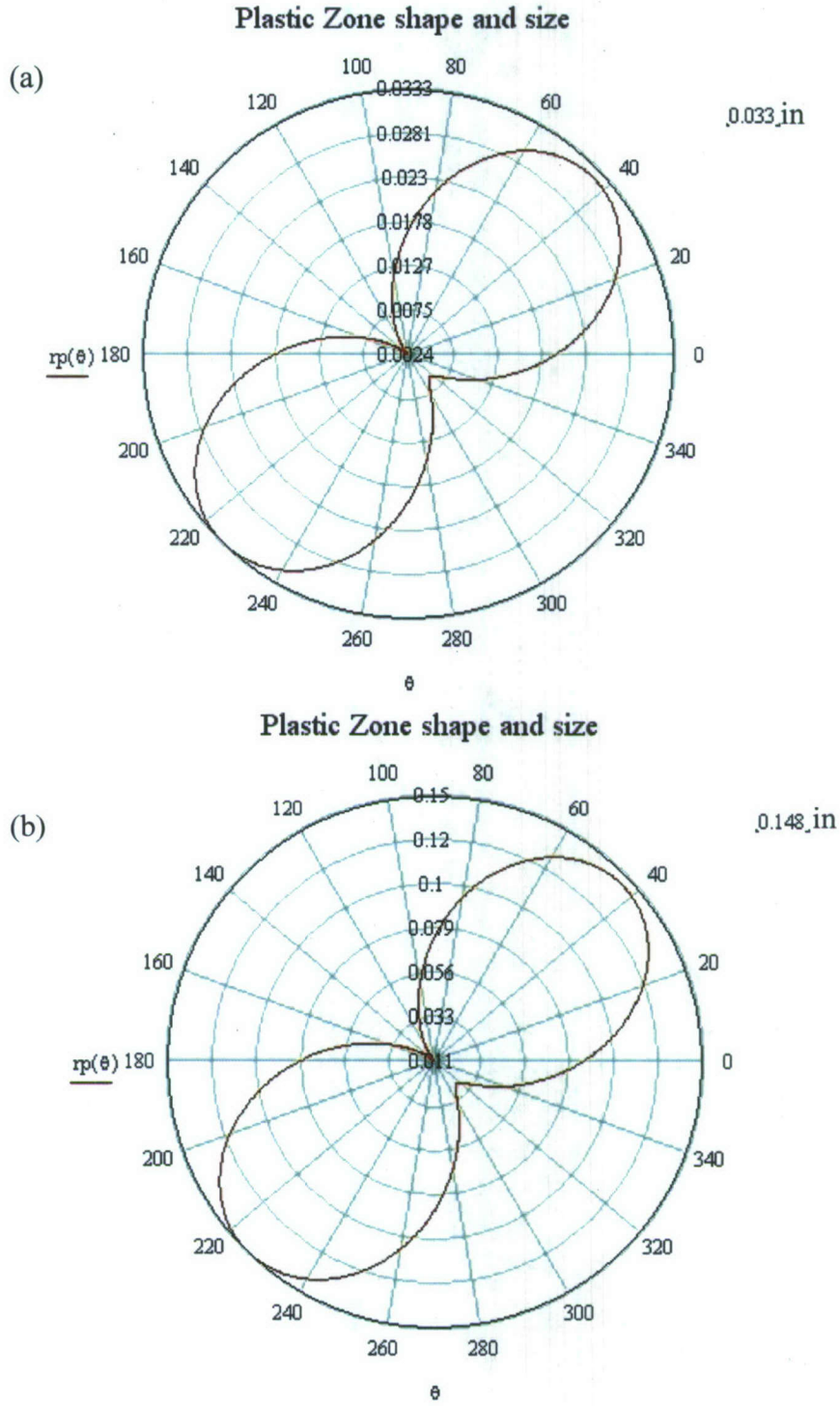

Figure 2.9: Theoretical plastic zone shape and size for: a)4147 steel and b)HSLA-65 steel.

Since the plastic zone size is seen within $1/50^{th}$ of the thickness dimensions of the joint, one can safely use LEFM for 4147 steel.

2.6 Finite Element Modeling

2.6.1 Analysis

A commercially available finite element package ABAQUS (2005), is used to perform numerical modeling. Some of the major modeling details are provided in this section to provide information so that this work can be duplicated using other finite element packages. A two-dimensional model is prepared by constructing two separate plates and joining them in the middle of the overlap to achieve the desired joint configuration, as already shown in Fig. 2.1. To simulate the weld, the nodes on the welded length of the overlapped plates are assigned the same degrees of freedom (Fig. 2.10). The non-welded overlapped regions have been defined as frictionless hard surfaces to ensure non-penetrating contact. Both the top and the bottom plates are assumed to be of same isotropic material, steel, with Young's modulus and Poisson's ratio of 29.7×10^3 ksi and 0.29 respectively. The finite element model is fixed at the left edge of the lower plate and point loads are applied at the right free edge of the upper plate to simulate a couple (refer Fig. 2.6)

A combination of triangular (continuum, plane-strain, 3-noded-CPE3, away from the notches) and quadrilateral (continuum, plane-strain, 4-noded, reduced integration, hourglass control-CPE4R, near the notch tips) elements are used, each possessing linear

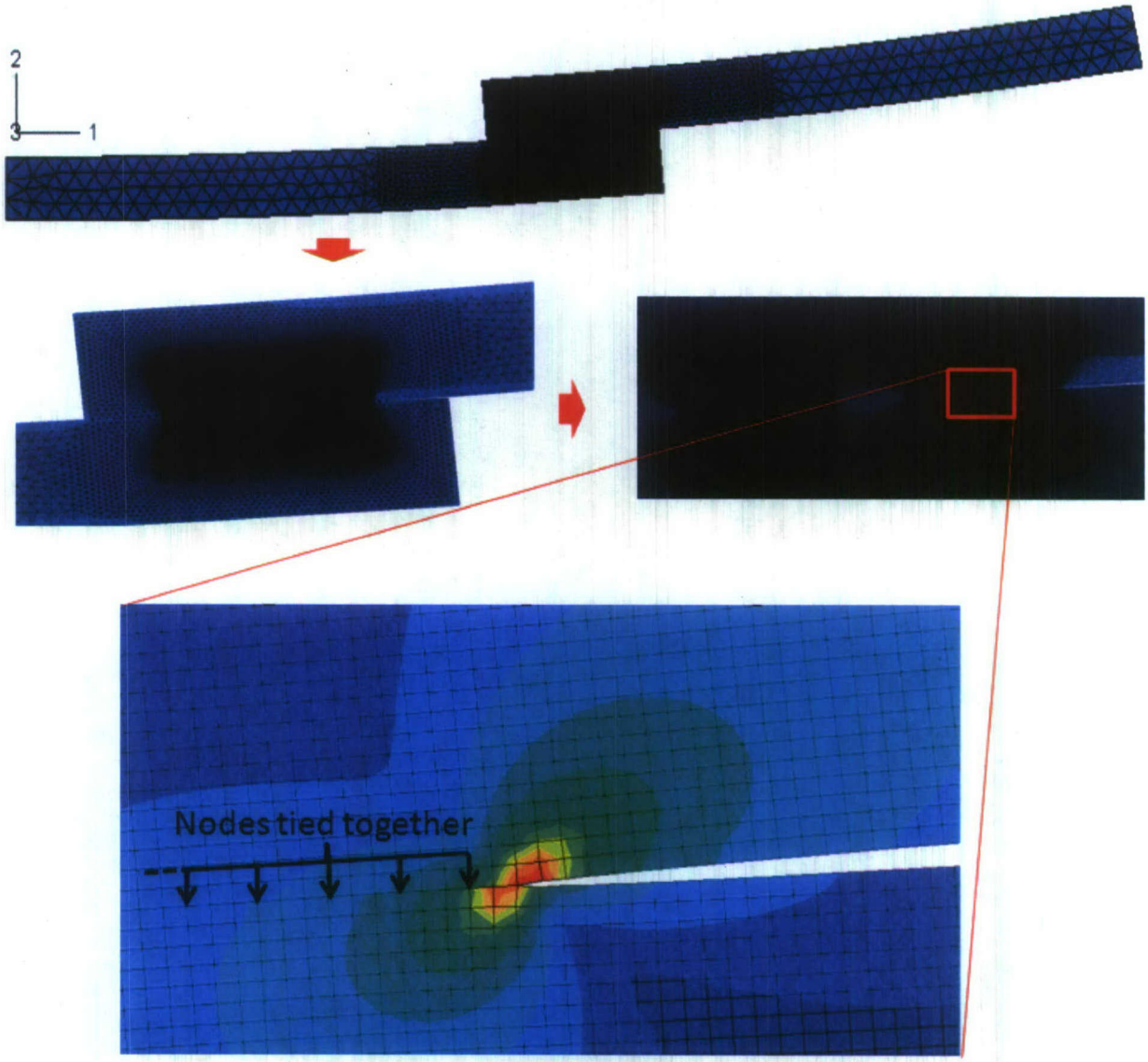

Figure 2.10: Deformed finite element model of the joint (H/h=1, w/h=0.6 and a/h=1).

shape functions. This combination is used to reduce the number of elements in each model and reduce the analysis runtime. The selection of elements, their number and their sizes will be discussed in detail in Section 2.6.2 and 2.6.3. The geometry and properties are defined and the model is set to run under plane strain conditions. Concerning the solution method, ABAQUS/Standard provides its own algorithm of automatic incrementation instead of asking the user to select among Newton or Modified Newton's methods. This default setting provides reliable results and a fast convergence rate. A direct matrix solver is used at each iteration which reduces the solution time and space requirements by taking maximum advantage of matrix sparsity. It is important that the appropriate output options are selected so that nodal forces and displacements can be retrieved at the crack tips.

2.6.2 Element Type

ABAQUS provides several different types of two-dimensional elements. For structural applications these include plane stress elements and plane strain elements. Plane stress elements can be used when the thickness of a body or domain is small relative to its lateral (in-plane) dimensions. Plane strain elements can be used when it is safe to assume that the strains in a loaded body or domain are functions of planar coordinates only, and that the out-of-plane normal and shear strains are equal to zero. Plane strain elements must be defined in the X-Y plane and all loading and deformation is restricted to this plane as well. This modeling method is generally used for bodies that are very thick relative to their lateral dimensions, like the model under consideration.

There are five factors to characterize the behavior of an element. These are namely the element family, the number of degrees of freedom, the number of nodes, the

element formulation type and the integration procedure used. Fig. 2.11 shows the element families available in ABAQUS that are most commonly used in a stress analysis. For our analysis, where the plates are considered to be of infinite width and it is important to model contacts, two-dimensional continuum elements CPE4R and CPE3 are selected, where the first letter or letters indicate the element family. For example, CPE4R is a continuum, plane strain element (C – continuum, PE – plane-strain). The degrees of freedom are the fundamental variables calculated during the analysis. For a displacement/stress element the degrees of freedom are the translations. At any point in the element other than the nodes, the displacements or other degrees of freedom are obtained by interpolating from the nodal degrees of freedom. Usually the interpolation order is determined by the number of nodes used in the element. Elements that have nodes only at their corners, such as a rectangular 4-node 2D continuum element, use linear interpolation in each direction and are labeled linear elements or first-order elements.

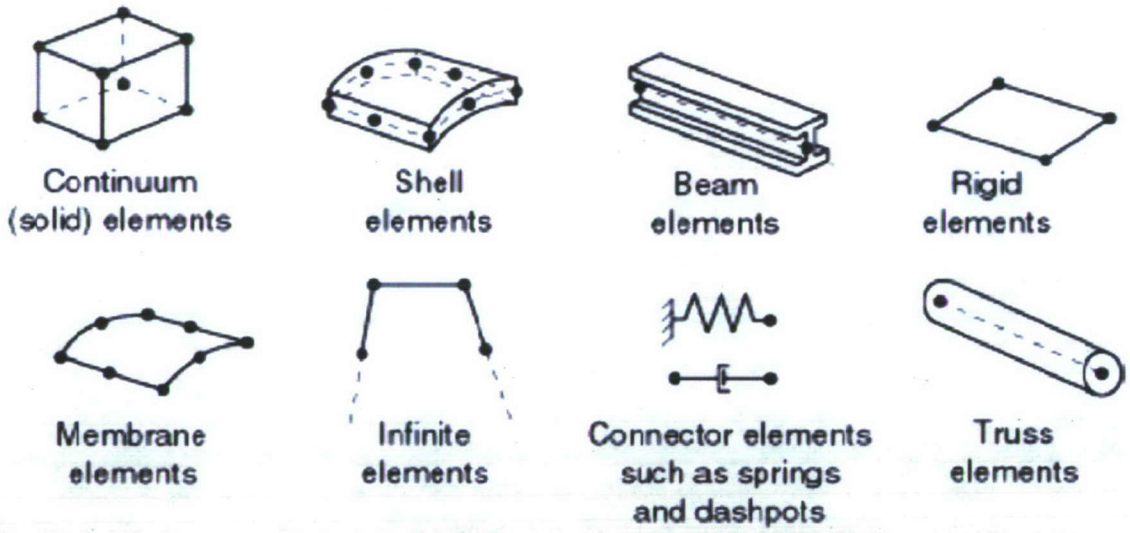

Figure 2.11 Commonly used element families.

The formulation of an element refers to the mathematical theory used to define the element's behavior. Since adaptive meshing techniques are not used in our work, all of the displacement/stress elements used here are based on a Lagrangian formulation, i.e. the element deforms with the material. With this type of formulation large scale deformations cannot be modeled correctly.

The finite element program ABAQUS uses numerical techniques to integrate various quantities over the volume of each element, thus allowing complete generality in material behavior (Section 3.2.1, ABAQUS Theory Manual). Using Gaussian quadrature for most elements, including CPE4R and CPE3, ABAQUS evaluates the material response at each integration point in each element. Some continuum elements, such as CPE4R, have the ability to use either full or reduced integration. Reduced integration decreases the number of constraints introduced by an element when there are internal constraints in the continuum theory being modeled, such as incompressibility or the Kirchhoff transverse shear constraints in the case of solid elements used for analyzing bending problems. In such applications fully integrated elements will "lock" and will exhibit a very stiff response, thus giving very poor results. In these cases, the reduced integration version of an element will often work well. The letter R at the end of an ABAQUS element name signifies a reduced integration element. Although reduced integration lowers the cost of forming an element, the drawback is that except in one-dimensional and in axisymmetric geometries modeled with higher than first-order elements, the element stiffness matrix will be rank deficient. This often creates singular or hourglass modes in the response. When reduced integration is used in first-order elements (4-node quadrilateral), hourglassing often makes the elements unusable unless

the phenomena is controlled. In ABAQUS, artificial stiffness and damping methods are used to control the hourglass modes in these elements.

The CPE4R and CPE3 elements are applicable for many applications. These displacement/stress elements can be used in linear or complex nonlinear mechanical analyses that involve contact, plasticity, and/or large deformations.

2.6.3 Convergence Study

A convergence study is required at several steps of the process to verify that the mesh being used is sufficiently refined. The first study is performed to assess the accuracy of the Modified Crack Closure Technique. This is performed using two separate center crack plate models subjected to the remotely applied uniform normal and shear tractions for K_I and K_{II} respectively. The dimensions of the plate in the model are made to be much larger than the crack width $2a$, thus allowing the use of analytic solutions for infinite media for comparison purposes. The element types and analysis procedure used are the same as was discussed in Section 2.6.1 and 2.6.2. The finite element solution has been compared with the analytic values and the results of the study are presented in Tables 2.3(a) and (b). The errors in the finite element results are plotted as a function of element size in Fig. 2.12.

Referring to Table 2.3(a), a mesh size of $\Delta a/a = 0.0025$ appears to give good results for K_I, as the reported value is only 0.4% off from the analytic value. Further mesh refinement provides only diminishing gains in accuracy. Rather than decreasing the element size, one can double the partition area close to the notch tip while keeping the same element size ($\Delta a/a = 0.0025$) which reduces the error to only 0.04%. This

a) Center crack convergence study for K_I				
Ele. Size(Δa)	K_I	Analytical	Error %	Δa/a
0.003	79.013	79.461	0.564	0.015
0.0009	79.491	79.461	0.038	0.0045
0.0007	80.09	79.461	0.792	0.0035
0.0005	79.803	79.461	0.430	0.0025

b) Center crack convergence study for K_{II}				
Ele. Size(Δa)	K_{II}	Analytical	Error %	Δa/a
0.003	78.446	79.267	1.036	0.015
0.0009	78.912	79.267	0.448	0.0045
0.0007	79.499	79.267	0.293	0.0035
0.0005	79.221	79.267	0.058	0.0025

Table 2.3: Convergence study for the center crack model for: a) mode-I stress intensity factor and b) mode-II stress intensity factor.

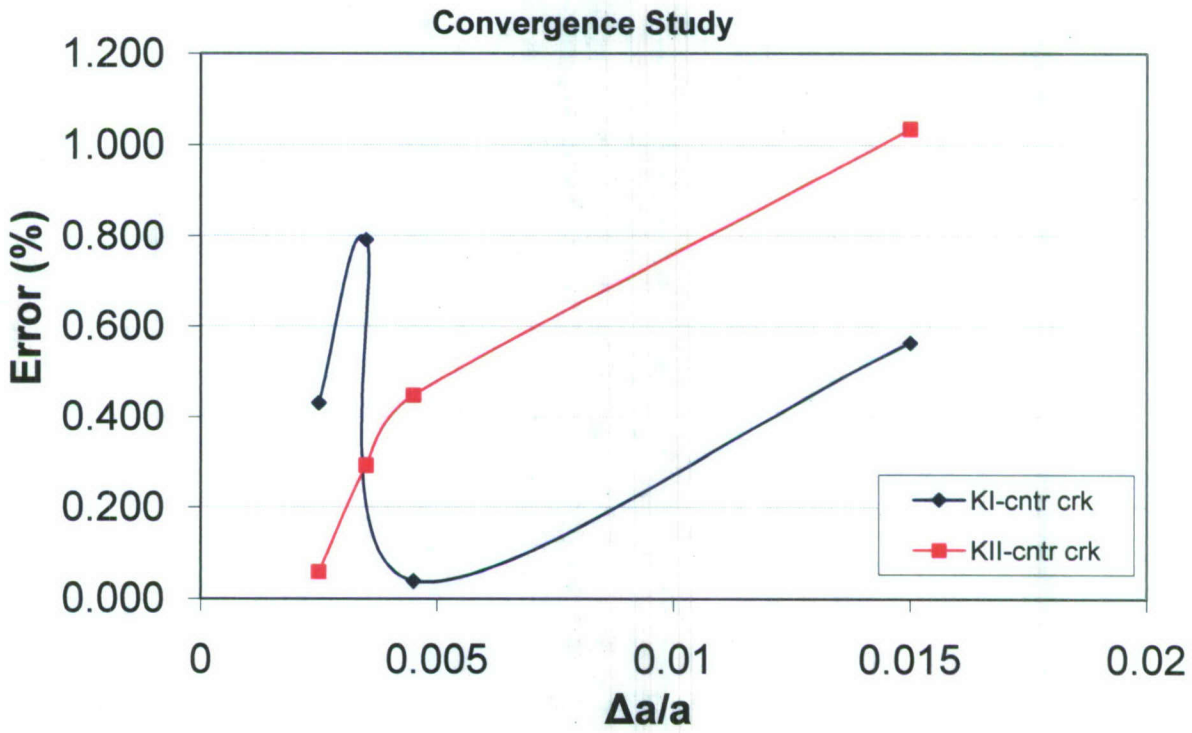

Figure 2.12: Convergence study of stress intensity factors for the center crack model.

essentially means defining a larger region around the crack tip for which there is a finer mesh. Table 2.3(b) shows the convergence for the mode-II fracture parameter, and for an element size ratio of $\Delta a/a = 0.0025$ around the notch tip, the error is only 0.06%.

To establish if the small element size and mesh partitions used in the comparison with analytic solutions would work with the connection geometry under consideration, a similar convergence study is also performed on a selected joint configuration ($H/h = 1$, $w/h = 1$, $a/h = 1$). Performing a convergence study on the model with element size ratios of 0.015, 0.0045, 0.0035, 0.0025 close to the notch tip, yields results less than 1% off from each other. Due to some technical issues with the software's meshing features, it was hard to obtain an element size ratio around the crack tip any smaller than 0.0025. Normalizing the selected element size ratio in terms of h, $\Delta a/h = 0.000625$ is obtained. In order to obtain accurate stress intensity factors for laser welded lap joints, an even finer mesh is used in subsequent analyses by choosing the normalized element size to be $\Delta a/h$=0.0005.

2.6.4 Contact Modeling

In general, structural surfaces do not penetrate each other. Thus, in order to obtain more realistic and accurate values for the stress intensity factors, it is important to incorporate contact conditions between the non-welded regions of the joint in the finite element model. It is found that neglecting contacts may provide mode-I stress intensity factors that are off by 500-600% from the true values. Typically, the mode-I stress intensity factor value is lower in the contact model since the normal reaction stresses are distributed over a wider contact region in the joint. When contact is neglected, all stresses are distributed over the narrow welded region which results in large stress intensity

factors at the notch tips. In general, the mode-II stress intensity factor value is also smaller in the contact model, though the difference is not as significant as it is for the mode-I stress intensity factor. The inclusion of contact conditions in the finite element model increases the computational cost due to the iterative solution procedure required to solve the now geometrically nonlinear problem. In addition, the inclusion of contact causes a somewhat nonlinear relationship between the computed stress intensities and the load applied. This discrepancy was discussed in detail in Section 2.5.3.

If a linear structure is subjected to different types of loads, then it is possible to evaluate the stress intensity induced by each type of load separately and then sum the solutions to get the total stress intensity at the crack tip. However, the principle of superposition is limited to only linear structures. Even though our structure is nonlinear, a simple test is performed to check if the principle of superposition can be applied on the joint geometry under consideration, thus allowing the stress intensity factor to be calculated for various loads by using results from a select few simple cases.

2.6.4.1 Superposition of Stress Intensity Factors

Various uniform loading cases are studied in literature, but in actual engineering applications, a body is often subjected to non-uniformly distributed loads. Stress intensity factors at a crack in the body under arbitrary loading conditions can be obtained using the method of superposition for linear structures. This allows the evaluation of the stress intensity factor of a desired load case using available fundamental solutions for bodies subjected to uniform forces.

In an attempt to model the real life loading situations faced by the lap joint studied herein, a small finite element modeling experiment is performed. It is assumed

that to simulate the response of the joint to the desired variety of arbitrary loads, the results from only two types of fundamental loads, moment and axial loads, is required. By superposition of the stress intensity factors obtained due to these loads separately, one can compute the stress intensity factors at the notches due to any linear combination of these loads. Consider a lap joint configuration fixed at the left end of the lower plate, as shown in the Fig. 2.13(a). The stress intensities in this joint can be obtained by superimposing the solutions of the following two problems, as illustrated in Figs. 2.13(b) and (c).

A joint with dimensions of $H/h = 2.5$, $w/h = 0.6$, and $a/h = 1$ is selected. Finite element models are made and stress intensity factors for mode-I and II are computed for the left and right notches, for both the loading conditions (a) and (b) assuming unit tensile force P, with contact conditions in effect. Table 2.4(a) shows the results obtained for K_I and K_{II} values at the left and right notches of the joint. It shows that there is a large discrepancy between the superimposed and directly computed mode-I stress intensities, the reason for which can be attributed to the nonlinearity created by the contact conditions. To ascertain this reasoning, the contact conditions were removed from all the models and the analyses were rerun. Table 2.4(b) displays the results obtained for the linear models. The results verify that superposition works for the models without contact. This study proves that including contact phenomena induces geometric nonlinearity in the connection. Therefore, the principle of superposition cannot be

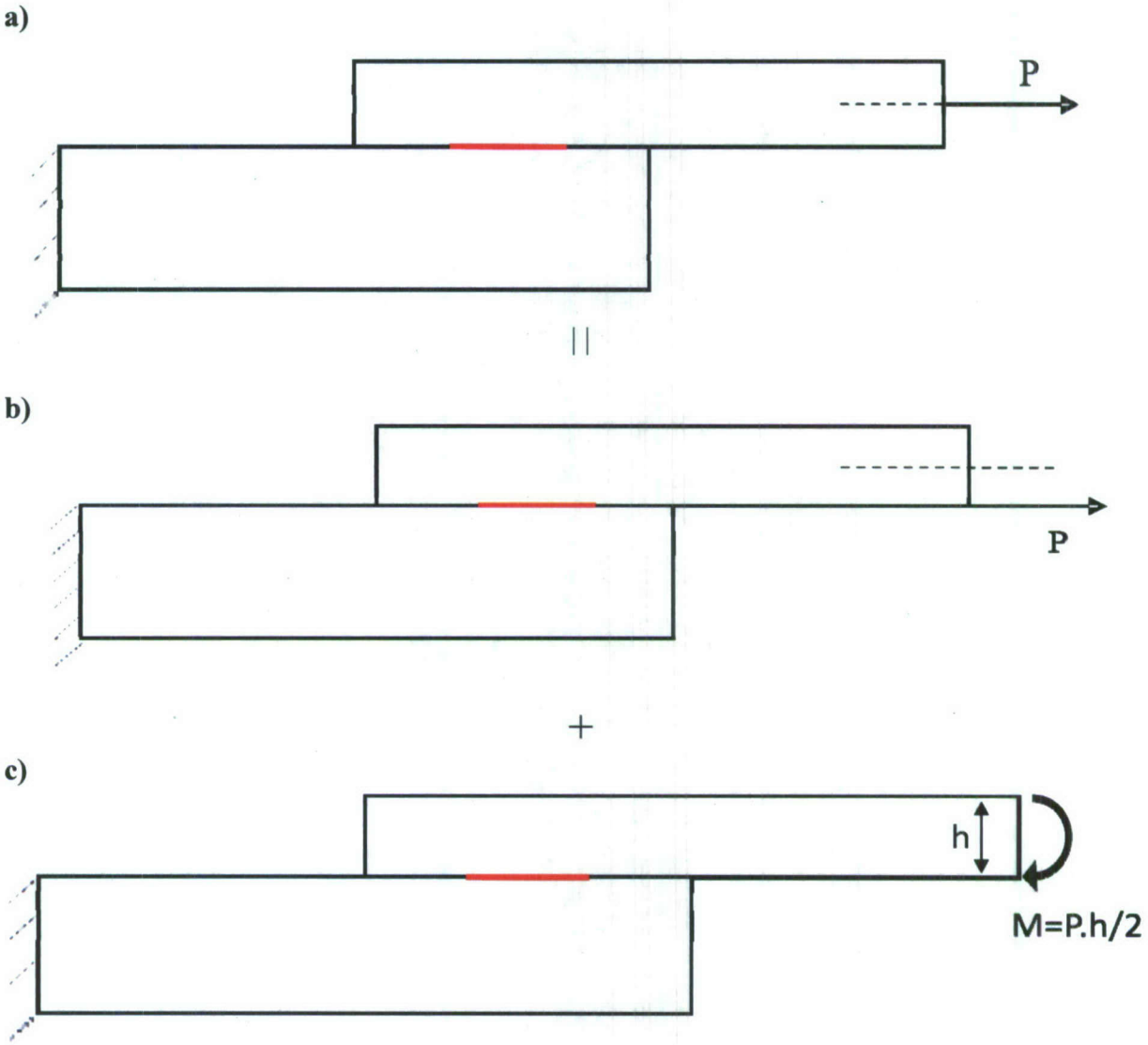

Figure 2.13: Superposition of models, for computing stress intensity factors of the joint under combined loading.

a)

With Contacts	Left end		Right end	
	K_I	K_{II}	K_I	K_{II}
(b)	0.11	0.84	0.13	1.36
(c)	0.66	0.2	0.21	-0.3
Total	0.77	1.04	0.34	1.06
(a)	1.19	1.06	0	1.03

b)

Without Contacts	Left end		Right end	
	K_I	K_{II}	K_I	K_{II}
(b)	0.112	0.837	0.134	1.363
(c)	3.357	0.325	3.541	-0.469
Total	3.469	1.162	3.675	0.894
(a)	3.459	1.162	3.404	0.896

Table 2.4: Effect of contact in stress intensity factor calculations: a) with contact b) without contact.

utilized in this work. Unfortunately, for other arbitrary loading conditions of interest, one has to make a separate model for computing the fracture strength of the connection.

2.6.5 Parametric Study

Detailed finite element analyses are performed for all combinations of the joint parameters H/h = [1, 2.5, 5], w/h = [0.2, 0.6, 1] and a/h = [0.25, 1, 2] and the stress intensity factors are evaluated for each of the 27 different joint configurations. Table 2.5 lists the normalized mode-I and mode-II stress intensity factors at the left and right notch for all three ratios of H/h corresponding to a positive applied moment. Similar results corresponding to a negative moment are shown in Table 2.6. Tables 2.5 and 2.6 also list the mode mixity angle, defined as $\tan^{-1}(K_{II}/K_I)$, for various joint configurations. Since the critical moment is a dependent parameter, it is normalized as

$$\bar{M}_c = \frac{M_c}{h^{3/2}.K_{Ic}}$$

When a positive or negative moment is applied at the free edge of the upper plate, one can visualize one side of the overlap opening and the other closing. Cracks that close completely gives $K_I = 0$ and are highlighted as gray boxes in the Tables 2.5 and 2.6. The negative stress intensity values in both the tables for a closing notch signify the reverse stresses of shear. For the M^- cases, there are fewer crack closings. By zooming in on the deformed model shown in Fig. 2.14, this behavior can be explained by the hinging effect of the overhang plate. The stresses which are usually carried by the welded length

Joint			Right or opening notch				Left or closing notch			
H/h	w/h	a/h	f_I	f_{II}	$\bar{M}_c$	Mode Mixity*	f_I	f_{II}	$\bar{M}_c$	Mode Mixity*
1	0.2	0.25	11.86	1.28	9038	0.107	0.00	-1.56	60521	
1	0.2	1	2.93	0.83	33620	0.275	0.75	-0.83	76460	0.840
1	0.2	2	1.78	0.83	48940	0.436	0.21	-0.83	101200	1.322
1	0.6	0.25	4.53	1.32	21620	0.282	0.00	-1.58	59600	
1	0.6	1	2.11	1.30	37080	0.551	0.00	-1.30	72600	
1	0.6	2	1.66	1.40	40560	0.701	0.00	-1.40	67530	
1	1	0.25	2.71	1.40	31040	0.477	0.00	-1.59	59560	
1	1	1	1.85	1.45	37780	0.666	0.07	-1.45	63540	1.523
1	1	2	1.63	1.45	40040	0.728	0.10	-1.45	62940	1.499
2.5	0.2	0.25	11.87	1.21	9047	0.101	0.00	-1.43	66200	
2.5	0.2	1	3.28	0.71	31170	0.212	0.65	-0.67	91770	0.801
2.5	0.2	2	2.43	0.75	39920	0.299	0.37	-0.72	103600	1.100
2.5	0.6	0.25	4.65	1.18	21579	0.248	0.02	-1.12	83343	1.553
2.5	0.6	1	2.57	1.15	34380	0.421	0.00	-0.95	99100	
2.5	0.6	2	2.30	1.19	36530	0.476	0.00	-1.02	92670	
2.5	1	0.25	2.95	1.26	30317	0.403	0.00	-0.88	107070	
2.5	1	1	2.27	1.33	35160	0.531	0.00	-0.93	101800	
2.5	1	2	2.18	1.36	35720	0.558	0.00	-0.99	95830	
5	0.2	0.25	11.85	1.21	9058	0.102	0.00	-1.43	65975	
5	0.2	1	3.31	0.69	31060	0.205	0.65	-0.65	93880	0.785
5	0.2	2	2.49	1.33	33310	0.492	0.30	-0.68	113100	1.154
5	0.6	0.25	4.65	1.17	21578	0.247	0.02	-1.10	84777	1.553
5	0.6	1	2.60	1.12	34350	0.405	0.00	-0.90	105100	
5	0.6	2	2.36	1.14	36400	0.451	0.00	-0.95	98930	
5	1	0.25	2.95	1.26	30355	0.402	0.00	-0.85	111580	
5	1	1	2.32	1.30	35170	0.510	0.00	-0.85	111400	
5	1	2	2.24	1.32	35670	0.531	0.00	-0.90	105400	

* Mode Mixity = $\tan^{-1}(K_{II}/K_I)$

Table 2.5: Stress intensity factors in 27 different joint configurations at the left and right crack tips for a positive moment load.

Joint			Left or opening tip				Right or closing tip			
H/h	w/h	a/h	f_I	f_{II}	$\bar{M}_c$	Mode Mixity*	f_I	f_{II}	$\bar{M}_c$	Mode Mixity*
1	0.2	0.25	11.84	1.28	9053.2	0.107	0	-1.56	60508	
1	0.2	1	2.93	0.83	33640	0.276	0.745	-0.831	76440	0.840
1	0.2	2	1.79	0.83	48830	0.435	0.216	-0.828	101000	1.316
1	0.6	0.25	4.54	1.32	33810	0.282	0	-1.583	59620	
1	0.6	1	2.13	1.30	36910	0.547	0	-1.298	72740	
1	0.6	2	1.65	1.40	40600	0.703	0	-1.397	67560	
1	1	0.25	2.71	1.40	31040	0.477	0	-1.587	59490	
1	1	1	1.85	1.45	37760	0.666	0.071	-1.45	63610	1.522
1	1	2	1.63	1.45	40020	0.727	0.034	-1.45	64300	1.547
2.5	0.2	0.25	11.89	1.14	9049	0.095	0	-1.485	63579	
2.5	0.2	1	2.52	0.29	42430	0.115	1.025	-0.339	93170	0.319
2.5	0.2	2	0.75	0.18	134500	0.235	1.005	-0.198	102800	0.195
2.5	0.6	0.25	4.35	0.80	23934	0.182	0	-1.413	66784	
2.5	0.6	1	1.28	0.39	75950	0.294	0.348	-0.586	123000	1.035
2.5	0.6	2	0.17	0.26	274000	0.983	0.841	-0.33	109000	0.374
2.5	1	0.25	2.22	0.62	44450	0.274	0	-1.41	66947	
2.5	1	1	0.75	0.39	111800	0.483	0.328	-0.736	104600	1.152
2.5	1	2	0.05	0.27	321200	1.376	0.841	-0.385	104200	0.429
5	0.2	0.25	11.88	1.14	9050.5	0.095	0.089	-1.475	62223	1.511
5	0.2	1	2.53	0.26	42460	0.104	1.026	-0.315	94540	0.298
5	0.2	2	0.72	0.11	147100	0.157	1.036	-0.135	102700	0.130
5	0.6	0.25	4.36	0.78	23918	0.177	0	-1.403	67279	
5	0.6	1	1.27	0.32	79140	0.246	0.349	-0.542	130400	0.999
5	0.6	2	0.09	0.13	530500	0.951	0.887	-0.219	113400	0.242
5	1	0.25	2.22	0.58	44861	0.256	0	-1.401	67378	
5	1	1	0.71	0.29	128500	0.386	0.329	-0.678	111600	1.119
5	1	2	0.07	0.10	700700	0.987	0.883	-0.239	112400	0.264

* Mode Mixity = $\tan^{-1}(K_{II}/K_I)$

Table 2.6: Stress intensity factors in 27 different joint configurations at the left and right crack tips for a negative moment load.

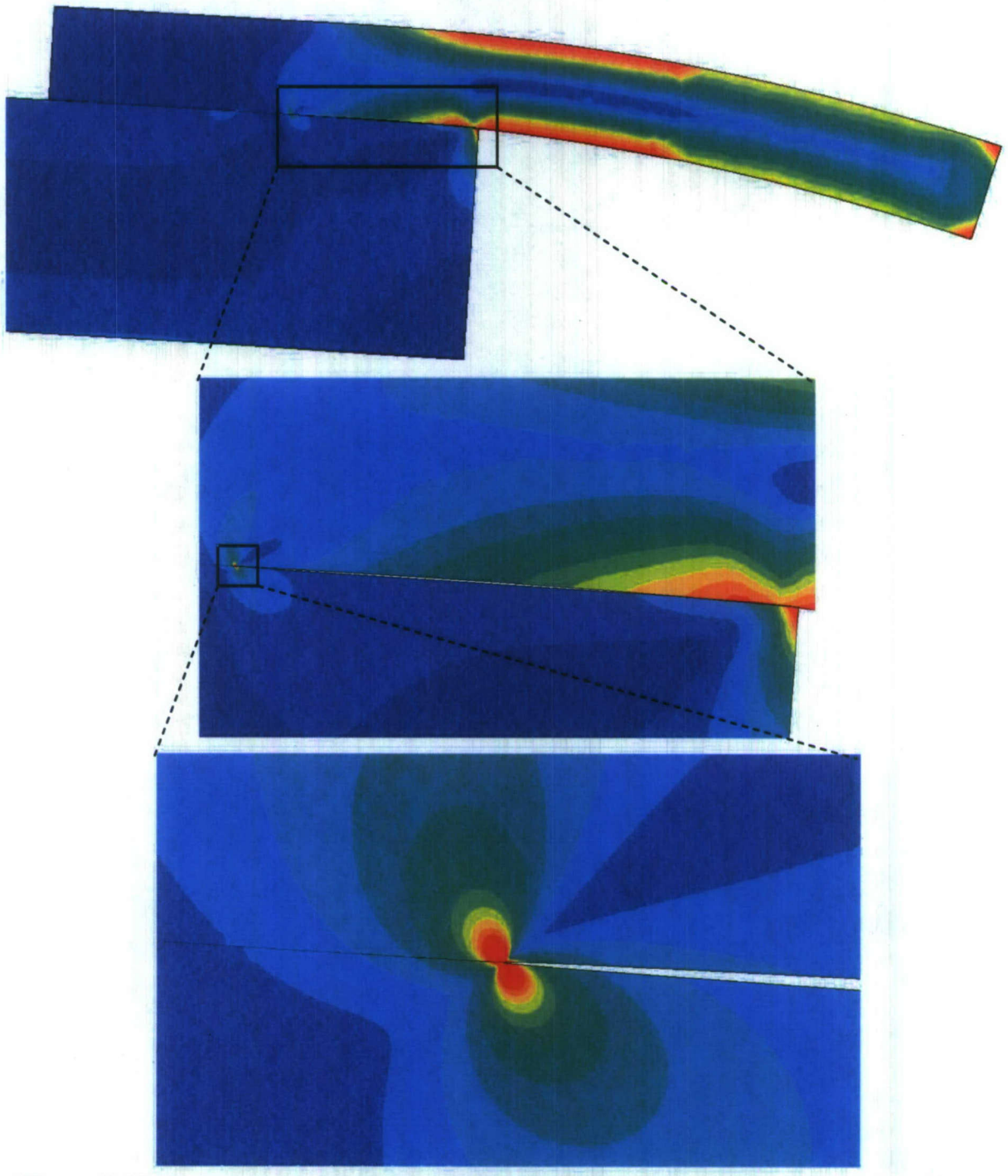

Figure 2.14: Contour plot of joint configuration (H/h = 2.5, w/h = 0.6, a/h = 2) with M^- loading illustrating hinging effect.

become concentrated at the hinge point. This leads to a visually unaffected left notch and a rather high tensile stress concentration at the right notch. The green boxes show that some of these configurations have closing notch critical moment lower than the one at opening notch. This shows that these configurations are more susceptible to crack propagation at the closing overlap side rather than the opening side of the joint. This is not much of a concern, though, because it will be shown in Chapter 3 that while cracks do propagate on the closing side they require much more steps to reach failure, than what is usually required at the opening side.

2.7 Metamodel Construction and Optimization

In order to optimize a laser welded lap joint, the fracture strength has to be evaluated using the finite element method for a large number of candidate designs. The computational cost of performing hundreds of detailed finite element analyses can be prohibitive. One way to overcome this problem is to generate an approximation to the finite element values at a much lower cost. Such approximations are often called metamodels in that they provide a "model of the model".

Based on the results of a limited number of finite element analyses, simple curve fits were initially tried using the mathematical software MATLAB to obtain the stress intensity factors for arbitrary joint configurations. An exponential curve fit was tested over the data obtained from parametric study and the least square errors were minimized using a single-objective genetic algorithm. The method did not provide satisfactory results due to the high nonlinearity of the data. This prompted the investigation, and the ultimate use, of metamodels.

Taking a simple mathematical approach to metamodels, let the vector $\boldsymbol{x}$ denote the decision variables and $y = f(\boldsymbol{x})$ denote the true output obtained from a finite element analysis of the joint at those decision variables. The corresponding computationally efficient metamodel approximation is denoted by $\hat{y} = g(\boldsymbol{x})$. The closeness of the two results $f(\boldsymbol{x})$ and $g(\boldsymbol{x})$ shows the accuracy of a metamodel. There are several techniques for approximating the function $f(\boldsymbol{x})$ by $g(\boldsymbol{x})$ such as response surface methodology (RSM), kriging, support vector regression, neural networks and radial basis functions (RBF) (Jin et al., 2001; Fang et al., 2005).

During the method selection process two popular methods, RSM and RBF, were compared. RSM is very simple and efficient, but is not suitable for creating global models over the entire design space for highly non-linear problems. In a work by Yang et al. (2002) it is suggested that RSM can be ineffective in multi-objective optimization problems because the response region of interest would never reduce to a small area that is good for all conflicting objectives. Jin et al. (2001) compared several metamodels using fourteen different problems. Among those, the RBF method was found to be the best for both large and small scale problems. In addition, the method was also found to be best for overall performance with respect to accuracy, robustness, problem type flexibility, sample size, efficiency and simplicity. Krishnamurthy (2003) compared other metamodels with an augmented RBF and found it to be very promising and efficient. RBFs, on the other hand, are computationally more expensive because it uses a series of complex functions for a single model. This becomes apparent when solving a multi-objective optimization problem where a set of trade-off solutions needs to be obtained.

The RBF procedure uses a linear combination of basis functions centered at each sampling point. This can be represented as

$$g(\mathbf{x}) = \sum_{i=1}^{n} \lambda_i \phi(\|\mathbf{x} - \mathbf{x}_i\|), \tag{20}$$

where n is the number of sampling points, $\boldsymbol{x}$ is the vector of design variables (H/h, w/h and a/h for the problem here), $\boldsymbol{x}_i$ is the vector of design variables at the i^{th} sampling point, ϕ is the basis function and λ_i are the unknown weighting coefficients. Some of the most commonly used basis functions are the thin plate spline, Gaussian, multiquadric, inverse multiquadric and logistic basis functions. The data generated in the parametric study was found to be best suited for use with the multiquadric basis function which is defined as

$$\phi(r) = \sqrt{r^2 + 1}. \tag{21}$$

An augmented radial basis function method is utilized to construct the required metamodel. The RBF defined in equation (20) did not provide a satisfactory model when applied to the sampling data and thus it was augmented using exponential functions to better approximate the global response of the true function. The augmented RBF model is expressed in the form

$$g(\mathbf{x}) = \sum_{i=1}^{n} \lambda_i \phi(\|\mathbf{x} - \mathbf{x}_i\|) + \sum_{j=1}^{m} c_j p_j(\mathbf{x}), \tag{22}$$

where p_j are the global approximation functions, c_j are the corresponding unknown weight coefficients and m is the number of linearly independent global approximation

functions used to represent the global response. The chosen global approximation functions is

$$p = [1, e^{-\alpha_1 x_1}, e^{-\alpha_2 x_2}, e^{-\alpha_3 x_3}, e^{-\alpha_1 x_1 - \alpha_2 x_2}, e^{-\alpha_2 x_2 - \alpha_3 x_3}, e^{-\alpha_3 x_3 - \alpha_1 x_1}, e^{-\alpha_1 x_1 - \alpha_2 x_2 - \alpha_3 x_3}]^T.$$

where x_i represent the variables *H/h*, *w/h* and *a/h* for i = 1, 2 and 3 respectively and α_i are corresponding coefficients which are optimized so as to provide as best fit to the data as possible. In general, the stress intensity factors obtained from the finite element analyses were found to be smoothly increasing or decreasing monotonic functions of the design variables. Therefore, the global response of RBF is appended using exponentially increasing or decreasing functions. By combining an appropriate global model and the RBF methodology, a quality approximation is created which possesses the desirable trait of returning the true function values at the sampling points. As for the undetermined coefficients, the exponents α_i and the weight coefficients c_j of the global approximation functions are obtained by the method of least squares. The sum of the square of the errors at the sampling points is minimized using a real-coded single-objective genetic algorithm. These three sets of α and c coefficients will be different depending on the type of load, the location of the notch and the fracture mode. These coefficients will be different if only a two-dimensional curve fit is desired (with one design variable held fixed) instead of the full three-dimensional model. While it may be a concern for other methods, there is no need to impose any orthogonality condition to obtain c coefficients. Once the α and c coefficients are obtained from the GA, the only unknown variables to be determined are

the weighting coefficients λ which are determined by solving the linear system of equations (Krishnamurthi, 2003)

$$A\lambda + Pc = g, \tag{23}$$

where $A_{i,j} = \phi(||\boldsymbol{x}_i - \boldsymbol{x}_j||)$, $P_{i,j} = p_j(x_i)$ $(i = 1,2,\ldots n, j = 1,2,\ldots m)$, $\boldsymbol{\lambda} = [\lambda_1, \lambda_2,\ldots, \lambda_n]^T$, $\boldsymbol{c} = [c_1, c_2,\ldots, c_m]^T$ and $\boldsymbol{g} = [g(\boldsymbol{x}_1), g(\boldsymbol{x}_2),\ldots, g(\boldsymbol{x}_n)]^T$. As previously alluded to, it should be reiterated that the augmented RBF approximation passes through all the sampling points exactly. In other words, the output of the metamodel is identical to the true function value at the sampling points unlike a least squares approximation.

The outlined method is used to construct a metamodel for the stress intensity factor values obtained for positive and negative moment loading cases. Using the data of twenty seven sampling points for each separate load case, the genetic algorithm is utilized to obtain the α and c coefficients. For full three-dimensional (all three design variables) validations, four sets of three α coefficients and eight c values are evaluated for each load type. One such three-dimensional set of coefficients for the M^+ load case with stress intensity factors at the right notch for both mode-I and II is given in Table 2.7. If one of the variables is held constant and a two-dimensional fit is desired for further validation, twelve sets of three α coefficients and four c values are obtained for each load type. One of these sets for a use in a two-dimensional evaluation for representing the stress intensities for both fracture modes at the left notch under M^- load is given in Table 2.8.

No.	c		α	
	Mode-I	Mode-II	Mode-I	Mode-II
1	2.2166	1.32611	4.15975	5.21889
2	-34.2	35.3324	3.40316	3.10918
3	0.2898	-0.8773	2.96254	9.48687
4	0.1049	-1.1726		
5	-6.358	-68.995		
6	42.615	-10.06		
7	39.03	9.28647		
8	77.755	200		

Table 2.7: GA optimized c and α coefficients for right notch stress intensity factors for a full 3D validation case under M^+ load.

H/h	mode		1	2	3	4
1	I	c	1.686	0.028	0.774	38.882
		α	-	3.423	2.794	
	II	c	1.464	-1.555	-0.486	7.049
		α	-	4.452	6.715	
2.5	I	c	0.156	0.498	2.143	33.018
		α	-	3.1294	2.192	
	II	c	0.3519	-0.297	0.235	2.220
		α	-	1.8538	2.311	
5	I	c	0.1268	0.4276	2.055	32.571
		α	-	3.0642	2.154	
	II	c	0.183	-0.182	0.261	1.981
		α	-	1.4501	1.897	

Table 2.8: GA optimized c and α coefficients for left notch stress intensity factors for a full 2D validation case under M^- load.

2.8 Validation

As stated earlier, the augmented RBF passes through all sampling points exactly and thus the only concern with the RBF is whether or not the model is accurate at locations away from the sampling points. Therefore, the accuracy of the metamodel needs to be checked at points which do not coincide with the sampling points. Different validation designs are constructed for both two and three-dimensional curve fits. In a two-dimensional plot, function values are evaluated by fixing one of the three dimensionless ratios *H/h, w/h* and *a/h* and changing the other two, while in a three-dimension validation, all three ratios are varied. Ten finite element analyses are performed for each load type and for both the two and three-dimensional cases to obtain the stress intensity factors for use in validating the metamodel. These results are labeled as validation points. To aid in the validation process, two and three-dimensional plots are presented separately for two different loading conditions which allow one to visualize the error in the metamodel.

2.8.1 Two-dimensional Validation

For comparisons concerning the effects of load type, the metamodel input file can be changed from M^- left (or opening) tip results to M^+ right (or opening) tip results. However, the M^+ right tip plots will come out to be very similar to the plots for the M^- left tip because, if we look at Tables 2.5 and 2.6 for an *H/h* ratio of 1, it is noticed that there are negligible changes in the stress intensity values. Therefore, instead of separating the results based solely on load type, the two-dimensional results have been further divided into left and right notch plots. For two-dimensional cases shown here, only the

left notch will be studied for two types of loads while in the next section for the three-dimensional cases, the right notch will be discussed for both load types.

Two dimensional surface plots of the normalized stress intensity factors $f_I^{M-,l}$ and $f_{II}^{M-,l}$ obtained from the metamodel are shown in Figs. 2.15 (a) and (b). The thickness ratio H/h is chosen to be equal to 1 and the normalized stress intensities for M^- at the left notch are plotted as a function of a/h and w/h. The plot shows an infinite number of designs among which ten are chosen to be validated using actual finite element results. The visible green asterisks are sampling points while the yellow asterisks are validation points. The dark red portion of the surface denotes maximal values of the function. It would be interesting to observe the differences in the surface plot if the load is reversed (i.e. M^+) whilst keeping other factors constant (H/h = 1, left notch). The plot corresponding to this case is shown in Figs. 2.15(c) and (d) for mode-I and II respectively. Looking at the mode-I plot for M^-, it can be seen that the maximum stress intensities are obtained when the joint overlap is at a minimum. For the M^+ case, it is noted that maximum stress intensities occur for designs with the small and mid-length non-welded and welded regions respectively. With these observations established, consideration is given to the other design variable. The large errors in the mode-I, M^+, left tip plot are due to the fact that the actual value at these locations is zero whilst the model predicts a small, but finite value. More sample analyses are required to better capture the closing phenomenon which leads to this behavior.

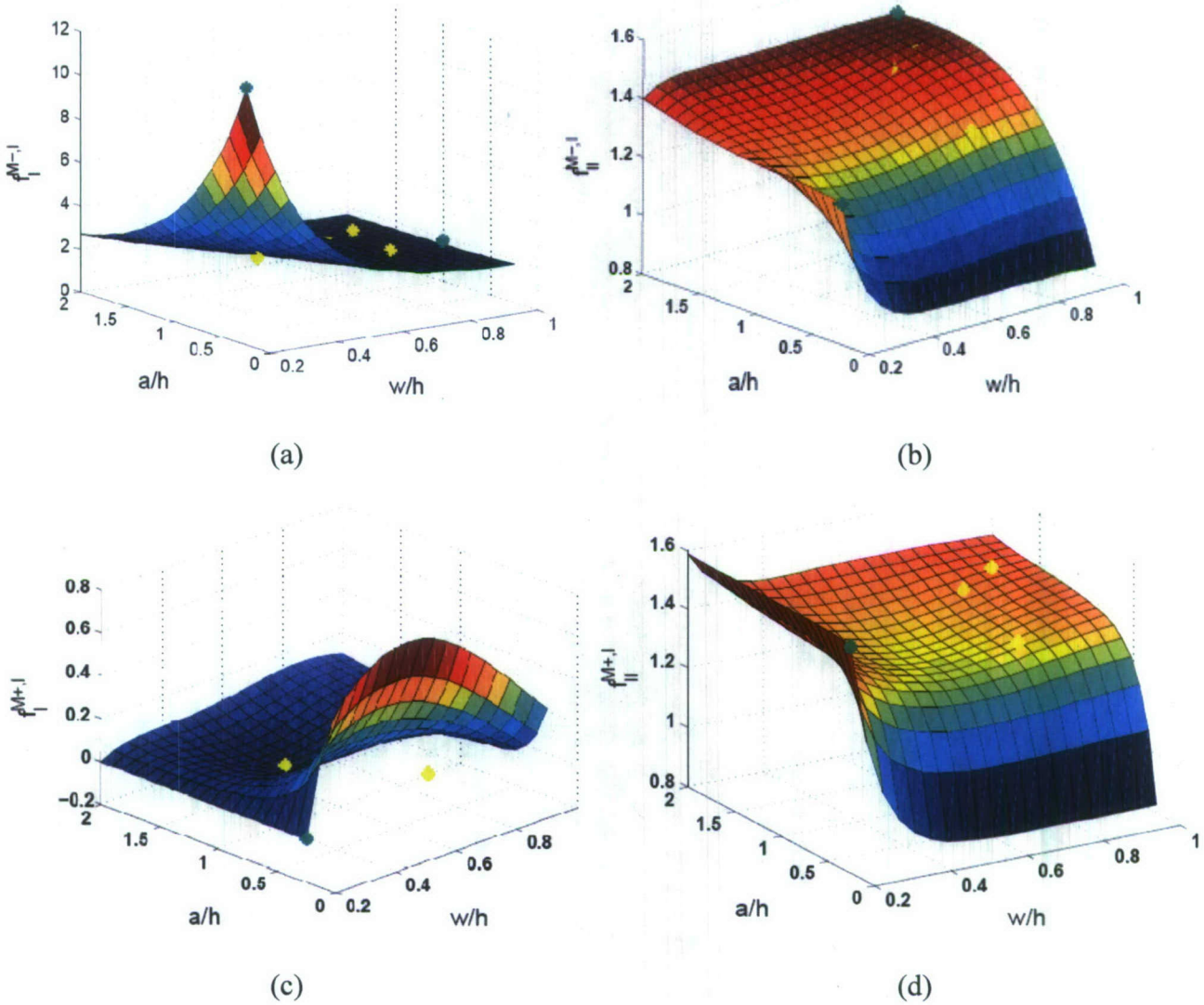

Figure 2.15: Two-dimensional surface plots of geometric configuration factor values at the left notch for *H/h*=1: (a) mode-I and (b) mode-II under M^-, (c) mode-I and (d) mode-II under M^+.

The surface curvature clearly illustrates the nonlinearity in the data and reinforces the importance of using the metamodeling approach. The percentage errors between the detailed finite element analysis results at the left notch and the corresponding metamodel predictions for H/h=1 and both loading types are given in Tables 2.9(a) and (b). It is observed that the metamodel is fairly accurate and that the error is on the order of one or two percent. At some locations higher errors can be observed, the reason for which will be addressed later. Mode-I error is not shown in Table 2.9(b) because even though the value provided is not poor in a practical sense, the error is technically infinite.

2.8.2 Three-dimensional Validation

Here a three-dimensional model is used for explaining the workings of the metamodel. In a three-dimensional metamodel, one can obtain values of stress intensity factors for a large combination of the three dimensionless ratios. The M^+ right notch case is considered here to explain the metamodeling process. In this case, the function value $f_I^{M+,r}$ (or $f_{II}^{M+,r}$) is evaluated to create m x n x p volume array of data for plotting. Slice volumetric plots for M^+ mode-I and II are shown in Figs. 2.16(a) and (b) where darker red portions represents a higher geometric configuration factor value, and conversely, darker blue regions indicate a lower factor value. For the purposes of this discussion, recall that for the joint geometry, a/h and w/h combined represent the overlapped area, while H/h represents the lower plate thickness. As apparent from Fig 2.16(a), the smaller the total overlap area the greater the tensile stress concentration. This effectively reduces

(a)

Test Configurations			Mode-I			Mode-II		
H/h	w/h	a/h	$f_I^{M-,l}$	$*f_I^{M-,l}$	%Error	$f_{II}^{M-,l}$	$*f_{II}^{M-,l}$	%Error
1	0.5	1.2	1.999	2.030	-1.551	1.222	1.262	-3.241
1	0.7	0.5	2.844	2.781	2.233	1.349	1.340	0.667
1	0.8	1.5	1.744	1.750	-0.367	1.398	1.423	-1.788
1	0.9	1.6	1.698	1.700	-0.118	1.428	1.447	-1.310

(b)

Test Configurations			Mode-I		Mode-II		
H/h	w/h	a/h	$f_I^{M+,l}$	$*f_I^{M+,l}$	$f_{II}^{M+,l}$	$*f_{II}^{M+,l}$	%Error
1	0.5	1.2	0	0.0638	1.224	1.295	5.83
1	0.7	0.5	0	0.0284	1.407	1.407	0.00
1	0.8	1.5	0	0.0571	1.398	1.381	1.22
1	0.9	1.6	0	0.0995	1.43	1.421	0.44

* Metamodel results

Table 2.9: Two-dimensional validation results checked at the left notch for H/h=1 for: M^- and (b) M^+ load.

(a)

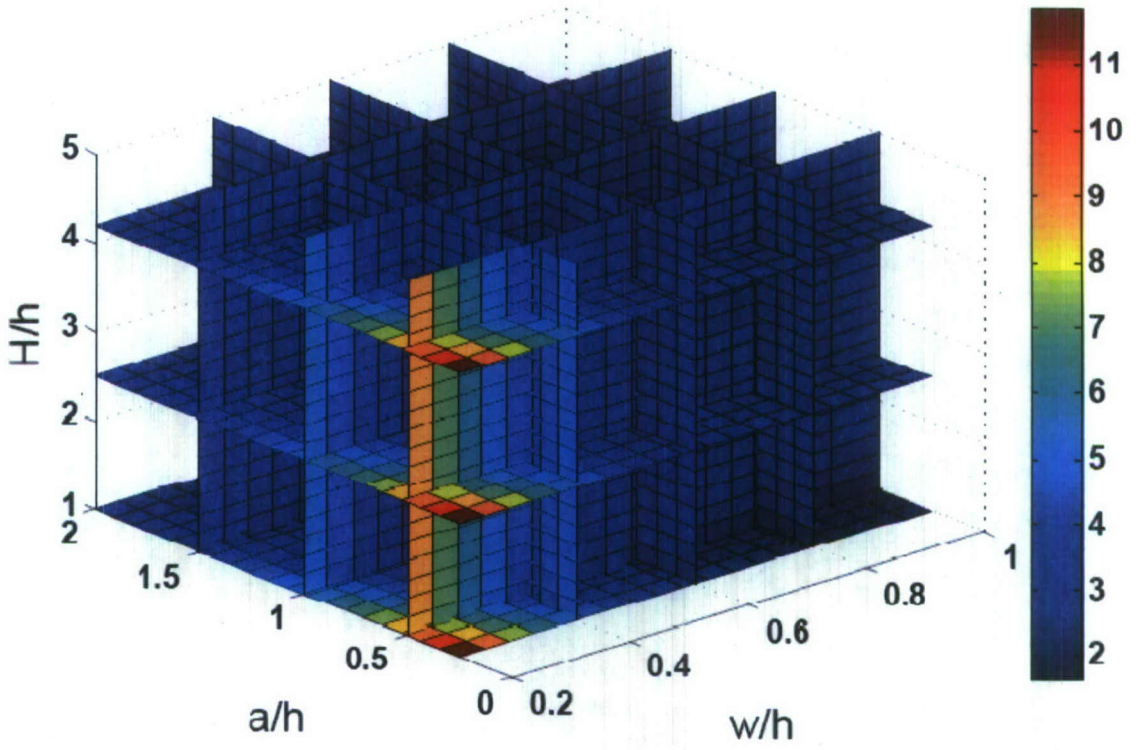

(b)

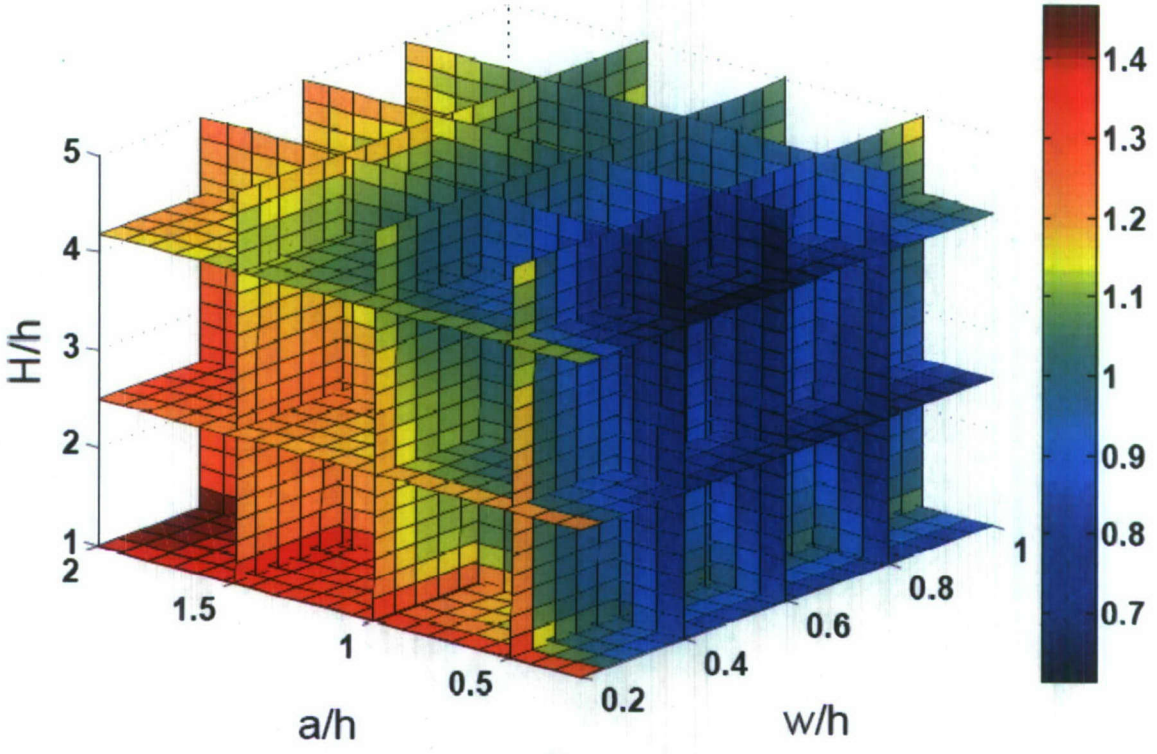

Figure 2.16: Three-dimensional volumetric slice plot for M^+, right notch tip: (a)mode-I, (b)mode-II.

the strength of the joint, which conceptually makes sense. For mode-II, the plot shows that stress intensities are higher for geometries with high non-welded lengths, which represents the contact area between the left surfaces. As this contact area increases, the shear stress increases. If the figure is rotated and one inspects the slices on the vertical axis, it is observed that the shear stress distribution is highest when the lower plate thickness is at a minimum. This is because large lower plate thicknesses possess a high stiffness which reduces the shear stress concentration.

Table 2.10 gives the percentage errors between the finite element analyses for ten different joint configurations and the corresponding metamodel results for the M^+ right notch case. It is seen that the errors are within seven percent for all validation points, which for such a small number of sampling points, is acceptable.

As seen in Table 2.6, there are some joint configurations which show low failure strength on the closing side of the overlap. This ascertains the requirement of forming a metamodel for the closing side also. Data has been extracted from the same twenty seven analyses and ten validation points to construct data for the closing notch. There are two load types under consideration. For M^+, the left edge of the weld is the closing notch while for M^-, the right notch will close. Tables 2.11 (a) and (b) present the data for a two-dimensional metamodel validation for the left notch with M^+ and for a three-dimensional validation of the right notch with M^-, respectively. The errors have not been shown due to the often indeterminate nature of the error for mode-I. However, it can be seen that due to the very low values of the geometric configuration factors, any slight

Test Configurations			Mode-I			Mode-II		
H/h	w/h	a/h	$f_I^{M+,r}$	* $f_I^{M+,r}$	%Error	$f_{II}^{M+,r}$	* $f_{II}^{M+,r}$	%Error
1.2	0.5	1.2	2.20	2.3261	-5.612	1.20	1.1625	2.801
1.5	0.7	0.5	3.09	3.0281	2.003	1.23	1.1855	3.303
1.8	0.8	1.5	2.19	2.27	-3.700	1.33	1.2614	5.015
2	0.9	1.6	2.18	2.2326	-2.554	1.35	1.2951	4.350
2	0.4	0.4	5.14	5.3332	-3.739	0.99	1.0628	-6.922
2.2	0.5	1.1	2.57	2.5863	-0.713	1.10	1.0802	1.442
2.4	0.9	0.6	2.61	2.5462	2.283	1.26	1.2815	-1.787
3	0.7	0.5	3.16	3.0602	3.112	1.15	1.1726	-2.321
3.5	0.4	0.5	4.42	4.5666	-3.429	0.94	0.9675	-2.926
4.2	0.8	0.6	2.77	2.6664	3.723	1.19	1.1219	6.039

* Metamodel results

Table 2.10: Comparison of Metamodel with finite element results with Ten three-dimensional validation designs for the M^+ right notch case for both mode-I and II.

change, even in the second decimal place, makes a big difference in percentage error. In some analysis types for both the two and three-dimensional spaces, comparisons of the validation points with the metamodel values give high errors. These results have been checked for different basis functions of the metamodel as well, and it has been found that multiquadric works the best. Therefore, the above stated errors could potentially be due to changes in the mesh partition size used for each of the validation designs. As has been previously discussed, changes in the partition size have a significant impact on the obtained results. Another potential, and probable, cause could be the small number of sampling points used in constructing the metamodel. With the nonlinearity present in the data, more sampling points would definitely improve the results albeit at the cost of a greatly increased workload in terms of analysis runs and post-processing.

Although they are a little tedious to construct and give moderate errors for some configurations, metamodels provide a means of closely approximating the stress intensity factors for arbitrary joint configurations in a fraction of the time that it takes to perform a detailed finite element analysis.

(a)

Test Configurations			Mode-I		Mode-II	
H/h	w/h	a/h	$f_I^{M+,r}$	$*f_I^{M+,r}$	$f_{II}^{M+,r}$	$*f_{II}^{M+,r}$
1	0.5	1.2	0	0.0638	1.224	1.295
1	0.7	0.5	0	0.0284	1.407	1.407
1	0.8	1.5	0	0.0571	1.398	1.381
1	0.9	1.6	0	0.0995	1.43	1.421
2.5	0.4	0.4	0	0.0738	0.935	1.049
2.5	0.5	1.1	0	0.0389	0.937	0.924
2.5	0.9	0.6	0	-0.0052	0.876	0.964
2.5	0.7	0.5	0	0.0073	0.894	1.048
5	0.4	0.5	0	0.1256	0.837	0.898
5	0.8	0.6	0	-0.01	0.837	0.928

(b)

Test Configurations			Mode-I		Mode-II	
H/h	w/h	a/h	$f_I^{M+,r}$	$*f_I^{M+,r}$	$f_{II}^{M+,r}$	$*f_{II}^{M+,r}$
1.2	0.5	1.2	0.23	0.3034	0.94	1.012
1.5	0.7	0.5	0	0.1807	1.114	1.212
1.8	0.8	1.5	0.56	0.6064	0.643	0.733
2	0.9	1.6	0.64	0.6701	0.58	0.634
2	0.4	0.4	0	0.1377	1.027	1.167
2.2	0.5	1.1	0.454	0.4961	0.525	0.537
2.4	0.9	0.6	0	0.2042	0.996	0.951
3	0.7	0.5	0	0.1846	1.003	0.983
3.5	0.4	0.5	0	0.2345	0.846	0.957
4.2	0.8	0.6	0	0.2947	0.932	0.896

* Metamodel results

Table 2.11: Metamodel validation results checked at ten joint configurations for: (a) 2D M^+ cases at left/closing notch for both mode-I and II, and (b) 3D M^- cases at right/closing notch for both mode-I and II.

2.9 Results and Discussion

In this section, optimal design studies are performed on two model problems and the results are presented. These design studies will demonstrate the procedure of using the established model. The joint geometry is similar to the lap joint shown in Fig 2.1. For both studies, the insert and sub-frame are assumed to be made of HSLA-65 steel. The yield strength and critical stress intensity factors are taken to be S_y = 65 Ksi and K_{Ic} = 113.76 ksi$\sqrt{in}$. Both of these model problems utilize previously constructed metamodels.

2.9.1 Design Problem I: Optimal Weld-Width with a Positive Moment

We consider the design of a laser welded joint that is subjected to a positive moment of M_{design} = *750* lb-in/in. The stress in the insert material is obtained from beam bending theory:

$$\frac{\sigma_b}{y} = \frac{M}{I} \Rightarrow \sigma_b = \frac{6M}{h^2}. \tag{24}$$

The factor of safety against yielding S_y/σ_b is chosen to be 2. Obtaining σ_b from this yield factor of safety expression and plugging the result into equation (24) gives the thickness of the insert material. Rounding the obtained thickness to the next standard dimension results in a value of h = 3/8″. Assuming a sub-frame thickness of H = 1″, the ratio of the insert thickness to the sub-frame thickness is H/h = 2.67. The metamodel for the right notch positive moment case is employed to compute the geometric configuration factors $f_i^{M+,r}(2.67, \frac{w}{h}, \frac{a}{h})$ for mode-I and II. If the ratio a/h is fixed at 2, a range of values varying with only w/h could be obtained. The stress intensity factors $K_I^{M+,r}$ and $K_{II}^{M+,r}$ at the right notch are evaluated using equation (18) where M is replaced by M_{design}. The crack initiation angle θ_o is computed by inserting the obtained K_I and K_{II} values in

equation (6). With θ_o, K_I and K_{II}, the critical fracture moment M_{fract} is obtained using the maximum tensile stress criteria for mixed mode failure via equation (8). Once the critical moment for the model is obtained, the factor of safety against fracture can be defined as $N_{fr} = M_{fract}/M_{design}$. Fig. 2.17 shows the fracture safety factor as a function of the weld-width ratio *w/h* for several different choices of *a/h*. It is noticed that the factor of safety is greater than 2 for the range of joint dimensions considered in this study. When the width of the non-welded region $a/h <= 1.0$, the factor of safety increases as the width of the non-welded region *w* increases. The trend reverses for values of $a/h > 1.0$. For a given weld-width *w*, it is found that a significant increase in the fracture safety factor can be achieved for an *a/h* value of approximately 1.5. If *a/h* is larger than 1.5, the weight of the joint would increase whereas the strength would remain virtually unchanged or decrease slightly. This drop in the strength value can be explained by the mode mixity factor, shown in Figure 2.18. If mode mixity is plotted versus *w/h*, it can be seen that its value increases for every increment in the *a/h* ratio. From this one can infer that the mode-II factor plays a more significant role in failure for higher overlaps. As the overlap continues to increase after a certain value of *a/h*, more shear stresses develop which lead to lowering the joint strength and fastening the failure of the joint.

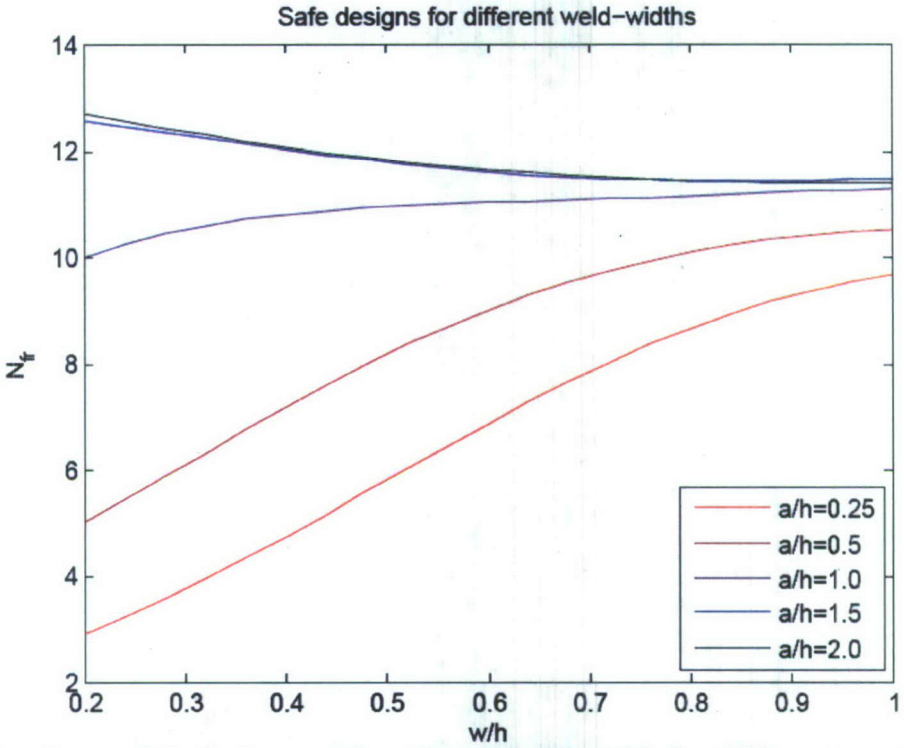

Figure 2.17: Fracture safety factor as a function of weld-width for different overlaps with M^+, right tip function evaluations.

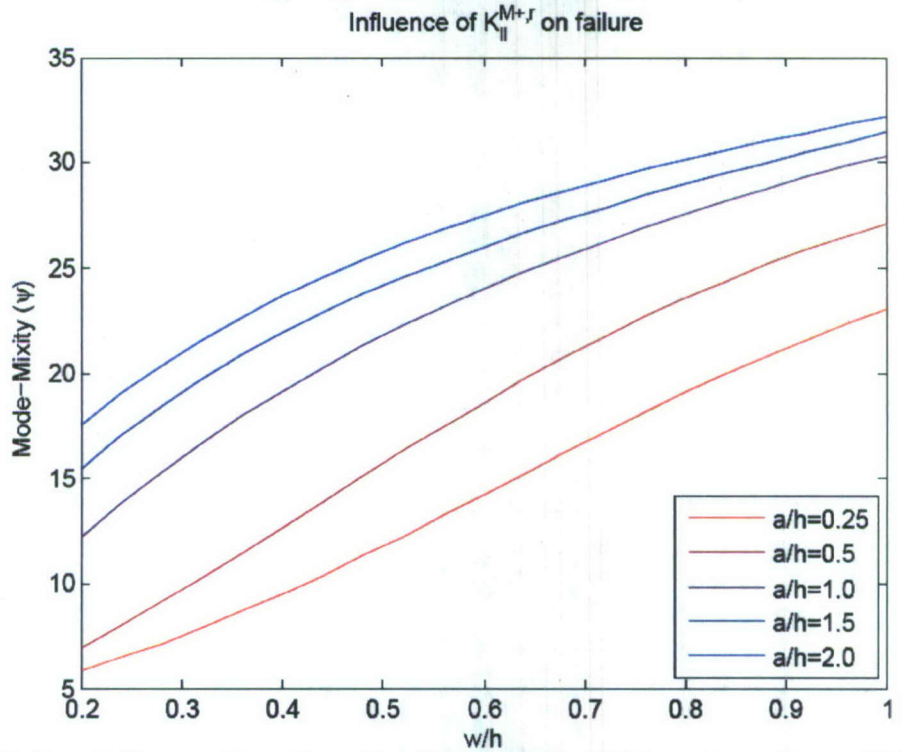

Figure 2.18: Mode mixity as a function of weld-width for different overlaps with M^+, right tip function evaluations.

Using these results, the optimum joint dimensions for this design case study are h = 0.375 in, $w = (0.2 \times h) = 0.075$ in and $a = (1.5 \times h) = 0.5625$ in. This model problem demonstrates the benefit of performing a limited number of detailed finite element simulations to aid in the construction of a metamodel that can then be later used to optimize laser welded lap joints.

2.9.2 Design Problem II: Optimal Weld-Width with a Negative Moment

As was discussed earlier, there are some non-zero mode-I stress intensity factors at the closing side of the joint, most notably in the negative moment cases. Therefore, for this design problem, a negative moment is applied and the critical load of failure at the left and right notches of the joint are analyzed and compared. The joint dimensions are identical to those used in design problem 1. The applied moment for this case is M_{design} = *-750* lb-in/in. As in the previous design study, keeping the yield factor of safety at 2 gives a thickness of h = 3/8″ and an H/h value of 2.67.

As described in the previous design problem, the metamodel is utilized to compute the factor of safety against fracture $N_{fr} = M_{fract}/M_{design}$ for both the left and right notches when the joint is subjected to a negative moment. These two values are compared and the minimum is selected as the final value for the fracture factor of safety. To get a better handle on the problem, the range of a/h is subdivided into very small segments and a three-dimensional surface plot is shown in Figs. 2.19(a) and (b).

From these plots it can be observed that at a minimum weld-width of w/h = 0.2 the factor of safety increases as the overlap increase up to a value of a/h = 1.5, beyond which the value remains relatively unchanged. Once the weld length increases to *0.3h*, a slow increase in N_{fr} is seen even beyond a/h = 1.5. Once the curve peaks, the value of N_{fr}

begins to diminish with increasing weld-widths. A very prominent feature of these plots is the line of peak value. This peak line remains almost unchanged for an entire series of configurations, which is rather interesting. These values possess total overlap ratios ($a/h + w/h$) in the range of 1.8 to 2.1. However, the maximum strength is seen away from this line at design values of $w/h = 0.3$ and $a/h = 2.0$.

Although there are a range of designs to choose from, if the errors discussed in evaluating the stress intensity factors in Section 2.9 are taken into consideration, and if one wants to check the design with maximum possible factor of safety, one would be better off with an a/h ratio of 1.65 and w/h value of 0.3. Thus, the optimum joint dimensions for this design case study are taken as $h = 0.375$ in, $w = (0.3 \times h) = 0.1125$ in and $a = (1.65 \times h) = 0.6187$ in. The factor of safety corresponding to this joint is $N_{fr} = 39.29$. With this design study we saw that, even for a complicated loading condition on a lap joint, metamodels prove to be a very useful and computationally inexpensive tool for designing optimal lap joint configurations.

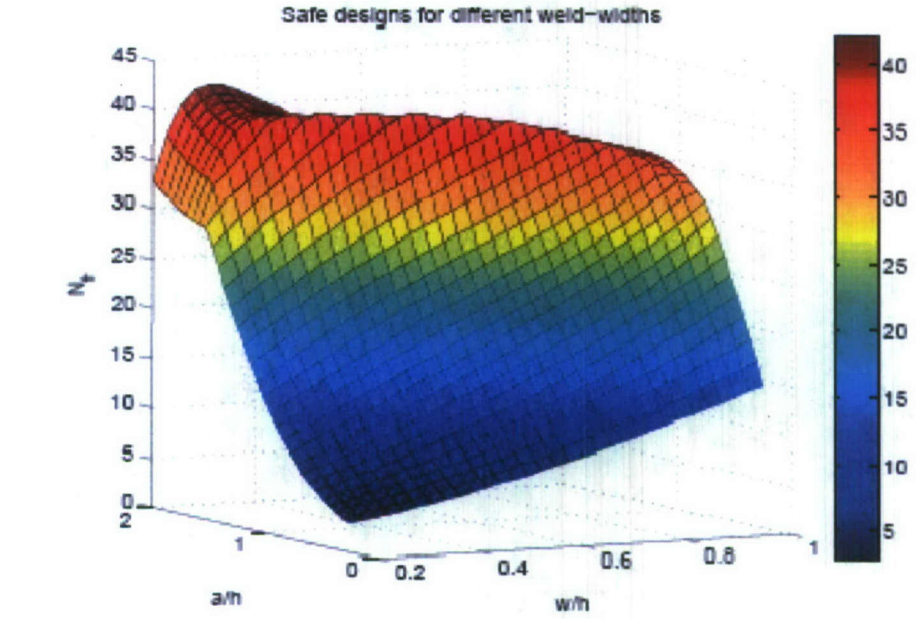

(a)

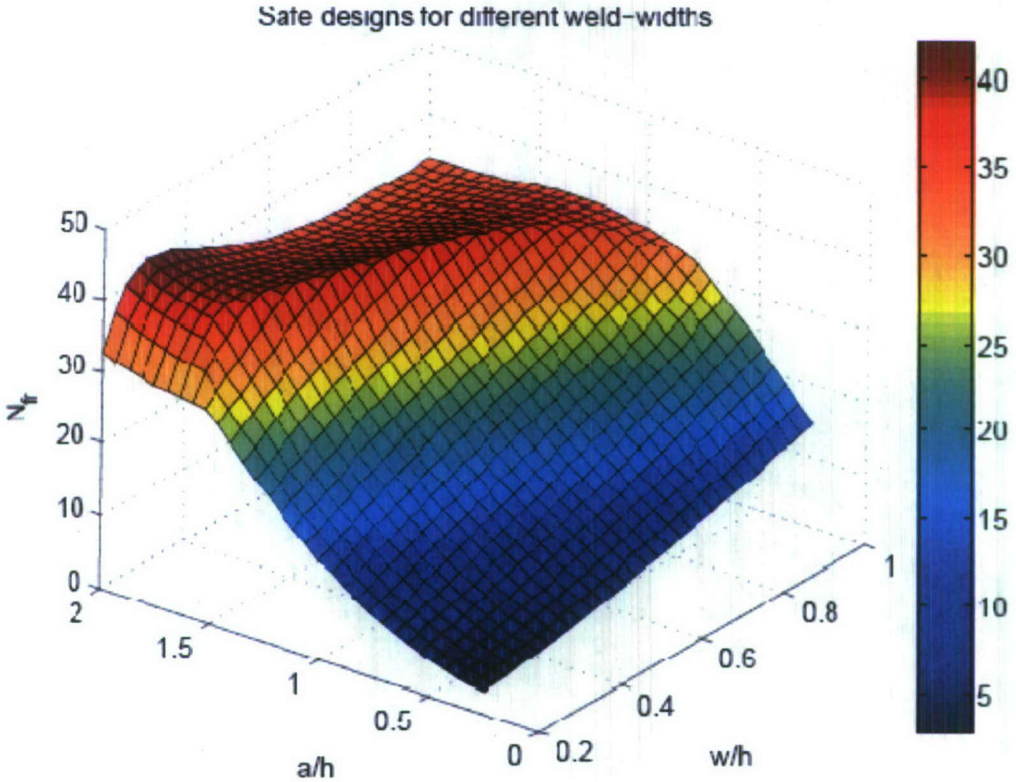

(b)

Figure 2.19: Two-dimensional surface plots of minimum fracture factor of safety at *H/h*=2.67 compared between the left and right notch for M^- cases.

3. FATIGUE CRACK PROPAGATION

3.1 Introduction

In this section, the two-dimensional crack propagation simulation software FRANC2D is used to study crack growth in laser welded lap joints. Sequential crack propagation analysis is performed to obtain the crack trajectories and corresponding stress intensity factors for lap joint configurations under three different loads; positive moment, negative moment and axial tension. The results of these analyses for each load case are utilized in conjunction with the Paris law to obtain a fatigue response estimate of the joints. Two joint configurations are selected to be studied under each load case among which one joint is set to be common to all the load cases.

3.2 Modeling in FRANC2D

Since the FEA program ABAQUS v6.6 does not provide a means for modeling crack propagation, a fracture-specific software is selected for use in this chapter. FRANC2D (FRacture ANalysis Code for 2D geometries) is a two-dimensional finite element based program for simulating curvilinear crack propagation in plane stress, plane strain and axisymmetric structures. The software was developed by Professor Ingraffea and his graduate students at Cornell University. FRANC2D requires an initial mesh of the geometry which has to be constructed separately since it does not feature a mesh generation module. Although it can be used with input files made in several different finite element software packages, the recommended pre-processing software CASCA is used to define the joint geometries and generate the initial mesh for all studies conducted in this chapter. Translation codes are also available on the Cornell Fracture Group website to convert other commercial finite element pre-processed data into a format that

is suitable for FRANC2D input. Several different mesh partition strategies were examined, as will be discussed in Section 3.3.1, and the selected mesh strategy for one such joint configuration is shown in Fig. 3.1.

3.2.1 Preprocessing

To begin the process, a FE model is created without cracks using the external mesh generator CASCA, as shown in Fig. 3.1(b). After loading the CASCA generated file, the remaining pre-processing is performed within FRANC2D. Similar boundary conditions are defined in FRANC2D as were in ABAQUS models. To simulate the boundary conditions in FRANC2D, translational degrees of freedom in x and y directions at the left edge of the lower plate are set to be equal to zero. Point and edge loads have been applied at the free edge of the upper plate to create the required couple and tensile forces, respectively. The next step is to define the material property of the joint. The entire model is defined to be made of any type of steel with a Young's Modulus of E = $29.7 \text{x} 10^3$ ksi and a Poisson's ratio of $\nu = 0.29$. In FRANC2D, contact modeling requires the use of gap elements and thus a second material property set for gap elements is required. The gap element property definition lets the user specify the surface friction and the interpenetration allowed between the surfaces in contact. These elements are

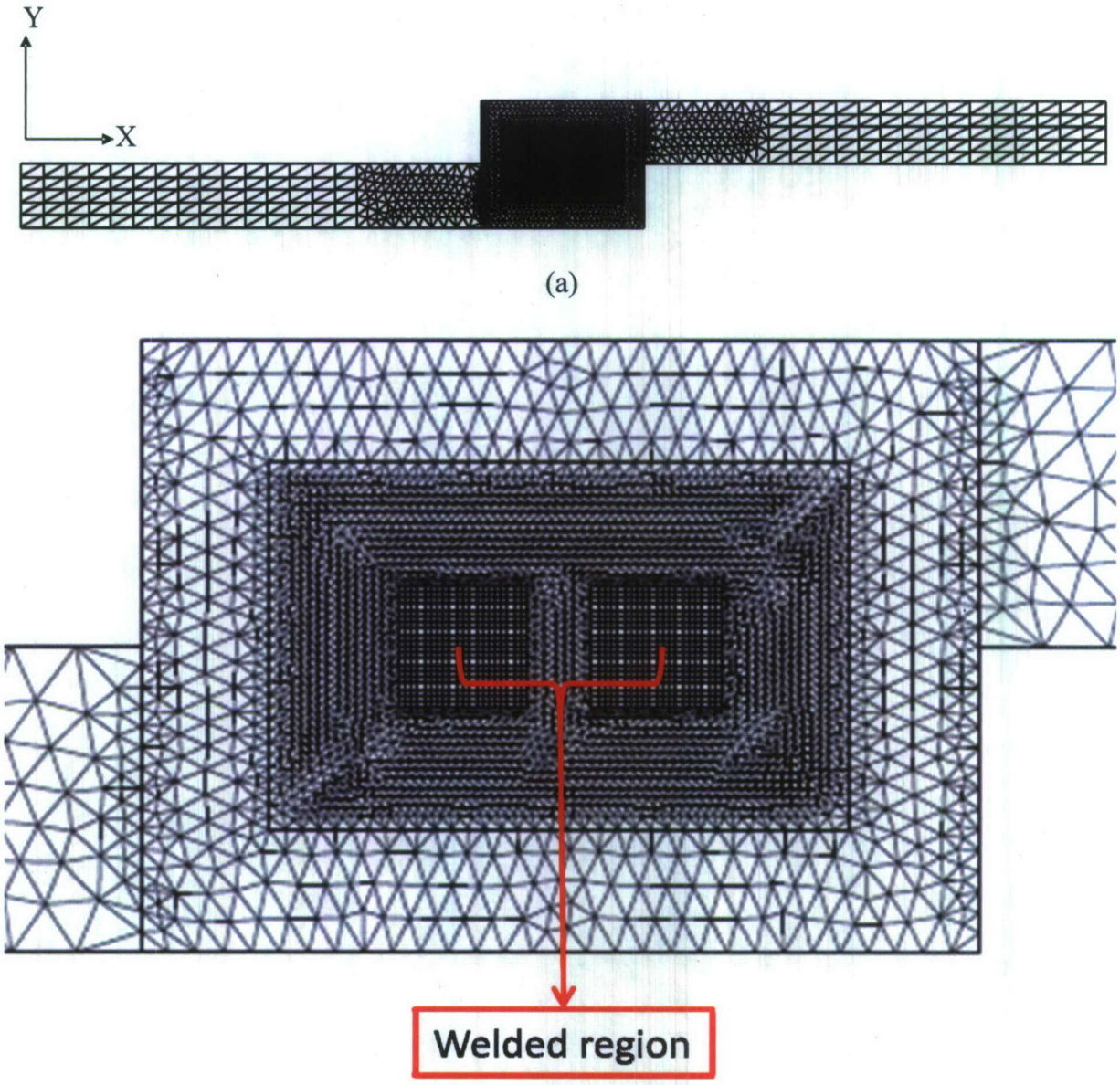

Figure 3.1 Mesh partitioning scheme on joint configuration (*H/h*=1, *w/h*=0.6, *a/h*=1) used for almost all joint configurations analyzed with FRACN2D.

allocated at the crack surfaces to enforce contact conditions. For all the joints under consideration, the problem type is selected to be plane strain. Although there are several other options in the program, only those pertaining to the work conducted in this chapter are mentioned here. Once the pre-processing is done, one has to introduce the non-welded lengths as cracks.

3.2.2 Creation of cracks

In FRANC2D, the user can change the geometry as well as the mesh of the structure which is essential for performing the desired fracture analyses. It may include addition or deletion of elements, introduction or propagation of the crack, and creation of material interfaces and contact surfaces. For the current purpose, two new cracks (to model the non-welded overlapped lengths) are introduced in the model on either side of the known welded length. Cracks can be non-cohesive (traction free crack surfaces), cohesive or those with gap elements. Gap elements are utilized in the present analysis to model contact between the plates in the non-welded overlap region. The entire process of crack creation is graphically shown in Fig. 3.2 (a), (b), (c), (d) and (e). Upon specification of an edge crack, the program deletes the elements around the crack path, creates crack surfaces with gap elements, forms a rosette of eight six-node triangular T6 elements around the crack-tip, and later meshes the deleted region using the quad-tree algorithm, which produces a good mesh consisting of T6 elements around the crack.

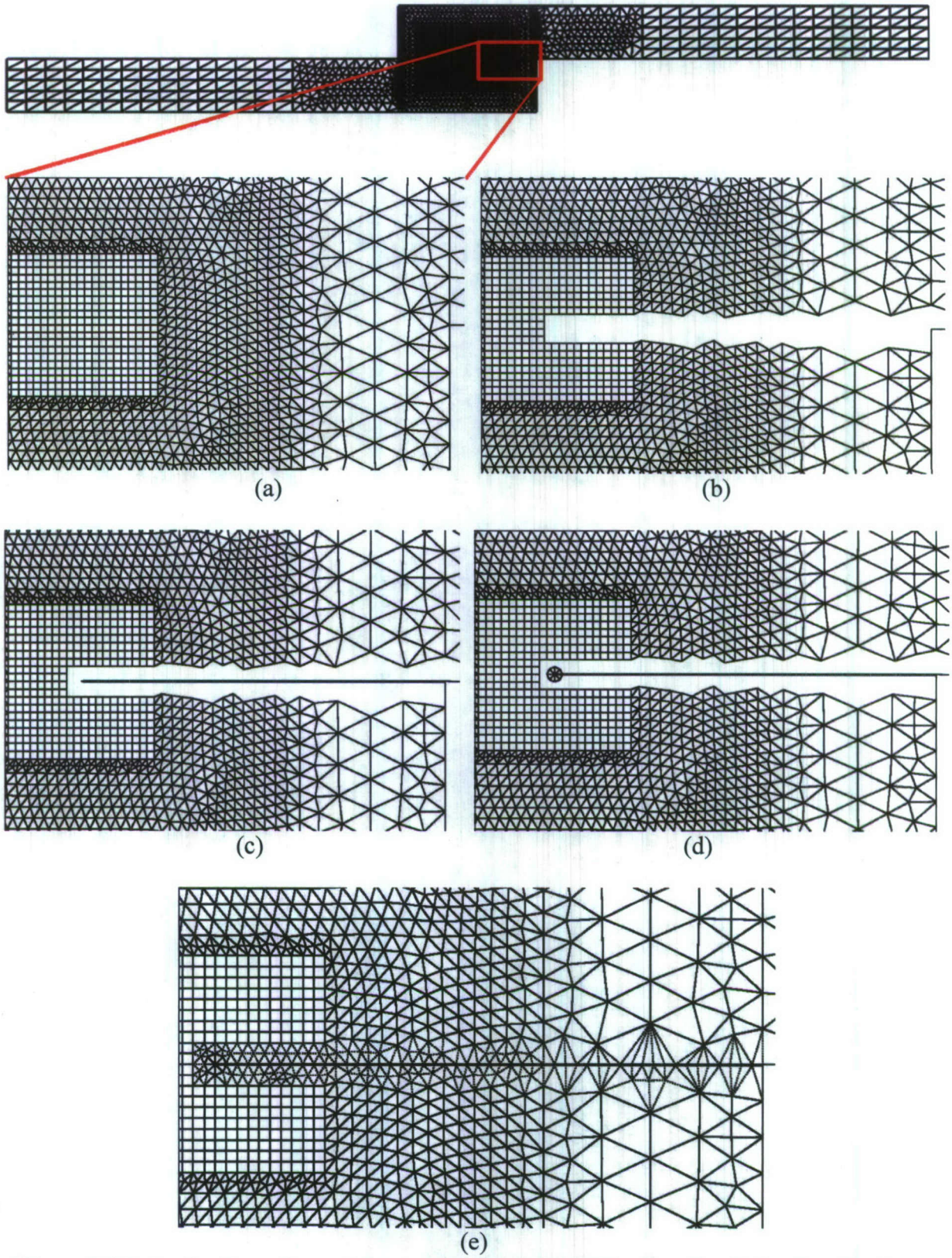

Figure 3.2 Introduction of an edge crack in the joint ($H/h = 1$, $w/h = 0.6$, $a/h = 1$) where, (a)section of Fig.3.1(b), (b)deletion of surrounding elements, (c)creation of crack surfaces, (d)creation of the rosette at the crack tip, (e)complete mesh.

3.2.3 Analysis

Two types of solvers are available in FRANC2D namely, direct stiffness and dynamic relaxation. Direct stiffness is a standard Gauss elimination solver for linear problems, while dynamic relaxation is used for problems containing gap elements (or rather any geometric nonlinearity, such as contacts). A convergence tolerance has to be specified for the dynamic relaxation algorithm. Smaller tolerances generally yield more accurate results at the expense of computational time.

3.3 Convergence

To ensure that the mesh is sufficiently refined and that the results have converged, the center crack model previously analyzed using the program ABAQUS is made and meshed in CASCA. Two types of element distributions are seen while creating mesh in CASCA and FRANC2D, namely, number of elements around the crack (EAC) and the number of elements over the crack length (EOCL). EAC is defined as the number of element seeds, at one edge of the innermost rectangular partition of the CASCA mesh, around the crack tip and EOCL defines the number of elements along the crack length (during mesh modification in FRANC2D), which is shown in Fig. 3.2(d). As the effect of these element density parameters on the final analysis result is not known a priori, the following studies are conducted; EOCL is fixed and EAC is increased, EAC is fixed and EOCL is increased, and both EAC and EOCL are increased simultaneously. The results are shown in Table 3.1(a). When EOCL is fixed at 40 and EAC is increased from 20 to 50 elements, the difference between the obtained stress intensity factors and analytical results remained almost unchanged. Similar results are obtained in the third

(a)

EOCL	EAC	MCC* K_I	Analytical K_I	Difference (%)
40	20	77.79	79.27	1.867
40	30	77.93	79.27	1.690
40	40	77.93	79.27	1.690
40	50	77.91	79.27	1.716

EOCL	EAC	MCC* K_I	Analytical K_I	Difference (%)
20	20	78.58	79.27	0.870
25	25	78.61	79.27	0.833
30	30	78.54	79.27	0.921
40	40	78.52	79.27	0.946
50	50	78.44	79.27	1.047

EOCL	EAC	MCC* K_I	Analytical K_I	Difference (%)
10	50	79.3	79.27	0.038
20	50	79.13	79.27	0.177
25	50	79.08	79.27	0.240
30	50	78.97	79.27	0.378
40	50	78.66	79.27	0.770
50	50	78.44	79.27	1.047

EOCL	EAC	MCC* K_I	Analytical K_I	Difference (%)
10	40	79.03	79.27	0.303
20	40	78.98	79.27	0.366
30	40	78.76	79.27	0.643
40	40	78.52	79.27	0.946
50	40	78.24	79.27	1.299

(b)

FRANC2D					ABAQUS		Difference (%)	
EOCL	EAC	Tolerance	K_I	K_{II}	K_I	K_{II}	K_I	K_{II}
8	20	10^{-7}	2.118	1.168	2.113	1.299	0.237	10.085
10	20	10^{-6}	2.116	1.289	2.113	1.299	0.142	0.770
10	20	10^{-7}	2.12	1.291	2.113	1.299	0.331	0.616
20	20	10^{-6}	2.115	1.168	2.113	1.299	0.095	10.085

*MCC is Modified Crack Closure Method of computing SIFs.
**Unit of stress intensity factors listed in the table is, psi$\sqrt{in}$

Table 3.1(a) Convergence study using center crack model, (b) Comparison of FRANC2D and ABAQUS results, for a representative joint configuration ($H/h = 1$, $w/h = 0.6$, $a/h = 1$).

case by increasing both the element distribution parameters from 20 to 50. For the second study, when EAC is fixed at 50 elements it is observed that the difference increases with EOCL being increased from 10 to 50 elements. Thus, the best result occurs at an EOCL of *10*. The same procedure is repeated for EAC numbers of 40, 30 and 20 with the EOCL element number increasing from 10 to 50. It is clearly seen that with an increase in the EOCL parameter, the difference increases. Therefore, for almost all meshes generated in this chapter, an EOCL of 10 is selected.

Once an appropriate number of elements to be used around the crack tip and elements over the crack length are determined using center crack FE model, the next step is to make sure that these modeling parameters also provide accurate results in the lap joint models. To examine this, several mesh convergence partitioning schemes were analyzed for a joint configuration of $H/h = 1$, $w/h = 0.6$, and $a/h = 1$. The two partitioning schemes used are displayed in Figs. 3.3(a) and (b). The mesh partitioning scheme plays a significant role in the numeric value of the output. It is expected that the finer the element mesh the more accurate the stress distribution results will be.

The model shown in Fig. 3.3(a) has an EAC of 80 and EOCL of 10. It exhibits a difference of 6% in the K_I value and 4% in the K_{II} value when compared to those obtained using ABAQUS for the same joint geometry. The model shown in Fig. 3.3(b) is partitioned in such a way as to obtain a more refined mesh around the crack tips with an EAC of 20 and EOCL of 10. Table 3.1(b) compares results obtained using FRANC2D for the mesh distribution shown in Fig. 3.3(b) with those obtained from ABAQUS for a joint of dimensions $h = H = a = 1$, $w = 0.6$ subjected to a unit moment. The results

(a)

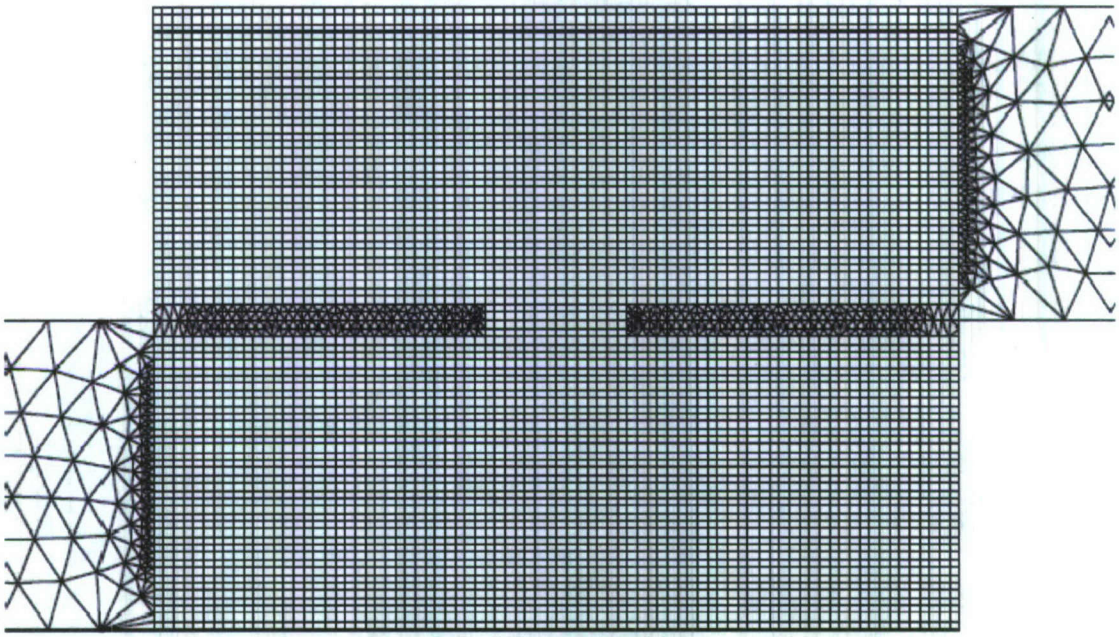

(b)

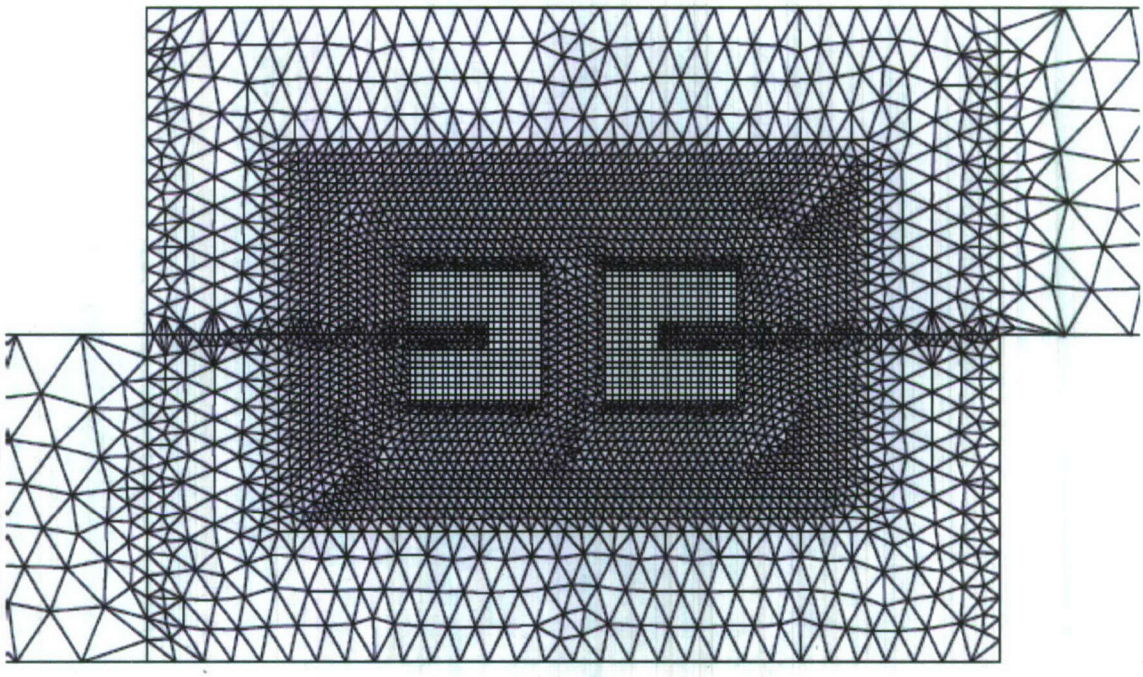

Figure 3.3: Mesh partitioning schemes of (a)80 elements and (b)20 elements on one side of the innermost rectangular section, on the joint configuration ($H/h = 1$, $w/h = 0.6$, $a/h = 1$).

given in the table demonstrate that, for this mesh scheme, tighter convergence tolerances for the dynamic relaxation algorithm is really not beneficial and an EOCL of 10, an EAC of 20 with a tolerance of 1×10^{-6} gives sufficiently accurate results. As it provides satisfactory results and reduces computer run time, a similar mesh partitioning scheme, as the one shown in Fig. 3.3(b) with four levels of partitions, is selected for the joint configurations considered here.

3.4 Crack Propagation Method

In Chapter 2, the static fracture strength of the joint was obtained by studying fracture initiation at the notches. In addition to the static fracture strength, it is helpful to understand crack growth and corresponding residual strength of the joint. Accordingly, a sequential crack propagation analysis is performed using FRANC2D in this section. A failure criterion which uses stress intensity factors to determine crack initiation angle under mixed mode conditions is discussed in Section 2.4. As an extension to that methodology, crack propagation can be considered as a step-by-step fracture process using the maximum tensile stress failure criterion. Crack propagation analysis begins with a previously defined crack. There are generally three methods to propagate a crack using FRANC2D, which are as follows; the standard method which allows the user to specify a crack length increment and direction, the interface method which is used when the crack tip is located at a bimaterial interface, and the automatic method. For the purposes of this work, the standard crack propagation algorithm is chosen as it is the most appropriate.

At each step of the crack propagation process, the stress intensities are first obtained by the Modified Crack Closure technique. These stress intensity factor values

are used to calculate the increment in crack length which is then supplied to the program manually (refer Section 3.5). Referring to the method outlined in Section 2.4, FRANC2D then evaluates the crack propagation angle for each crack using the maximum tensile stress criterion. Subsequently, the changes in crack geometries are incorporated into the existing finite element model and the elements around the new cracks are regenerated. Thereafter, the model is analyzed by the dynamic relaxation algorithm and the new stress intensity factors at the new crack tips are probed from the program output. This procedure is repeated until a crack surface reaches very close to a boundary or another crack surface. Fig. 3.4 shows the modified joint configuration during the sequential crack propagation process at the 3^{rd}, 8^{th} and 16^{th} step for the joint JC:1-0.6-1 under axial tension. The entire stress intensity factor history which is obtained as a function of the crack length is then utilized in the fatigue analysis of the joint as described in Section 3.6. In this whole process of crack growth, the propagation angle is independent of the fracture toughness and yield strength, as also shown in Section 2.4, Equation (6). Therefore, there would not be any change in the trajectory for different steels within the range of applicability of LEFM. However, it should be noted that the residual strength of the joint (which can also be called as critical moment of the joint) depends on the fracture toughness K_{Ic} of the material.

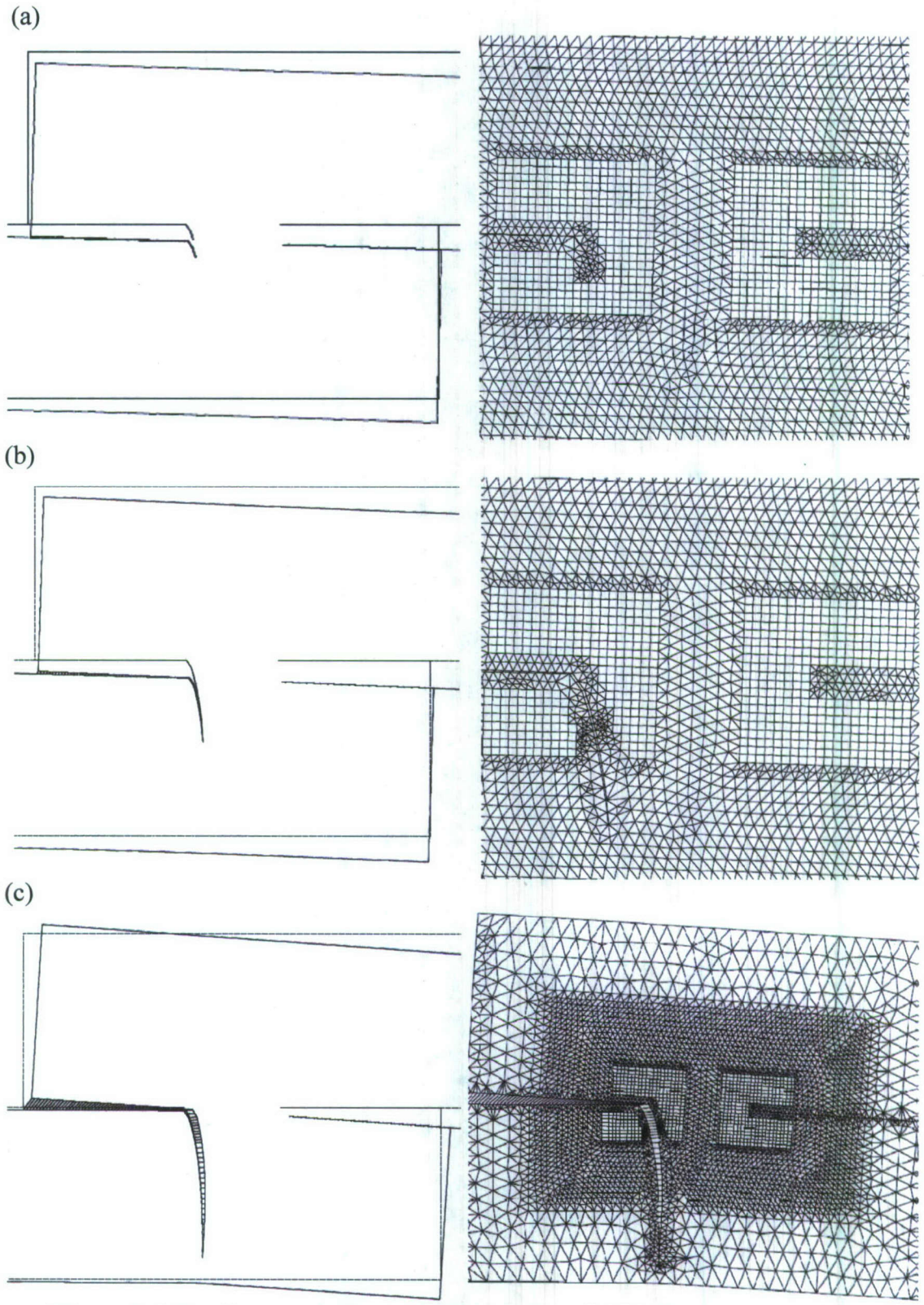

Figure 3.4 Crack propagation process at 3, 8 and 16 increment steps (a – c respectively) on the joint JC:1-0.6-1 under P^+ load.

Except for one joint geometry, which is common among all the load cases, an additional joint configuration has also been examined for each load case. All reported quantities discussed later in this chapter are normalized with respect to either the upper plate thickness h, applied moment load M or tensile load P, critical stress intensity factor K_{Ic}, other material constants, or a combination of these, and are denoted with bar over the quantity. These normalized quantities are listed hereunder,

- Crack extension,

$$\bar{e} = \frac{e}{h},$$

- Stress intensity factor for applied moment or tensile load,

$$\overline{K_i} = K_i \frac{h^{\frac{3}{2}}}{M}, \qquad OR \qquad \overline{K_i} = K_i \frac{h^{\frac{1}{2}}}{P}$$

- Critical moment or residual strength,

$$\overline{M_c} = \frac{M_c}{h^{\frac{3}{2}}.K_{Ic}},$$

- Critical tensile force or residual strength,

$$\overline{P_c} = \frac{P_c}{h^{\frac{1}{2}}.K_{Ic}},$$

where, subscript i denotes the fracture mode. To simplify and ease the understanding of the results, the following terminology is used to define the joint geometries,

Joint Configuration

$$\hookrightarrow JC: \frac{H}{h} - \frac{w}{h} - \frac{a}{h}, Location$$

In the box above, the ratios following the colon are,

H/h = ratio of plate thicknesses,

w/h = ratio of the weld-width to the upper plate thickness, and

a/h = ratio of the non-welded overlapped length to the upper plate thickness.

Here 'Location' is used to indicate results for the right or the left notch using the letters 'R' or 'L', respectively. For example, JC:2.5-0.2-1,L would indicate the results correspond to the left notch of joint configuration $H/h = 2.5$, $w/h = 0.2$ and $a/h = 1$.

3.5 Power-Law Crack Growth Model

In a body with multiple cracks, such as the lap joint configuration discussed here, it is assumed that each crack will propagate by different amounts which would depend on their stress intensity factors. The following power-law equation is commonly employed (FRANC3D manual v2.6) to determine the change in crack lengths at each step of the crack propagation process,

$$\Delta\bar{e}_i = \Delta\bar{e}\,\frac{\left(K_{eff}^{i}\right)^{m}}{\left(K_{eff}^{max}\right)^{m}}, \tag{25}$$

where, i is the crack number, $\Delta\bar{e}$ is the prescribed maximum normalized crack increment for the step, K^{i}_{eff} is the effective stress intensity factor of the i^{th} crack, K_{eff}^{max} is the largest value of the effective stress intensity factor of all cracks and b is a power exponent. Considering an example, the law states that if there are two cracks and the maximum effective stress intensity factor occurs at crack 1, then crack 1 will propagate by the specified maximum value $\Delta\bar{e}$ while crack 2 will extend by a fraction of the specified increment as computed by the preceding equation. If the power-law exponent b is chosen to be a large value then crack 2 will propagate by a smaller amount. The power-law exponent b is chosen to be 3.0 in the present analysis. The selection of this value is discussed in detail in the fatigue section (Section 3.6) of the chapter. It should be noted

that this power-law only gives information about the amount by which a crack will propagate and does not produce the stress intensity factors at the end of the increment.

3.6 Fatigue Analysis

In the early 1960's, it was demonstrated that fracture mechanics is a useful tool for investigating fatigue crack propagation. In this section, we discuss the fatigue analysis of a laser-welded joint under constant amplitude cyclic loading. Consider a crack under constant amplitude cyclic load ΔM. Based on the assumption of stress intensity factor being directly proportional to the applied load, the stress intensity amplitude ΔK at the crack tip has a cyclic variation as depicted in Fig. 3.5. If the cyclic plastic zone formed at the crack tip is small, the crack growth rate can be defined by the expression:

$$\frac{de}{dN} = f(\Delta K, R), \tag{26}$$

where $\Delta K = (K_{max} - K_{min})$ is the amplitude, $R = K_{min}/K_{max}$ is the load ratio, e is the crack extension measured from the notch tip in the undamaged configuration and de/dN is the crack growth per cycle. A typical fatigue crack growth curve for metals is illustrated in Fig. 3.6 on a log-log plot of de/dN versus ΔK. The sigmoidal curve has three regions. The high and low ΔK levels show non-linearity, while in the intermediate region or region-II, the curve is linear. At the low end, when ΔK value is less than the threshold value ΔK_{th}, de/dN approaches zero, which means that the crack will not grow. For high

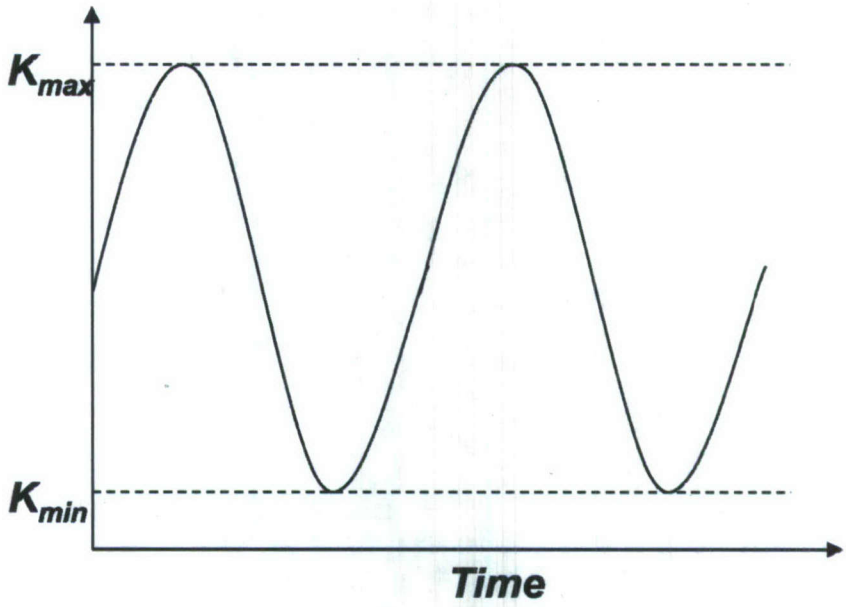

Figure 3.5: Constant amplitude stress intensity factor at the crack tip due to applied cyclic load.

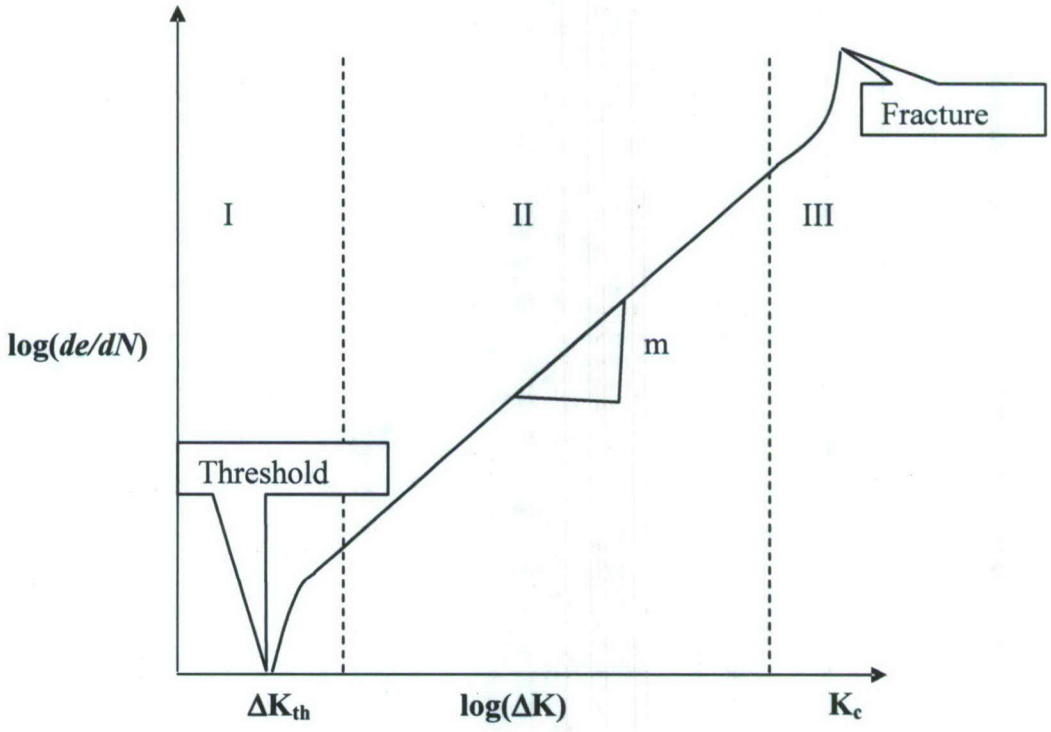

Figure 3.6: Typical fatigue crack growth behavior in metals.

ΔK values, the most widely accepted hypothesis is that crack growth rate accelerates as K_{max} approaches the fracture toughness of the material K_{Ic}. For intermediate values of ΔK, namely within region-II, the crack growth rate can be described by the power law expression of Paris and Erdogan (1960),

$$\frac{de}{dN} = C\,\Delta K^m, \tag{27}$$

where ΔK is amplitude of the cyclic stress intensity factor, and C and m are material constants which are obtained experimentally. Studies have shown that the exponent m ranges from 2.0 to 7.0 for most materials. Equation (27) is widely referred to as the *Paris Law*. After Paris's work a number of researchers have developed equations to model all or part of the sigmoidal curve. Some researchers proposed a relationship for region-II and III, assuming that region-III is caused by superposition of fracture and fatigue rather than plastic zone effects. A number of equations attempt to describe crack growth in all three regions. A simplified form of one such equation given by Forman (1967) is:

$$\frac{de}{dN} = \frac{C\Delta K^m}{\left((1-R)K_c - \Delta K\right)} \tag{28}$$

At region-II, equation (28) will reduce to equation (27). Generally these equations contain four material constants: C, m, K_c, and ΔK_{th}. None of these equations have history dependence, and thus, are only valid for constant (stress intensity) amplitude loading.

The objective of the fatigue crack propagation analysis is to predict the fatigue life of the joint. This can be defined as the number of cycles required for the specimen to fail at prescribed stress amplitude. FRANC2D finite element program is used to propagate the crack and obtain the history of stress intensity factors at each crack tip. All

crack growth analyses are carried out until a crack extends very close to a boundary or another crack surface.

A MATLAB program is written to compute the crack extension as a function of the number of cycles using the stress intensity factor histories obtained from FRANC2D. This is achieved by integrating the Paris Law. The power law exponent m in the Paris law is chosen to be that of mild steel m = 3.0 (Barsom 1971). The non-dimensional results presented in the following sections are independent of the material constant C in the Paris law. The mathematical steps involved in this formulation are summarized below. Consider the propagation of the crack that originates from the right notch of a joint that is subjected to a positive cyclic moment. The following expressions for the mode I and II stress intensity factor were presented previously,

$$\Delta K_i^{M+,r} = \frac{\Delta M}{h^{\frac{3}{2}}} . f_i^{M+,r}\left(\frac{H}{h}, \frac{w}{h}, \frac{a}{h}, \frac{e}{h}\right), \tag{29}$$

where the subscript i signifies the mode. For any arbitrary moment, ΔK depends on ΔM, h and the crack extension. It should be noted that for fatigue analysis, the non-dimensional stress intensity factor $f_i^{M+,r}$ is also a function of the crack extension e/h, which is different from non-welded overlap length a/h. For fatigue crack propagation, a particular joint geometry needs to be focused on and thus other dimensions (w/h, H/h and a/h) are considered to be fixed. The above equation can thus be simplified as,

$$\Delta K = \frac{\Delta M}{h^{\frac{3}{2}}} . f\left(\frac{e}{h}\right), \tag{30}$$

Substitution of equation (30) into equation (27) gives

$$\frac{de}{dN} = C.\left[\frac{\Delta M}{h^{3/2}} . f\left(\frac{e}{h}\right)\right]^m, \tag{31}$$

which when integrated yields

$$\frac{1}{C}\left(\frac{h^{3/2}}{\Delta M}\right)^{m} \cdot \int_{0}^{e_o} \frac{de}{f\left(\frac{e}{h}\right)^{m}} = \int_{0}^{N} dN = N, \tag{32}$$

Equation (34) can be expressed in a more simplified form as,

$$N = \frac{1}{C} \cdot \frac{h^{\left(\frac{3m}{2}+1\right)}}{(\Delta M)^{m}} \cdot \int_{0}^{e_o} \frac{d\left(\frac{e}{h}\right)}{f\left(\frac{e}{h}\right)^{m}}, \tag{33}$$

where, ΔM is the moment amplitude. The above equation (equation (33)), is then numerically integrated using an adaptive simpson quadrature technique. The factor f obtained at each step by applying a unit moment ΔM to a joint of unit thickness h, is really the stress intensity factor ΔK, i.e., $\Delta K = f(e/h)$ from equation (30). The stress intensities obtained at each crack increment has been recorded and while considering mixed mode fracture conditions, effective stress intensity factor (ΔK_{eff}) is calculated from them. The following effective stress intensity factor is used since it gives good correlation with experimental results (Qian and Fatemi, 1996),

$$\Delta K_{eff} = \left[\Delta K_I{}^4 + 8.\Delta K_{II}{}^4\right]^{1/4}, \tag{34}$$

The total crack extension range is divided into n segments, and at each segment ΔK_{eff} is evaluated by performing cubic interpolation. The ΔK_{eff} is normalized with respect to the applied load and upper plate thickness (h) as given among the normalized equations in Section 3.4.

Six joint configurations are selected to be studied for fatigue life predictions, of which, one is set to be common among each loading case. Plots of the normalized number of cycles versus normalized crack extension are shown for each loading case. There normalized number of cycles for the moment and tensile loads are defined as,

$$\bar{N} = (\Delta\bar{M})^m N, \tag{35}$$

where $\Delta\bar{M} = \frac{C^{1/m}\Delta M}{h^{(\frac{3}{2}+\frac{1}{m})}}$, and

$$\bar{N} = (\Delta\bar{P})^m N, \tag{36}$$

where $\Delta\bar{P} = \frac{C^{1/m}\Delta P}{h^{(\frac{1}{2}+\frac{1}{m})}}$. By normalizing the number of cycles, the $\bar{N} - \bar{e}$ plot becomes independent of the material constant C, load ΔM or ΔP, and upper plate thickness h.

In the manual crack growth propagation analysis performed here, stress intensities at both the notches are obtained and an effective stress intensity factor is evaluated (equation (34)) at every crack increment. One tip at a time is selected and an increment size for each crack tip is calculated using the following procedure and is supplied to the program. Let ΔK_1 and ΔK_2 denote the effective stress intensity factors at the 1st and 2nd crack tips of the joint, respectively. For a specified increment of load cycles ΔN the crack extensions Δe_1 and Δe_2 will be different. It is safe to assume here that the SIF of one crack tip would be greater than the other, say $\Delta K_1 > \Delta K_2$. The crack with the largest stress intensity factor is allowed to propagate by the maximum crack increment $\Delta e_1 = \Delta e$. Each step of the crack propagation analysis corresponds to a fixed number of cycles, i.e., $\Delta N_1 = \Delta N_2 = \Delta N$. On the basis of Paris Law,

$$\frac{\Delta e_1}{\Delta N} = C(\Delta K_1)^m, \tag{37}$$

$$\frac{\Delta e_2}{\Delta N} = C(\Delta K_2)^m, \tag{38}$$

Dividing equation (37) by equation (38),

$$\Delta e_2 = \Delta e \left(\frac{\Delta K_2}{\Delta K_1}\right)^m, \tag{39}$$

This explains that the extension of crack 2 is a fraction of the extension of crack 1. Comparing this with equation (25), it can be inferred that power b is actually the material constant m of the *Paris Law*. Therefore, a power value of $b = 3.0$ is used so that the results obtained from the crack propagation analyses can be further utilized for fatigue life prediction.

3.7 Results and Discussion

Three loading cases are presented in this section, namely, positive moment, negative moment and tensile force. Two joint configurations are discussed in each loading case. Among the two joints of each case, one is set to be common to ease the purpose of comparing the performance of one joint under different loading conditions.

3.7.1 Loading Case-I (positive moment M^+)

To ascertain the dependence of the crack propagation trajectory on the maximum crack growth size $\Delta\bar{e}$, three analyses with different normalized values of $\Delta\bar{e} = 0.1$, 0.05 and 0.025 were performed under positive moment. These analyses were run just to get an idea of the increments which should be used. The analyses are run to a maximum normalized crack extension of $\bar{e} = 0.9$ in each case. By analyzing the results based on the crack trajectory, convergence of stress intensity factor values, and the computation time taken by each of the analysis, a standard crack increment of 10% of the weld-width ratio w/h is selected for further study.

3.7.1.1 Common Joint (JC:1-0.6-1)

Manual crack propagation analysis is carried out on the joint JC:1-0.6-1 with a unit positive cyclic moment. The trajectory obtained is illustrated in Fig. 3.7. It is observed that initially both the left and right cracks begin to propagate. After few steps the left crack does not propagate further, since the computed crack growth at each step is smaller than the chosen tolerance of 0.002.

A comparative plot of the normalized effective stress intensity factors at the right and left notches versus the corresponding crack extensions $\bar{e}$ is shown in Fig. 3.8. Effective stress intensity factor values are plotted to emphasize the fact that the joint fails under mixed mode condition. The dipping down of the left notch curve shows that the left crack ceases to propagate further due to reduction in the effective stress intensity factor value.

The failure load for each crack tip is computed using the maximum tensile stress fracture criterion during the crack propagation process and the minimum of the two is chosen as the residual fracture strength of the entire joint. The notation M_c can thus be called as the residual strength of the joint at a certain step during the crack propagation process, since it is the maximum load the joint can bear just before crack propagation or material failure. Depicted in Fig. 3.9 is a plot of the normalized residual strength as a function of the normalized crack extensions of each notch. The plot is very useful for evaluating the residual strength of the joint as the cracks propagate through the structure. For a given value of the normalized crack extension of the right crack tip, the corresponding value of the residual strength can be inferred from Fig. 3.9. For example, the residual strength and crack extension of the left notch corresponding to a right notch

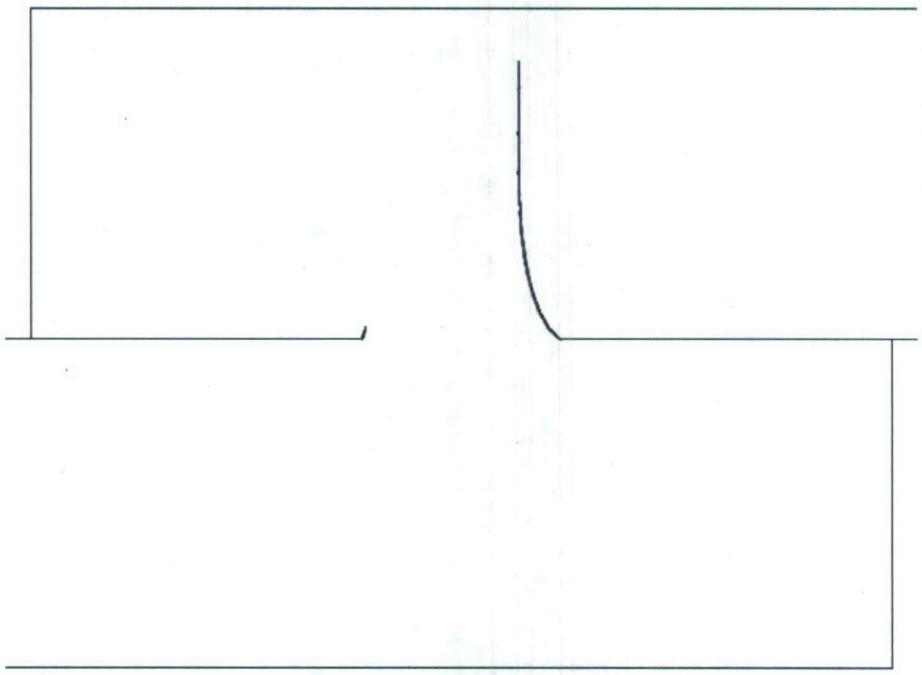

Figure 3.7: Crack propagation trajectory for M^+ load for the joint geometry ($H/h = 1$, $w/h = 0.6$, $a/h = 1$).

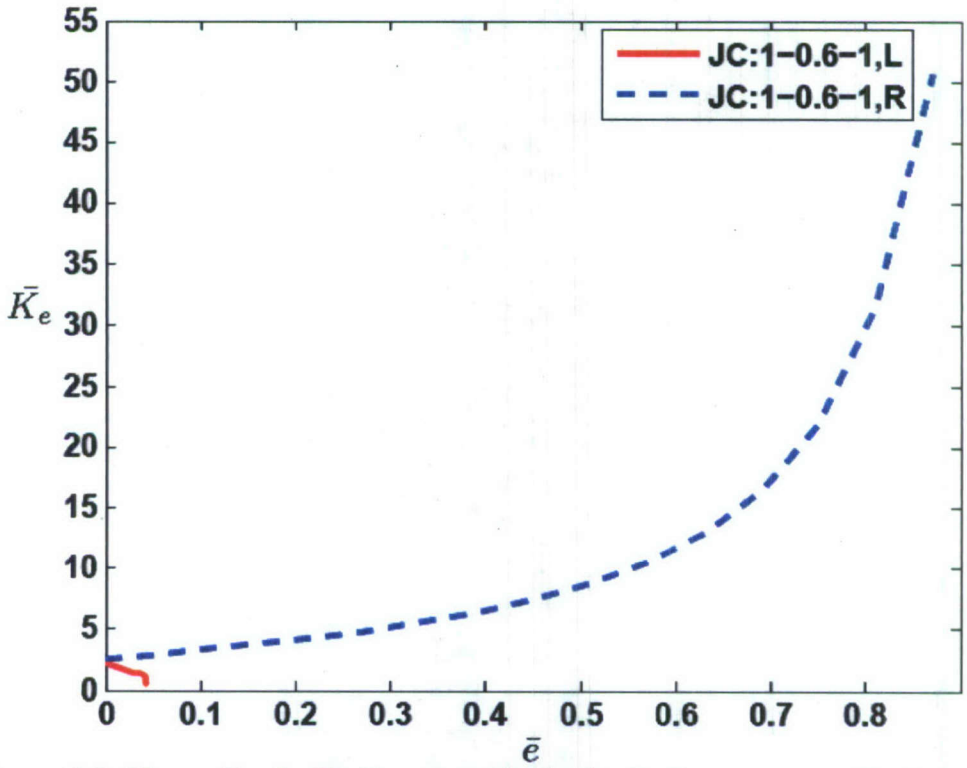

Figure 3.8: Normalized effective stress intensity factor vs. normalized crack extension under M^+ load at both the left and right notches.

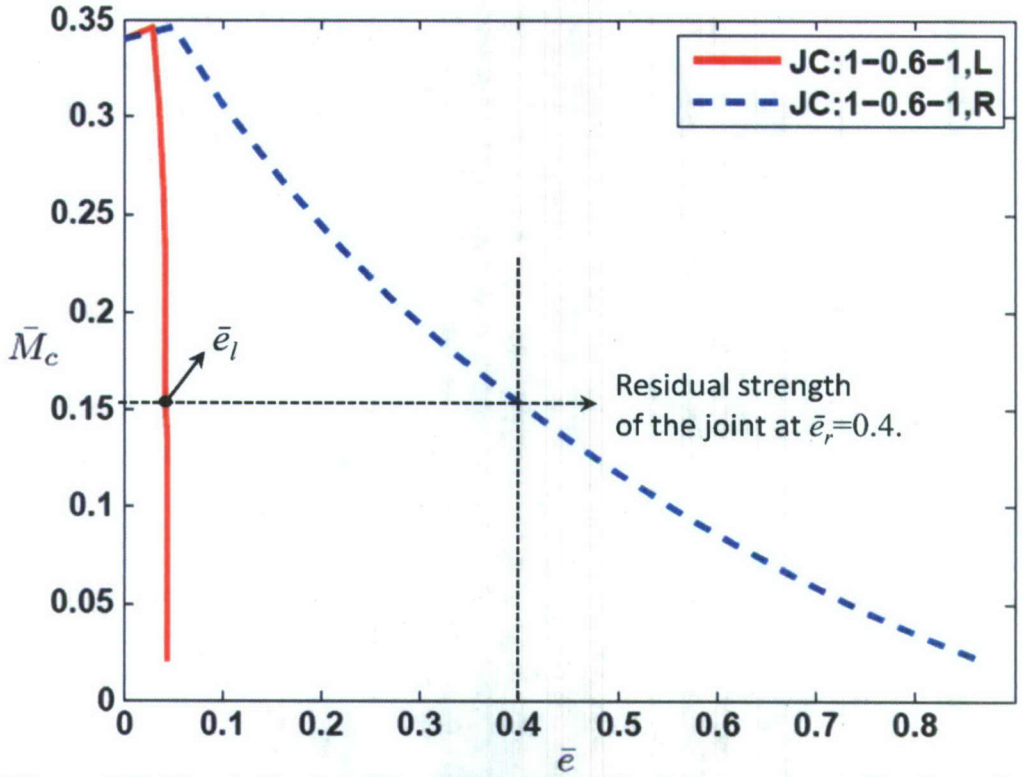

Figure 3.9: Normalized residual strength of the joint vs. normalized crack extension under M^+ load.

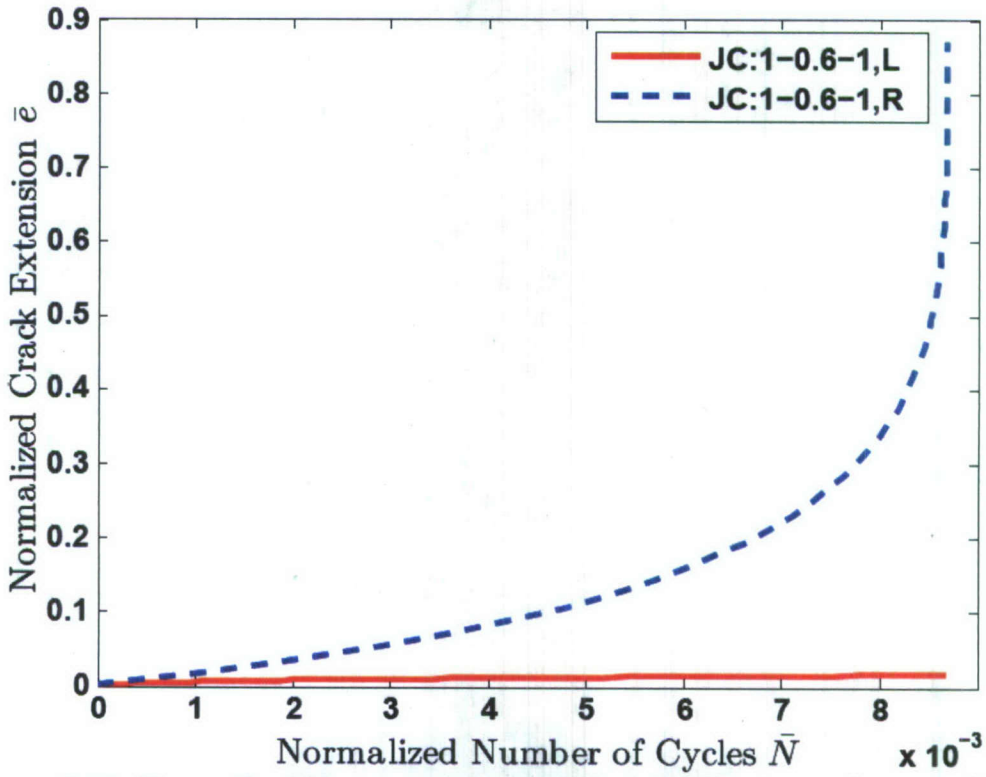

Figure 3.10: Normalized N-e curves for the left and right tips under a positive moment amplitude.

crack extension of $\bar{e}$=0.4 are $\bar{M}_c$= 0.151 and $\bar{e}_l$=0.04, respectively. It is observed that the residual strength of the joint increases a bit in the initial stages of crack growth and reaches a peak value after which it decreases monotonically. This is because the mode II stress intensity factor is significant in the undamaged joint. In the initial steps of crack propagation, the mode II stress intensity factor decreases significantly while the mode I stress intensity factor increases by only a small amount. This results in a decrease in effective stress intensity factor and therefore an increase in the residual strength. Subsequently, the mode I stress intensity factor continues to increase thus causing the residual strength to decrease monotonically.

The normalized crack extensions of both notches versus the normalized number of cycles obtained by integrating the Paris law are plotted in Fig. 3.10. The left notch propagates only up to $\bar{e}$ = 0.04. In comparison the right notch keeps growing until it reaches close to the top surface of the joint where $\bar{e}$ = 0.87. The crack growth accelerates rapidly as it approaches the upper boundary due to the sharp increase in stress intensity factor ΔK. The right crack reaches close to the upper surface at $\overline{N}$ = 0.0088 cycles. One of the benefits of plotting the normalized quantities is that it becomes possible to obtain the physical crack extension e if the number of cycles N, cyclic moment amplitude ΔM, joint thickness h and material constant C are specified. For example, if the applied cyclic moment is sufficiently small, the crack will extend to the upper surface when the normalized number of cycles is 0.0088. The normalization equation (35) can be used to determine the corresponding number of cycles N as follows,

$$N = 0.0088 \frac{h^{\frac{3m}{2}+1}}{C.(\Delta M)^m}.$$

For example, if ΔM = 1 kip-in/in, m = 3, h = 0.5" and $C = 3.6\times10^{-10}$ (in IPS units with ΔK specified in ksi-in$^{1/2}$ and e in inches in the Paris Law) the right crack will extend close to the upper surface (e = 0.435") at N = 0.54 million cycles. This will be elaborated upon in the joint case studies at the end of the Chapter. Another benefit of presenting the normalized results is that a single curve is sufficient to compute the fatigue failure limit of a joint at different load amplitudes (ΔM) and upper plate thicknesses (h). Therefore, the most desired curve $\Delta\overline{M} - N$ (also called as S-N curve) for one type of joint, can be obtained with the help of just one plot. The normalized moment amplitude has already been defined in equation (35).

If the cyclic moment magnitude is small, failure of the joint can be defined as the point at which the crack extends close to a boundary or another crack surface. In this case, the normalized number of cycles $\overline{N}$, corresponding to maximum crack extension can be used in equation (35) to obtain the normalized moment $\Delta\overline{M}$ as a function of the actual number of cycles N. The resulting $\Delta\overline{M}$ vs N curve is a straight line when plotted on the log-log axes as shown in Fig. 3.11.

3.7.1.2 Joint Configuration (JC:1-0.2-1)

Another joint configuration JC:1-0.2-1 is also studied due to its susceptibility of crack growth at both the notches under positive moment load. The joint geometry is the same as the common joint studied earlier, except for the weld width, which has been reduced to w/h = 0.2. The details of the joint and the corresponding crack trajectory are shown in Fig. 3.12. Initially, the right crack grows with maximum increments while the left one propagated with smaller ones. Due to propagation of right crack towards the

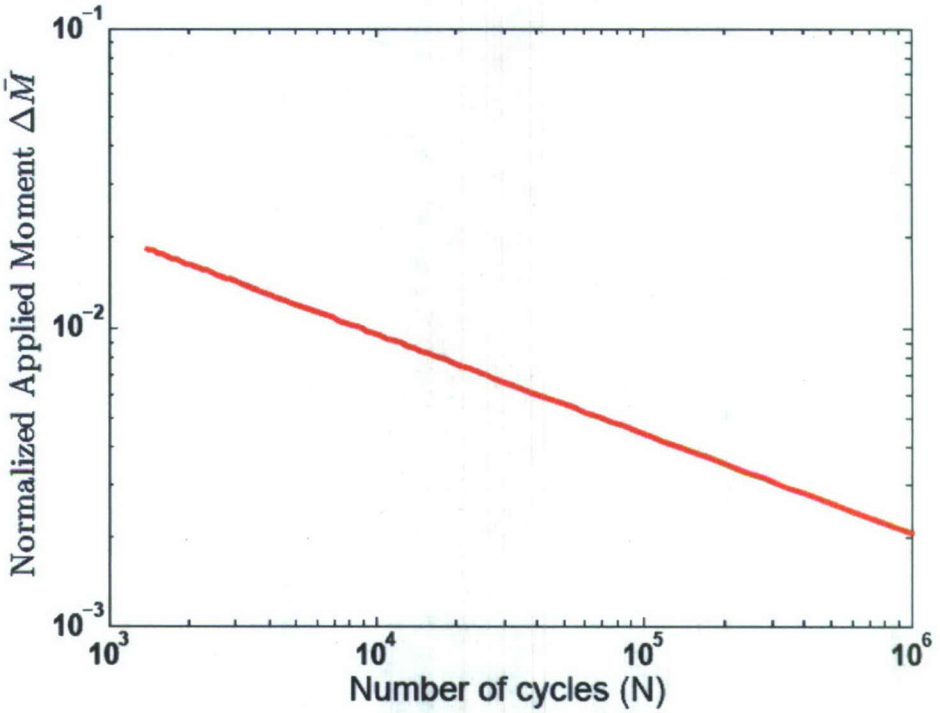

Figure 3.11: Log-log $\Delta\bar{M}$-N (or fatigue life) plot with positive moment amplitude for the joint JC:1-0.6-1.

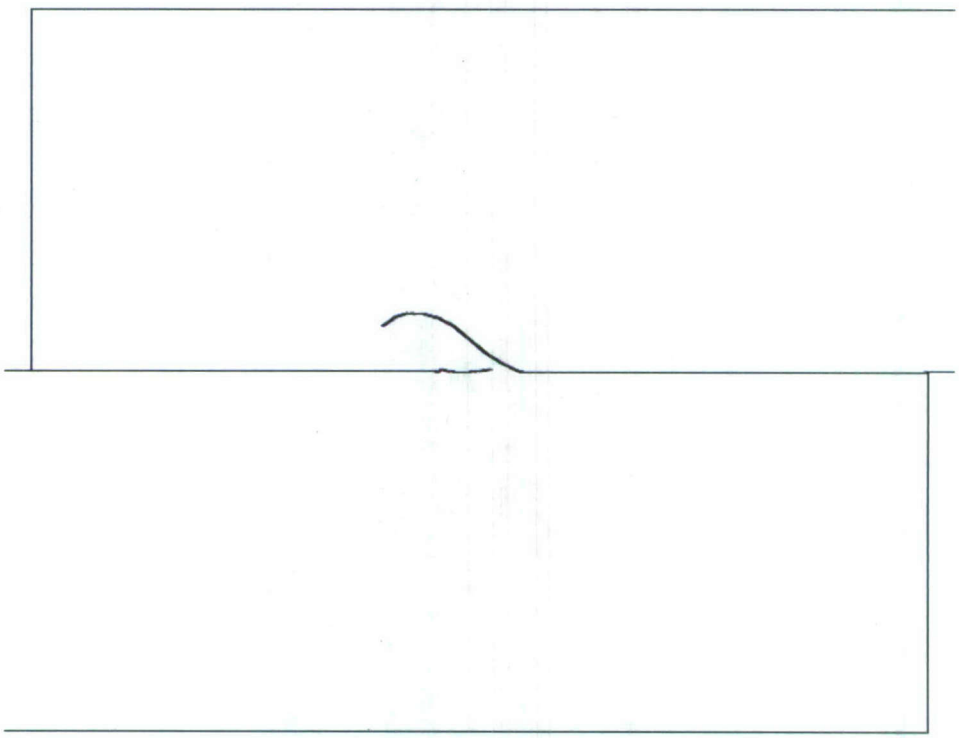

Figure 3.12: Crack propagation trajectory for M^+ load for the joint (H/h = 1, w/h = 0.2, a/h = 1).

other crack tip through the weld, within a few steps the rate of propagation of the left crack also increases with an increase in the increment size. The analysis is terminated when the left crack tip approached the right crack surface. It is observed that JC:1-0.2-1 has a very localized failure in the welded region.

A comparative plot of normalized effective stress intensity factors at the right and left notches versus $\bar{e}$ is shown in Fig. 3.13. As explained above, the plot illustrates that initially the right crack had higher stress concentration and that it grows with maximum supplied increments. Although the left notch propagated with a smaller crack increment calculated on the basis of equation (39), it shows a higher growth rate which is the effect of high stress concentration developed due to two very close crack tips.

The curve shown in Fig. 3.14 depicts the normalized residual strength of the joint at certain normalized crack extensions. It is observed that the residual strength of the joint decreases rapidly in the initial stages of crack growth.

Fig. 3.15(a) illustrates the normalized number of cycles versus normalized crack extension curves for both the notches in the joint considered. The convergence of the red curve at $\overline{N} = 0.0034$ signifies that, at this $\overline{N}$, the left crack grows steeply and meets all the way to the right crack surface which results in the failure of the joint.

As done before, the normalized number of cycles to failure $\overline{N} = 0.0034$ is used in conjunction with equation (35) to obtain the fatigue life curve shown in Fig. 3.15(b). A comparison of $\overline{N}$ at maximum crack extension for joints JC:1-0.6-1 and JC:1-0.2-1 shows that the fatigue life N for a given cyclic load decreases by 61.36% if the weld-width is decreased from w/h=0.6 to w/h=0.2.

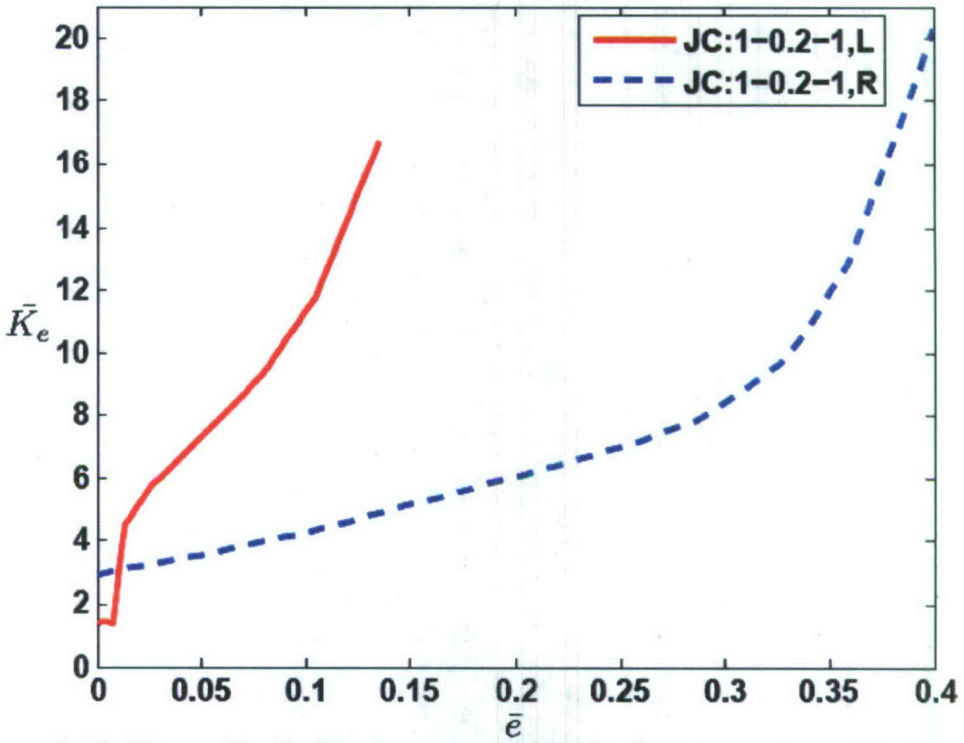

Figure 3.13: Normalized effective stress intensity factor vs. normalized crack extension under M^+ load at both the left and right notches.

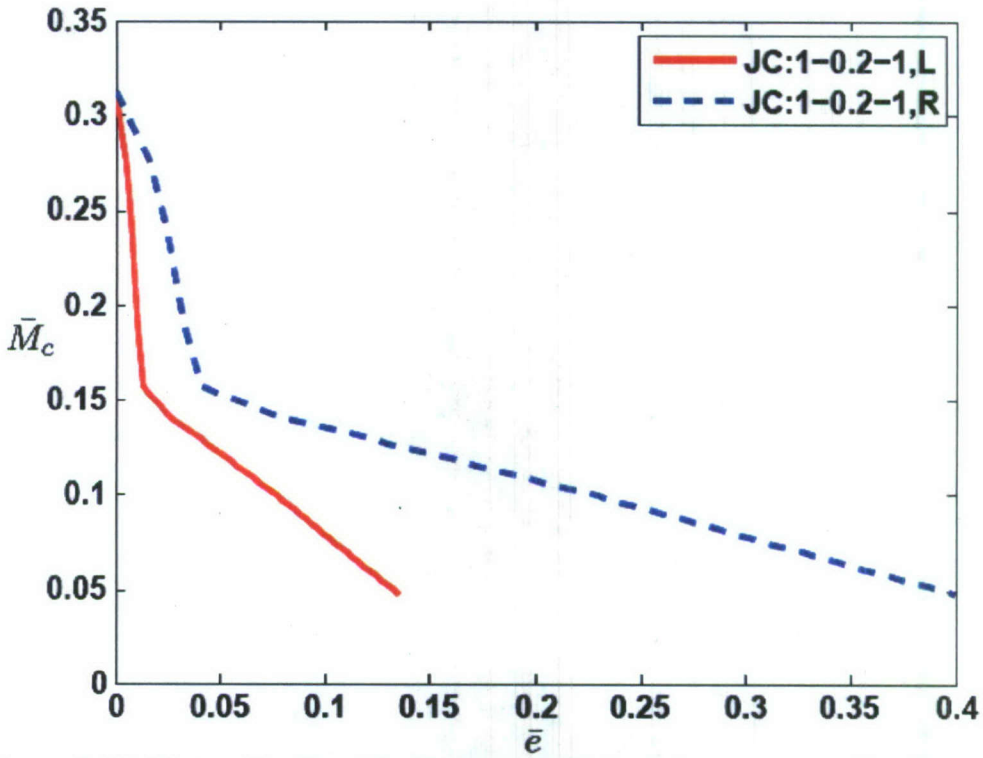

Figure 3.14: Normalized residual strength of the joint vs. normalized crack extension, under positive moment.

(a)

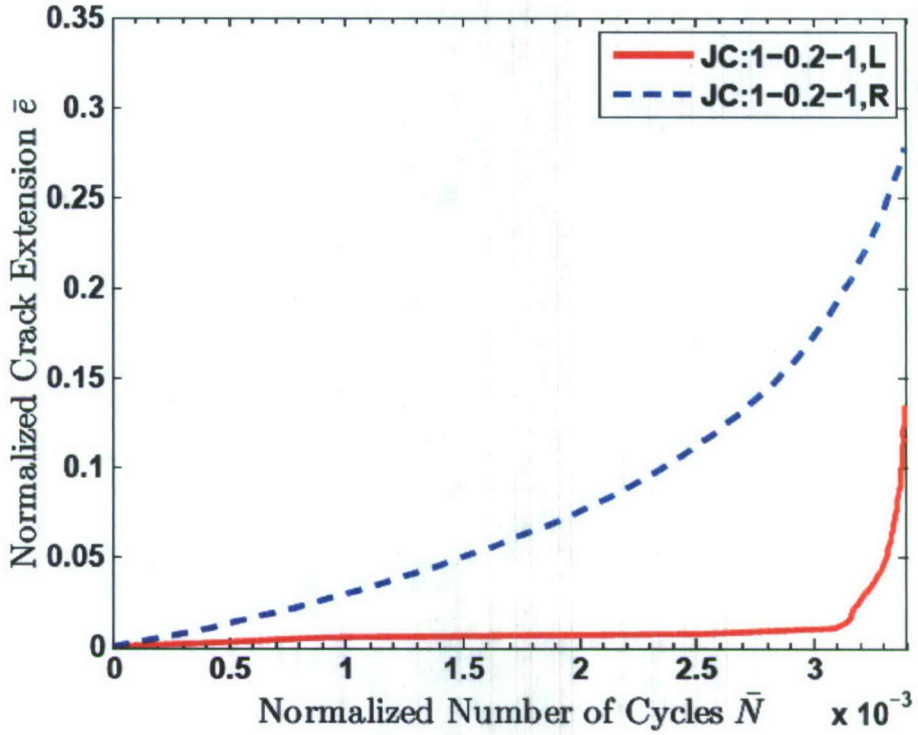

(b)

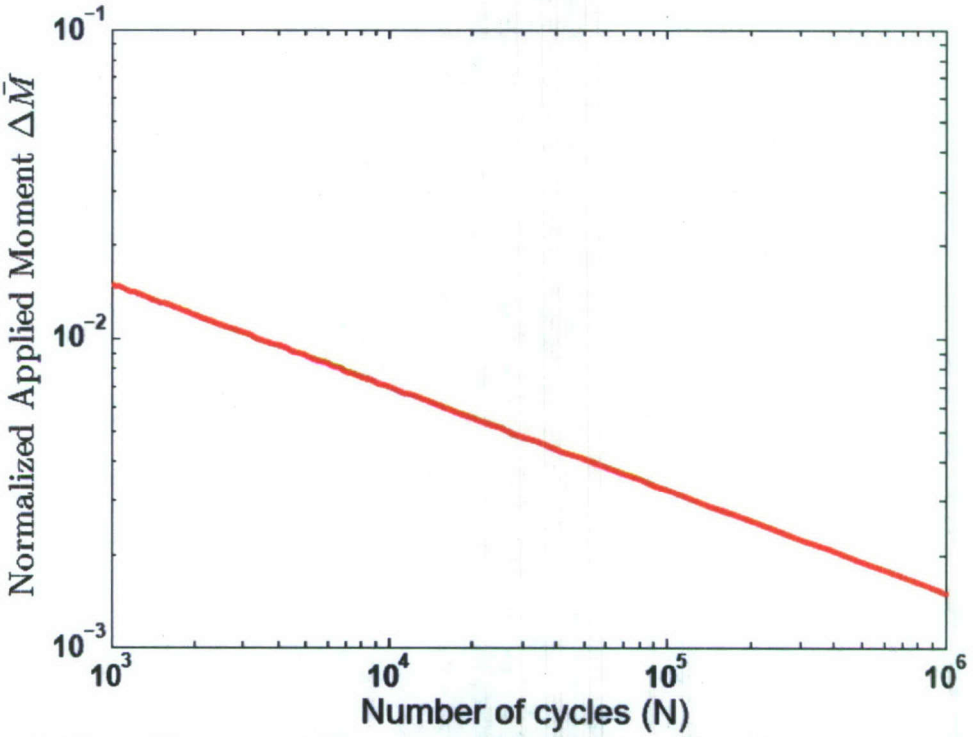

Figure 3.15: (a) Normalized N-e curves for the left and right tips, and (b) Fatigue life plot, for JC:1-0.2-1, under positive moment amplitude.

3.7.2 Loading case-II (Negative Moment, M^-)

Crack propagation analysis is also carried out for a negative moment load case. Two joint configurations JC:1-0.6-1 and JC:2.5-0.2-1 are selected to be analyzed under this loading condition.

3.7.2.1 Common Joint (JC:1-0.6-1)

On the common joint geometry (JC:1-0.6-1), 16 manual propagation steps, with a power value of 3, are performed. Fig. 3.16(a) illustrates the crack trajectory at both the right and left notches. The right crack trajectory shows a small dip down, which signifies the presence of hinging effect discussed in Section 2.6.5. However, it has been observed that for lower *H/h* ratios the hinging effect is not very prominent. This is because a lower plate of smaller thickness will be less stiff and thus will provide less reaction force.

Variations in the normalized effective stress intensity and the normalized residual strength with respect to the crack extension $\bar{e}$ have been shown in Fig. 3.16(b) and (c). The crack trajectory and the stress intensity factor plots are quite different from that of the positive moment loading case (see Figs. 3.7 and 3.8). In this case the opening is on the opposite side (left), and the crack trajectories at both the tips are downwards due to the effect of negative moment. Careful inspection of the right crack trajectory shows that it initially propagates upward and then changes direction and extends downwards. This is due to the stresses caused by the hinging effect in the initial stages. Due to the change in the propagation angle of the right crack tip, the residual strength is affected and thus it shows some variation in the initial steps. A little bump can be seen on the effective stress intensity factor at the left tip in Fig. 3.16(a) in the initial stages. The increase in the

(a)

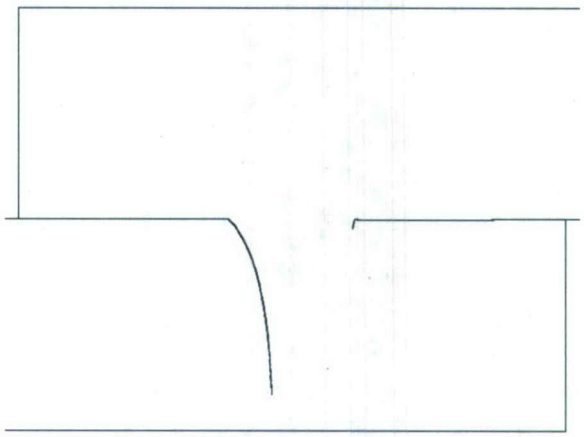

(b)

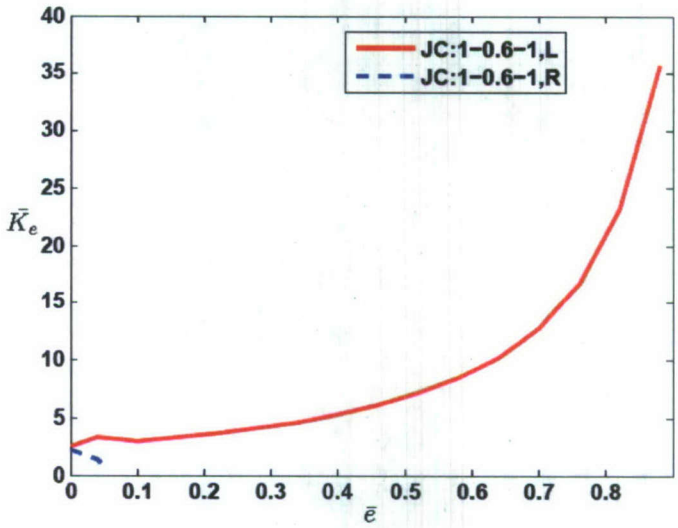

(c)

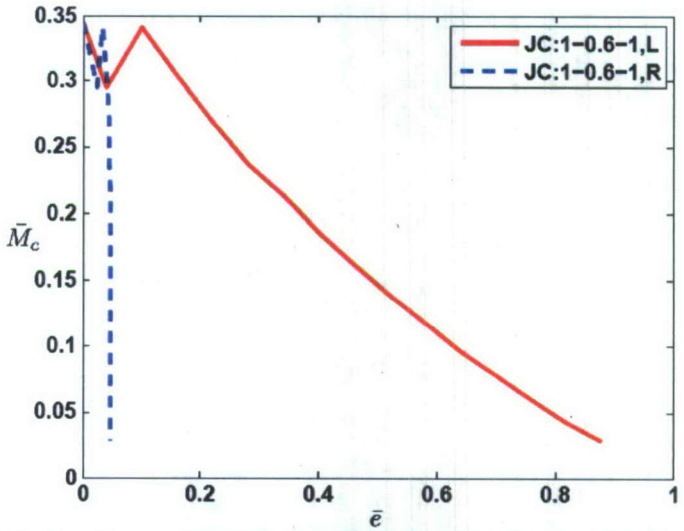

Figure 3.16: (a) Crack propagation trajectory, (b) Normalized effective stress intensity factor and (c) Normalized residual strength vs. normalized crack extension $\bar{e}$, under a M^- load in the joint geometry JC:1-0.6-1.

effective stress intensity factor at the left tip during the initial steps is due to the changes in the mode-II stress intensity factor. Since after a certain crack extension, the propagation becomes more and more mode-I, the K_{II} effects recede and the curve smoothens.

Figure 3.17(a) shows the left and right crack extensions as a function of the normalized number of cycles. It is seen that the left crack rapidly grows and reaches the lower boundary when $\bar{N} = 0.002$. The corresponding fatigue life curve is given in Fig. 3.17(b). A comparison of $\bar{N}$ at maximum crack extension from Figs. 3.10 and 3.17(a) shows that the direction of the moment load has a significant effect on the fatigue life of the joint. The fatigue life N of the joint under a negative moment is 77.3% smaller than when it is subjected to a positive moment of identical cyclic moment amplitude.

The converged normalized number of cycles obtained from Fig. 3.17(a), is again utilized to predict the fatigue life of the joint. For this purpose, the normalized negative moment amplitude $\Delta\bar{M}$ applied on the joint is plotted against actual number of cycles N to failure of the joint, on a log scale. Fig. 3.17(b) simply explains that if a certain amount of $\Delta\bar{M}$ is applied on the joint, then the joint will fail in the corresponding number of cycles based on the plot.

(a)

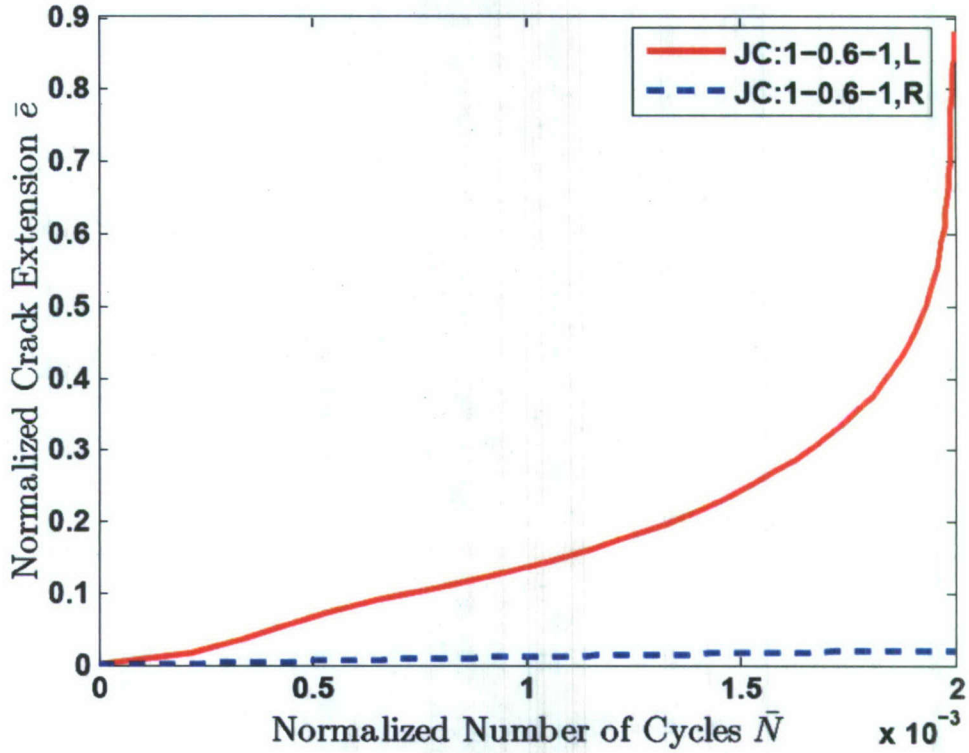

(b)

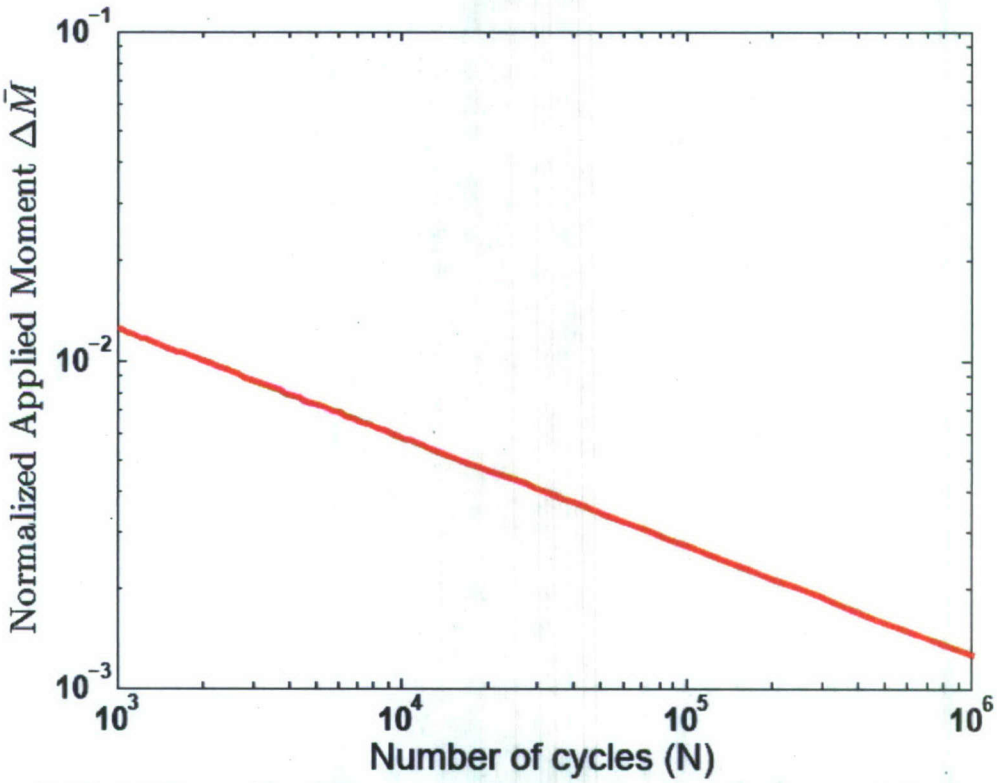

Figure 3.17: (a) Normalized N-e curves for the left and right tips, and (b) Log-log $\Delta\bar{M}$-N plot, for negative moment amplitude, for the joint JC:1-0.6-1.

3.7.2.2 Joint Configuration (JC:2.5-0.2-1)

A detailed joint model with dimensions $H/h = 2.5$, $w/h = 0.2$ and $a/h = 1$ is made and meshed in CASCA. Fig. 3.18(a) illustrates the crack trajectory for this model. It can be seen that the crack propagates through the weld, presenting a fairly complicated crack propagation trajectory. One has to be careful when choosing the maximum crack increment $\Delta\bar{e}$ during the crack propagation analysis. If the increment is too small, the analysis will require an excessive number of elements while if the increment is too large the trajectories are very coarse and it leads to the premature intersection of the two crack boundaries.

Normalized values of effective stress intensity factor history and residual strength with respect to normalized crack extension are plotted for each step in Fig. 3.18(b) and (c). Fig. 3.18(b) shows that the effective stress intensity factor is higher at the left tip during the initial steps.

The normalized residual strength at $\bar{e} = 0$ in this case, is found a little higher than the previous joint case JC:1-0.6-1. By comparing Fig. 3.18(c) and Fig. 3.16(c), one can say that at a fixed $a/h = 1$, increasing H/h produces a joint of higher strength although the weld-width w/h is smaller. Conversely, the smaller the weld length of the joint, the more significant drop is seen in its strength with crack growth.

For the joints under negative moment amplitude, e.g. JC:1-0.6-1, some amount of hinging effect has been seen. This effect becomes more prominent with either an increase in the non-welded overlap length or decrease in the welded length. This is explained with a reference of another joint JC:2.5-0.2-1 and its $\bar{N} - \bar{e}$ plot shown in Fig. 3.19(a). The curves shown in Fig. 3.19(a) and Fig. 3.17(a), clearly shows the effect of hinging

(a)

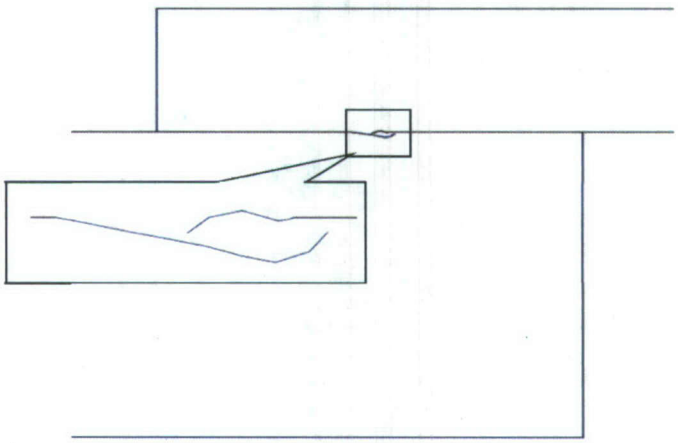

(b)

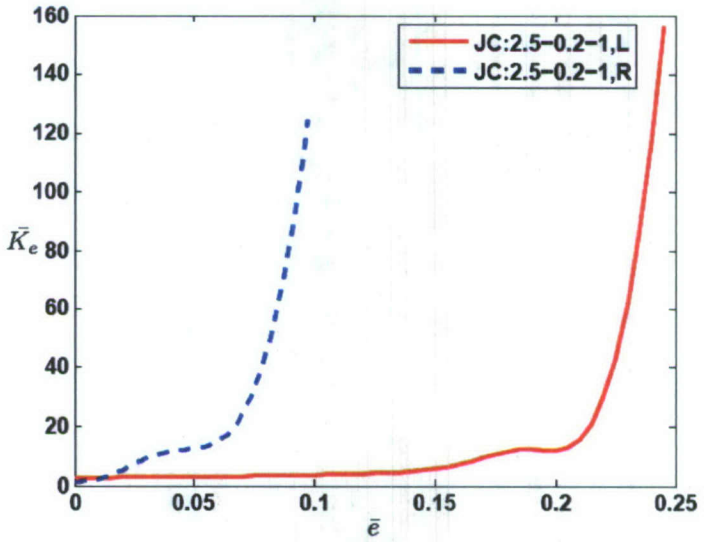

(c)

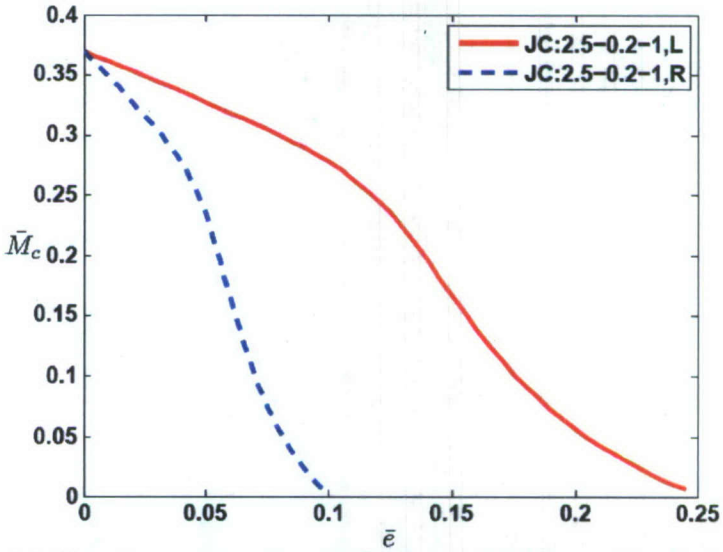

Figure 3.18: (a) Crack propagation trajectory, (b) Normalized effective stress intensity factor and (c) Normalized residual strength vs. normalized crack extension $\bar{e}$, under a M^- load in the joint geometry JC:2.5-0.2-1.

(a)

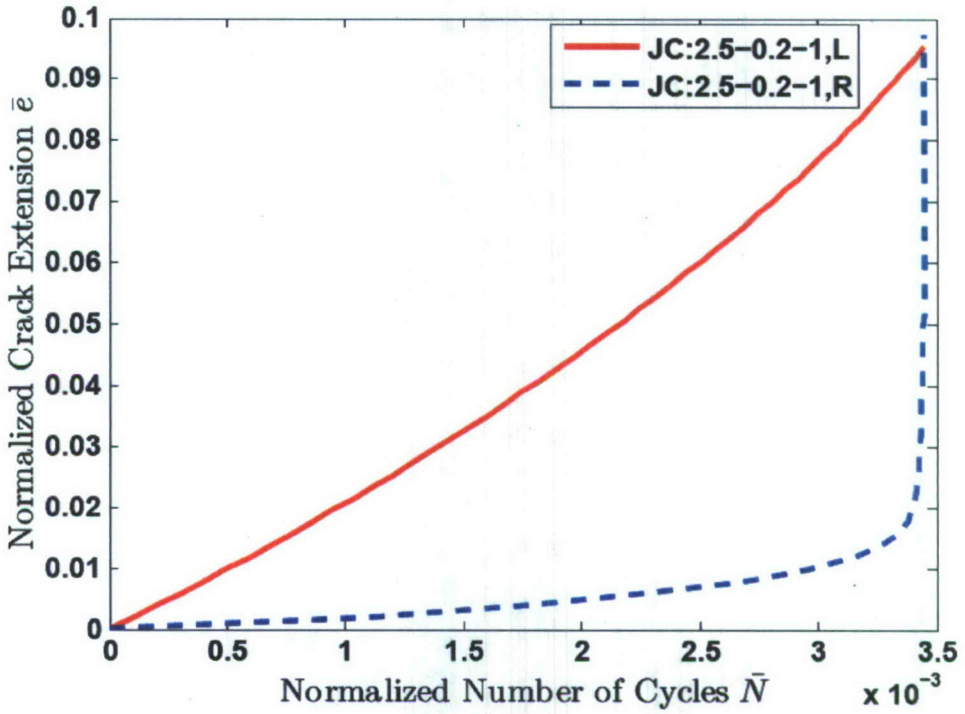

(b)

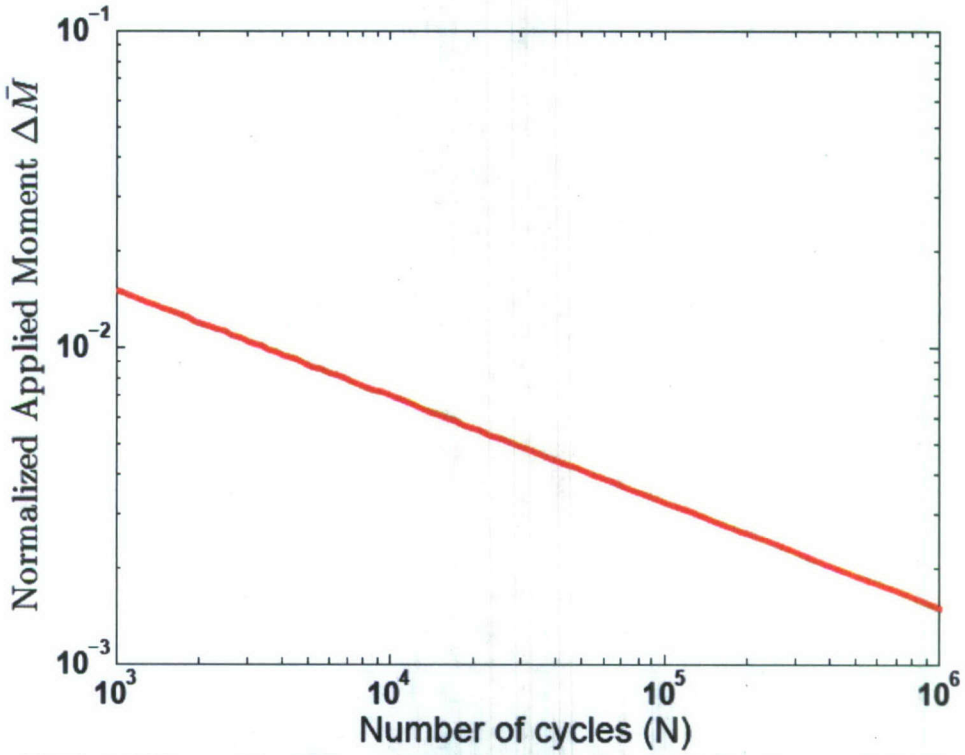

Figure 3.19: (a) Normalized N-e curves for the left and right tips, and (b) Log-log $\Delta\bar{M}$-N plot, for negative moment amplitude, for JC:2.5-0.2-1.

mechanism in both the negative moment cases. In Fig 3.17(a), the left notch propagated at a faster rate due to comparatively smaller non-welded and higher welded length. While in Fig. 3.19(a), right notch showed a higher growth rate due to high stress concentration as a result of hinging.

Fig. 3.19(b) shows the fatigue life prediction of joint JC:2.5-0.2-1. The end point of the line is defined as fatigue endurance limit of the joint. This means that the crack will not grow at any applied load below the lowest point of the line. By comparing the fatigue life plots of the two joint in this loading case, one can say that by increasing the *H/h* ratio the fatigue endurance limit of the joint increased. However, it did not increase significantly due to the reduced welded length. Therefore, it is worth adding here that JC:2.5-0.6-1 under negative moment amplitude has 70% higher fatigue life than JC:1-0.6-1.

3.7.3 Loading Case-III (Positive Tension, P^+)

Referring to the future goal of the study, if the bolted and riveted joints in a ship structure are to be replaced with laser welded joints, then, it would be desirable to understand the behavior of the joint under a tensile load. Keeping this in mind, a study has been conducted to investigate crack growth under a tensile load.

3.7.3.1 Common Joint (JC:1-0.6-1)

On the common joint-geometry (JC:1-0.6-1) a constant distributed axial load is applied at the overhang edge of the upper plate. With a power value of 3, and 16 steps of propagation, the crack trajectory obtained is almost the same as shown in Fig. 3.16(a). However, they are not identical. This is because in this case, no crack propagation is seen

on the right notch (Fig. 3.20(a)), which explains that hinging effect is really seen only in the negative moment cases.

The normalized K_{eff} and normalized M_c plots shown in Fig. 3.20(b) and (c) are for left notch of the joint JC:1-0.6-1. Corresponding normalized *N-e* curve and fatigue life plots are shown in Fig. 3.21(a) and (b). These plots are self explanatory.

(a)

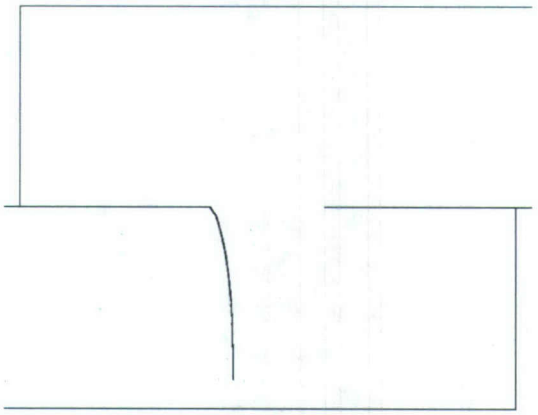

(b)

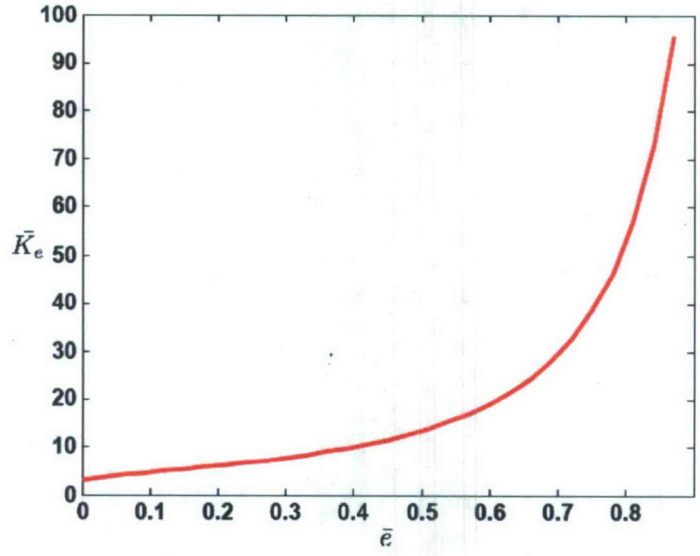

(c)

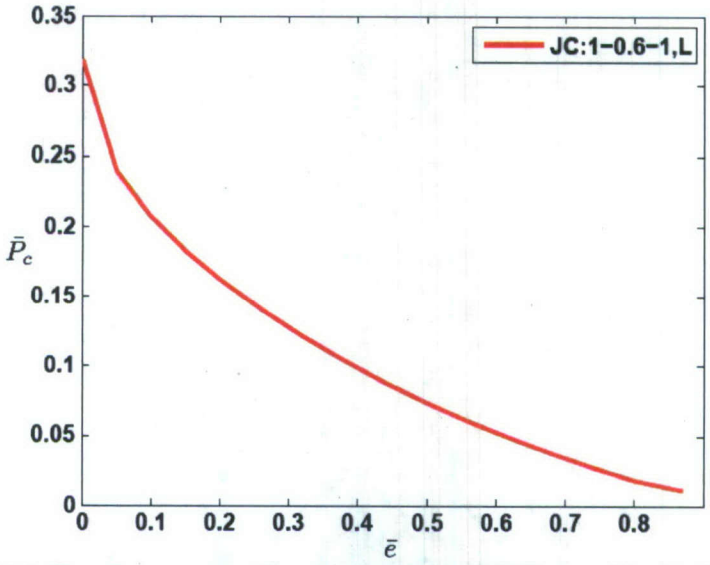

Figure 3.20: (a) Crack propagation trajectory, (b) Normalized effective stress intensity factor and (c) Normalized residual strength vs. normalized crack extension $\bar{e}$ at the left notch, under a P^+ load in the joint geometry JC:1-0.6-1.

(a)

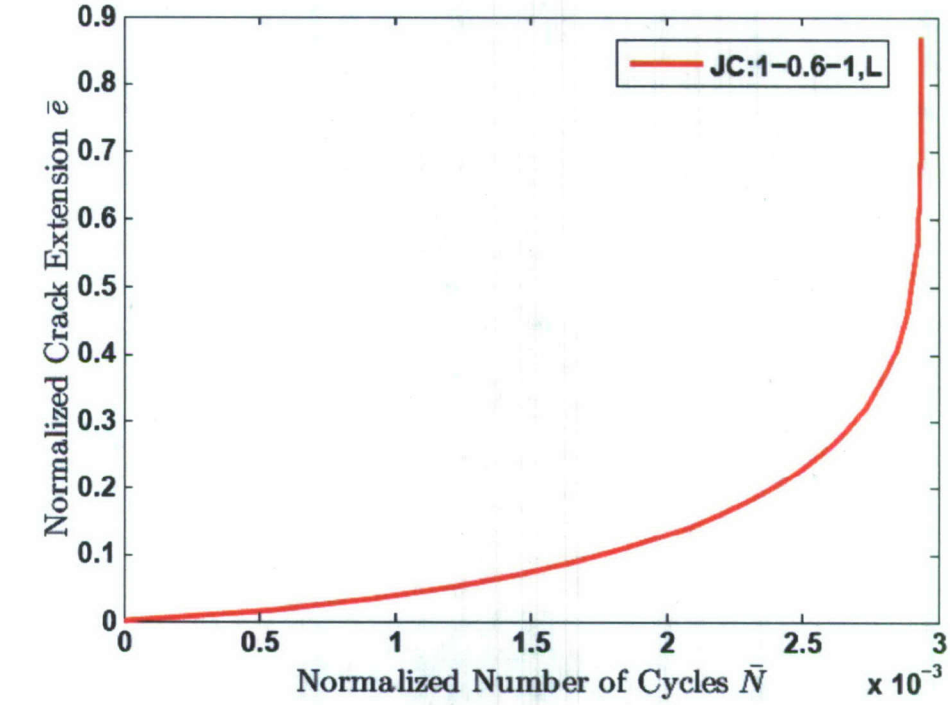

(b)

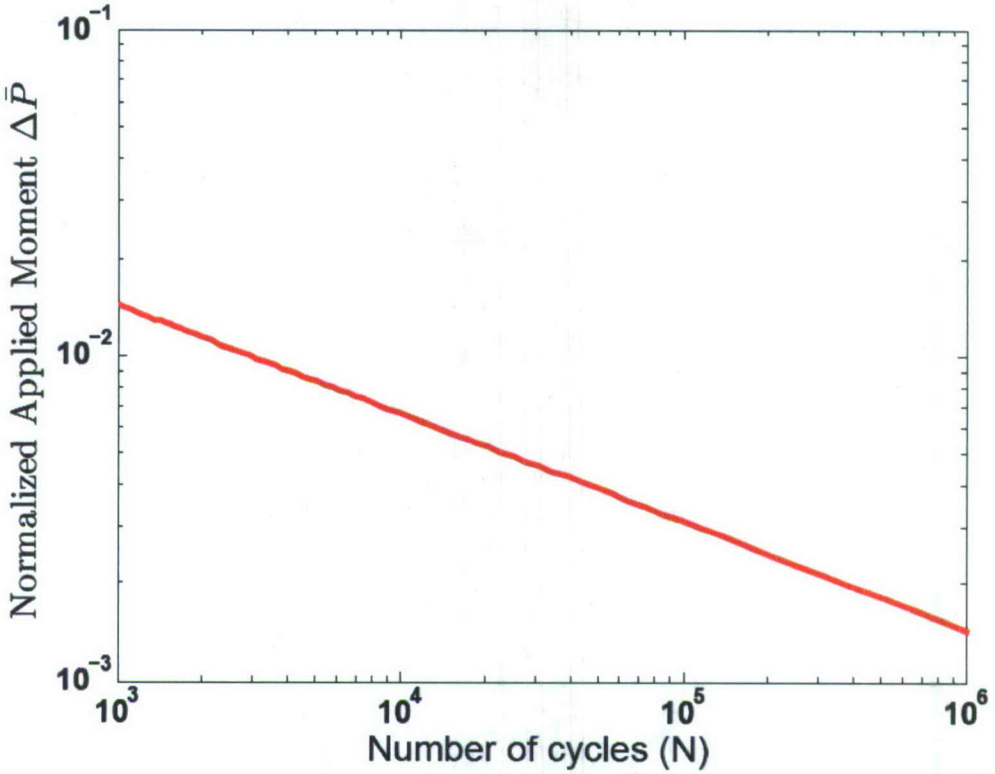

Figure 3.21: (a) Normalized N-e curves for the left tip, and (b) Log-log $\Delta\bar{M}$-N plot, under tensile force amplitude, for JC:1-0.6-1.

3.7.3.2 Joint Configuration (JC:2.5-0.2-1)

Another joint type is considered for this loading case in order to check the effect of varying *w/h* and *H/h* on, the crack trajectory, the stress intensity factor and the critical load, for an applied tensile load. Fig. 3.22(a), show the crack trajectory for the joint JC:2.5-0.2-1. It is observed that, although, effective stress intensity factor values at both the notches in this case are quite close, the cup and cap trajectory obtained here is really the effect of decrease and then increase in the mode-II stress intensity factor, which affected the crack propagation angle too. It can be seen that for a smaller *w/h* ratio, even if the lower plate is kept thick, the crack propagates through the weld when the specimen is subjected to a tensile load. The variation in the normalized effective stress intensity factor and the normalized residual strength for this joint with respect to the crack extension, have been shown in Figs. 3.2(b) and (c). As plotted earlier, the red color lines depict the left and blue depicts the right notches for the joint geometry. It is interesting to note that there comes a propagation step when both the crack tips have nearly the same effective stress intensities. At that step the crack increments calculated for both the crack tips are almost the same.

Fig. 3.23(a) and (b) shows the fatigue plots of normalized number of cycles versus normalized crack extension, and normalized applied tensile force amplitude versus actual number of cycles to complete failure of the joint, respectively. There is not much difference in the fatigue life of the two joint types under this loading case, but the one with higher *H/h* ratio can bear more number of cycles at the same applied load.

(a)

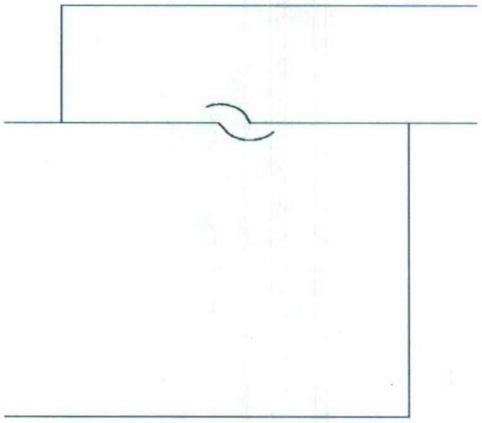

(b)

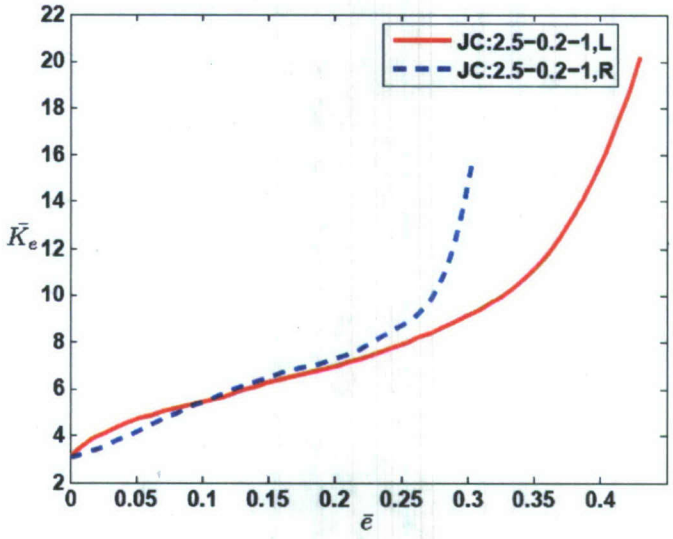

(c)

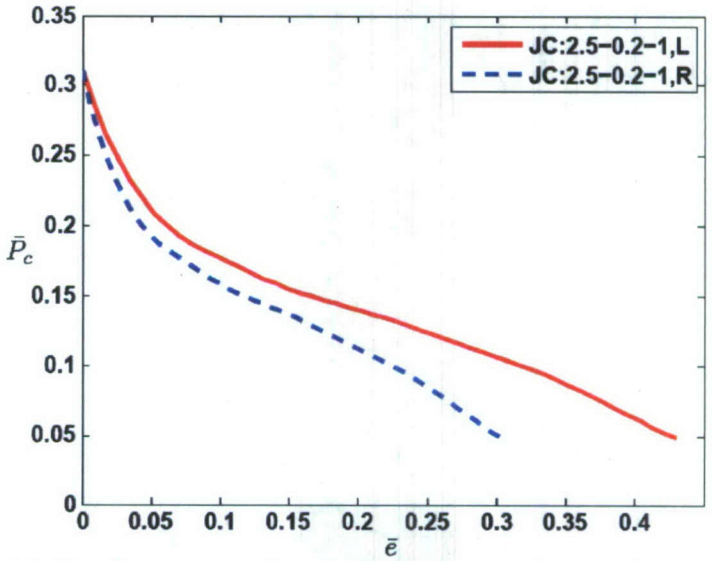

Figure 3.22: (a) Crack propagation trajectory, (b) Normalized effective stress intensity factor and (c) Normalized residual strength vs. normalized crack extension $\bar{e}$, under a P^+ load in the joint geometry JC:2.5-0.2-1.

(a)

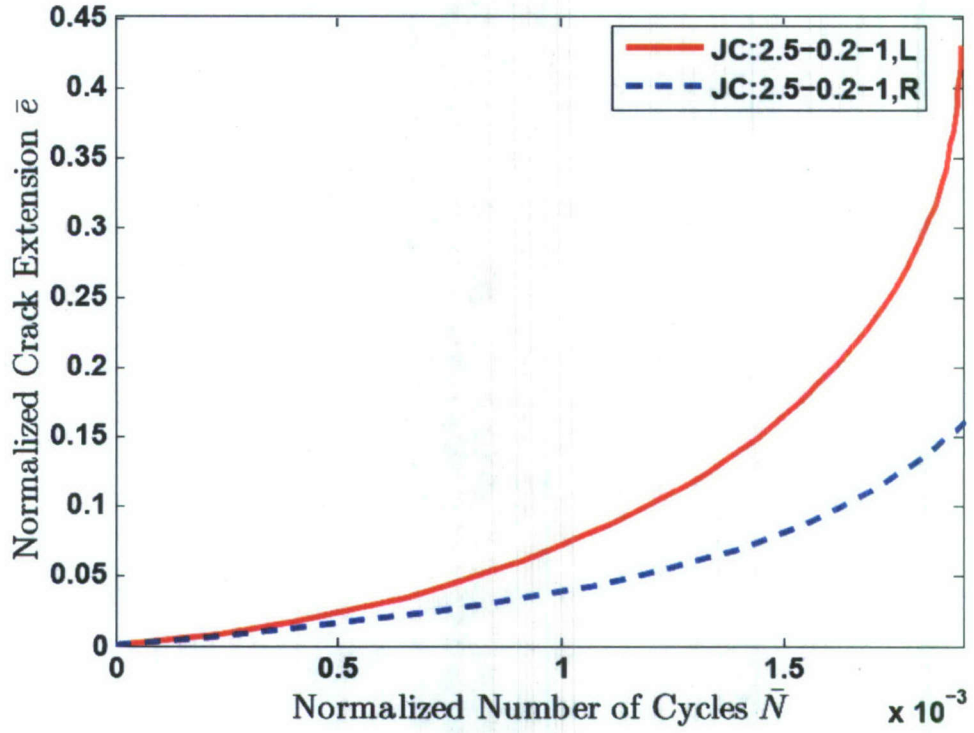

(b)

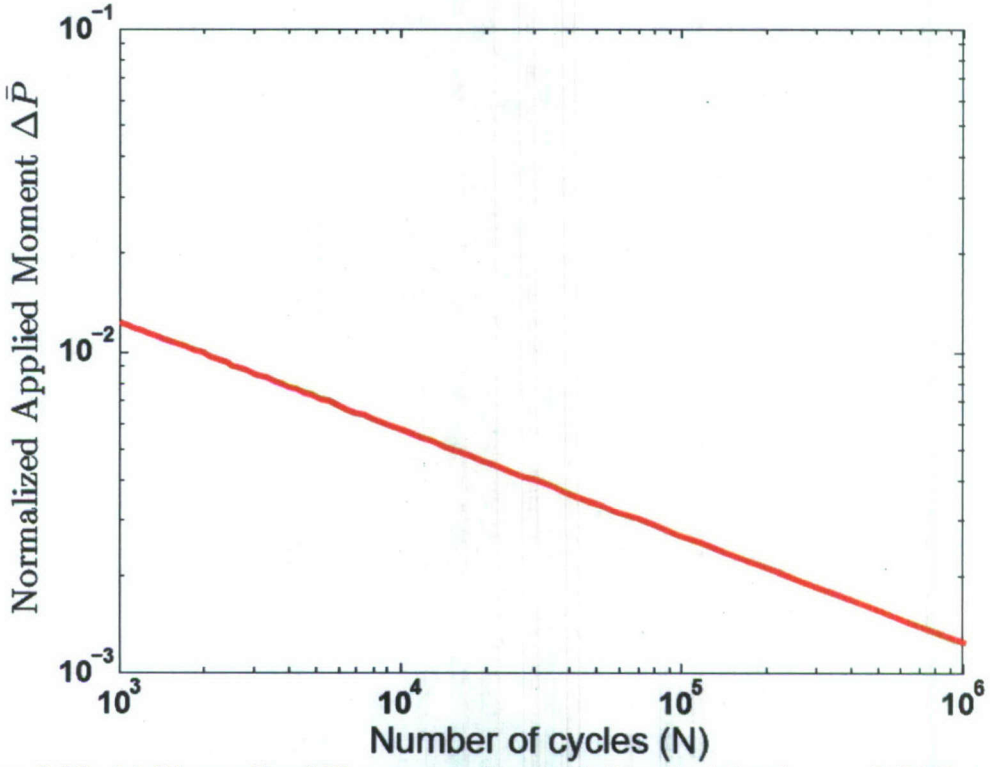

Figure 3.23: (a) Normalized N-e curves for the left and right tips, and (b) Log-log $\Delta\bar{M}$-N plot, for tensile force amplitude.

3.8 Joint Case Studies

An effort has been done in the previous sections to elaborate on the variation of stress intensity factors, residual strength and number of cycles with crack extension, but the results are presented in a non-dimensional form that can be applied to a variety of joint configurations. Two case studies are performed in this section to elucidate on the implementation of those results and get some data for practical applications. Designers are interested in the residual strength and/or fatigue life of a structure. In continuation, it is also desirable to know the residual strength of the joint after it has been subjected to a certain number of cycles under a prescribed cyclic load magnitude.

The first case study is performed on the joint model JC:1-0.6-1 with a repeated cyclic load (ΔM^{+}) where $M_{min} = 0$. It is assumed that the joint is made of steel with $C = 3.6 \times 10^{-10}$, $m = 3$, $K_{Ic} = 109$ ksi$\sqrt{\text{in}}$, $\Delta K_{th} = 5$ ksi$\sqrt{\text{in}}$ and it has an upper plate thickness of h = 0.25". The Paris law constants C and m used in the following case studies correspond to that of a mild steel (Barsom 1971). The output of the codes used for fatigue plots, is used to generate a plot of residual strength versus normalized number of cycles. Fig. 3.24 contains a plot of the residual strength of the joint versus the normalized number of cycles. The plot points out the minimum and maximum residual strength of the joint ($M_c^{min} = 0.269$ and $M_c^{max} = 4.639$ kips-in/in) at zero and maximum crack extensions at one of the notches. It is interesting to see that the plot shows some hardening effects up to certain $\bar{N}$ which corresponds to a certain crack extension, after which the strength of the joint drops almost linearly. The little peak in the residual strength plot experienced here, has been referenced back to the crack propagation analysis section of this chapter, and it

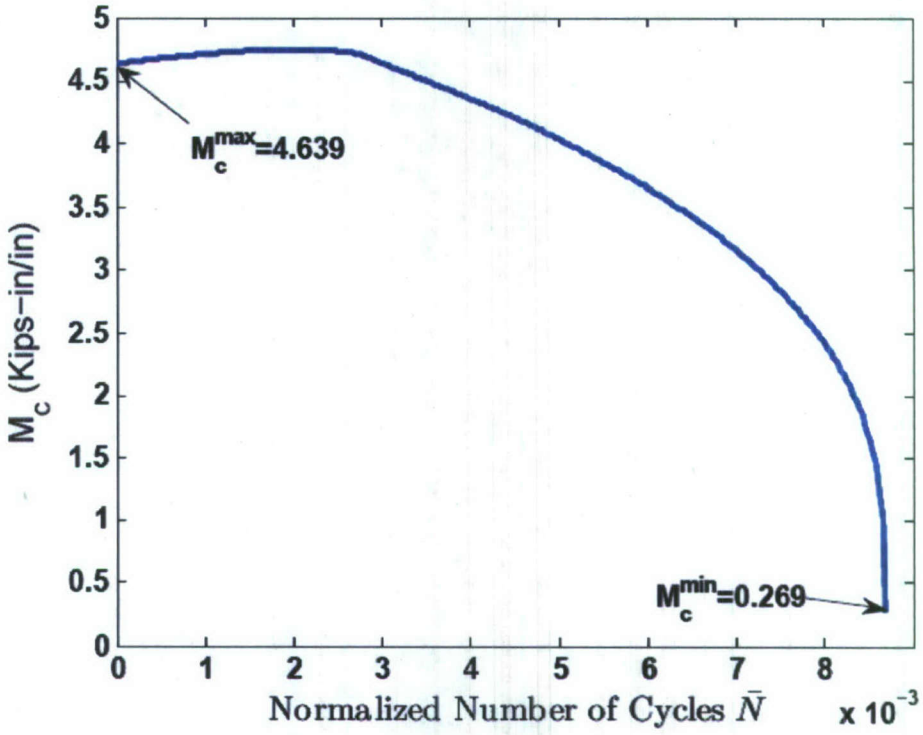

Figure 3.24: Normalized number of cycles versus strength left in the joint JC:1-0.6-1 for an applied positive moment amplitude.

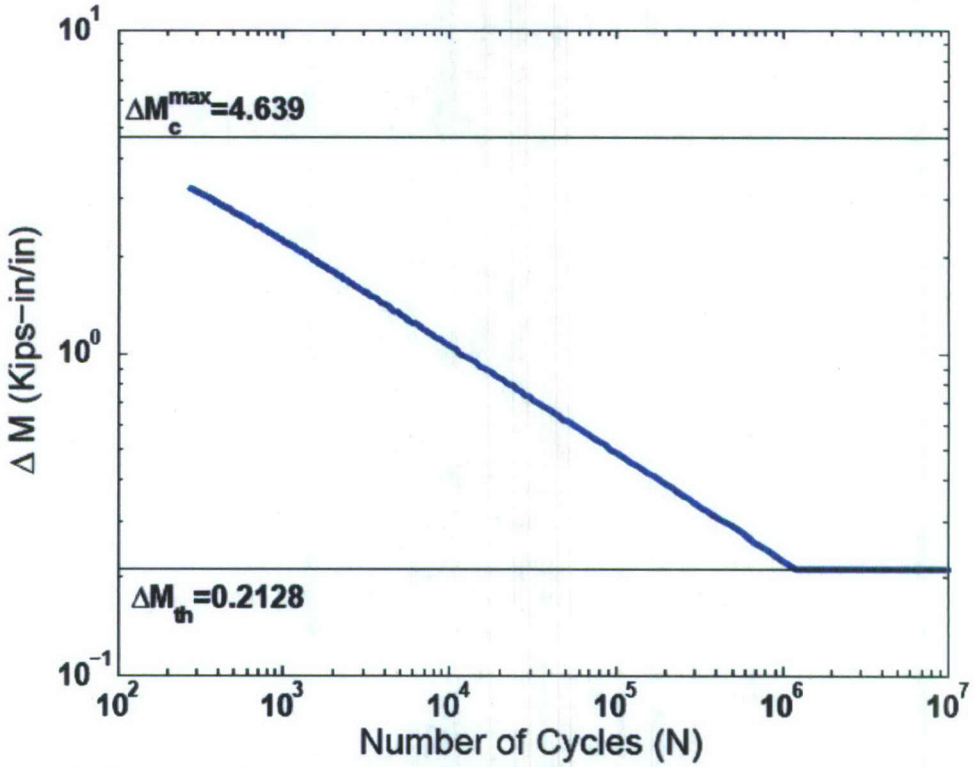

Figure 3.25: Applied moment amplitude vs. number of cycles for JC:1-0.6-1, considering failure of the structure.

is observed that this peak is a result of the large mode-II stress intensity factor at the very first step of crack propagation.

A plot of moment amplitude versus number of cycles ΔM-N is considered as a major result of any fatigue life analysis. It has been experimented and mentioned many times in the literature that ΔM-N plot for steel shows an 'L' shape, if broader range of applied moments and number of cycles to failure are considered. This essentially means that there is a fatigue endurance limit of the structure below which it will not fail for any number of cycles. An attempt has been made to relate this plot to the sigmoidal curve discussed above. For a better representation of Region-II of the sigmoidal curve shown in Fig. 3.6, it is required to define the lower and upper limits of the applied load amplitude. Critical moment or residual strength calculations have already been done to get the upper limit of the Region-II of the sigmoidal curve. The threshold load $\Delta M_{threshold}$ = 0.2128 kips-in/in is evaluated using Maximum Tensile Stress Criterion and ΔK_{th} of the material. Several moment amplitudes are applied on the model between $\Delta M_{threshold}$ and some 30% below ΔM_c^{max}, and number of cycles to failure of the joint is recorded, as shown in the Fig. 3.25. For fatigue analysis applied loads are not carried up to the critical value, but are kept below that value. The curve mimics the S-N curve for any other arbitrary specimen and is meant for the failure of the structure and not for the failure of the material.

The second design study is performed on JC:2.5-0.2-1 joint with tensile load P^+. An upper plate thickness h = 0.25" is used and same formulation and code is used, except using $h^{m/2}$ instead of $h^{3m/2}$ for normalized quantities in the moment cases. The output obtained by running the code are illustrated in Fig. 3.26(a) and (b).

(a)

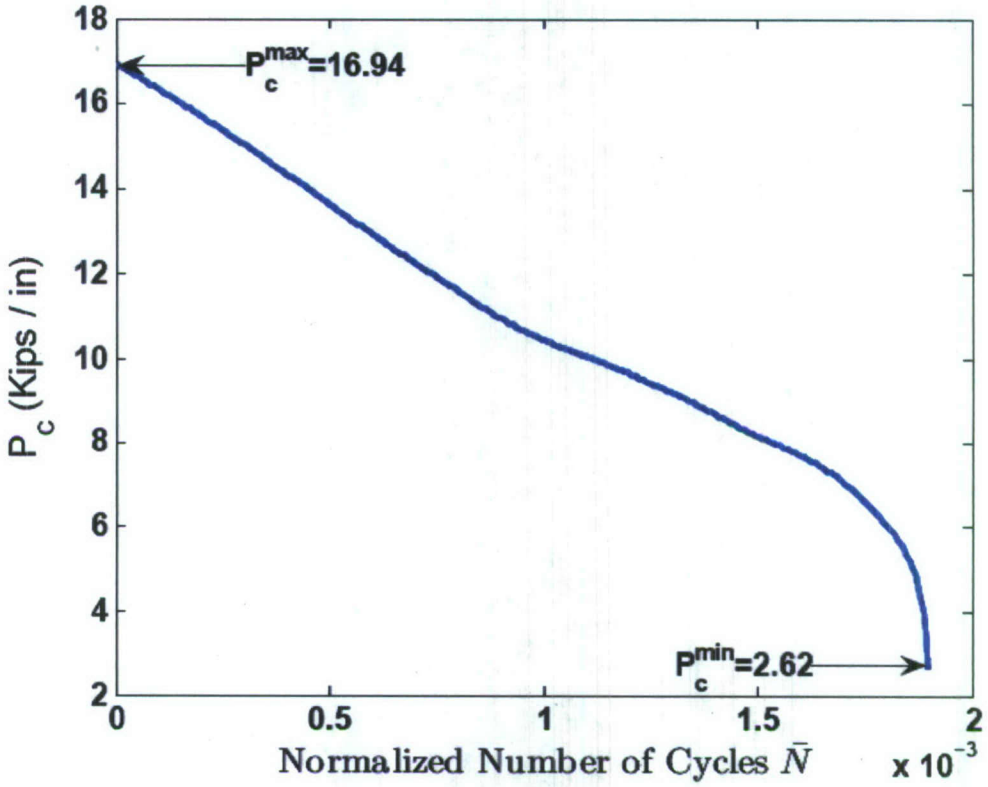

(b)

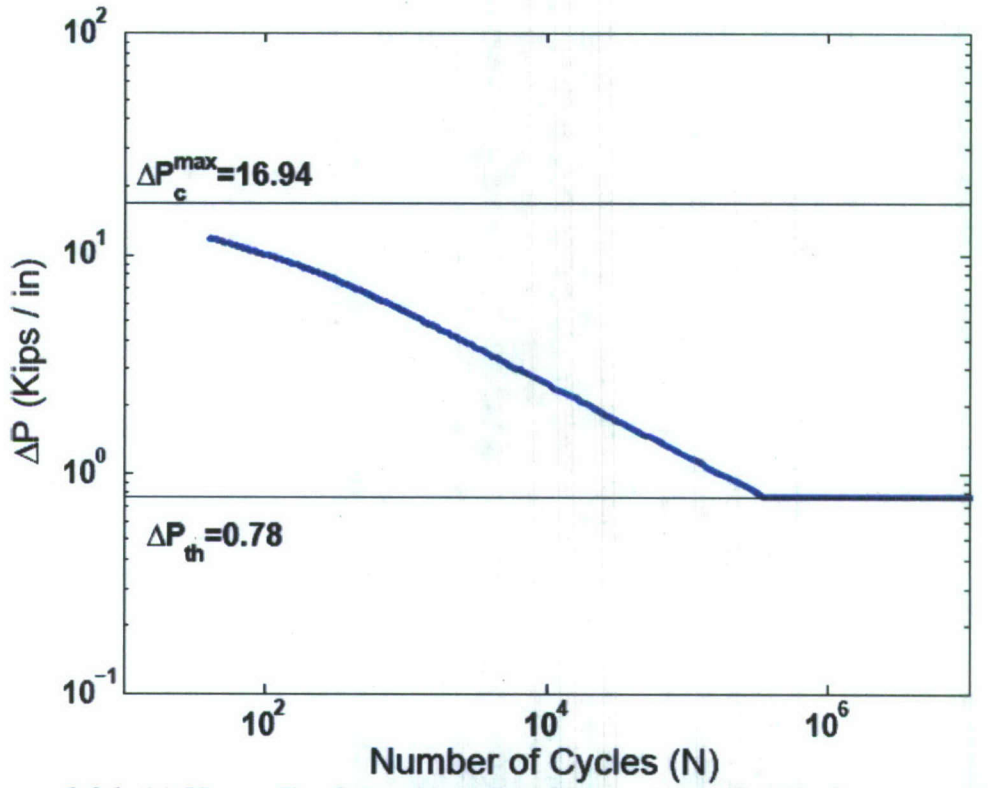

Figure 3.26: (a) Normalized number of cycles vs. strength left , for an applied tensile force amplitude (b) Applied tensile force amplitude vs. number of cycles to failure of the joint JC:2.5-0.2-1.

3.9 Conclusions

In this chapter, the finite element code FRANC2D is used to analyze the crack growth trajectories of different joint configurations and to compute the fatigue life by performing fatigue analysis of those joints under different loads. It is observed that for different joint configurations under different types of loading conditions, the crack trajectories are significantly different. Some situations are harder to explain, especially where there are crack growths at both the notch tips. In such conditions, one crack starts growing towards another which significantly affects the stress intensity around the other crack. These different trajectories also explain that the same joint behaves differently under different loading conditions, and therefore a crack trajectory of any stake connection cannot be predicted for any arbitrary load. However, one can say that the crack would always tend to grow through the weld when the weld-width is small.

The manual crack propagation gives better control over the operation of the program. In performing a manual propagation, one can keep the power value constant (which according to the multiple-crack fatigue crack growth method is really the material constant m) and compute the increments at each crack tip. The crack incrementation has been kept above a tolerance of 0.002, which means the crack is not propagated if the increment calculation gives below 0.002 for a crack tip. For the geometries like the one studied here, mixed mode stress intensity factors are required to be considered. Therefore, referring to the power law crack growth model, the stress intensity factor amplitude ΔK is considered as a mixed mode parameter ΔK_{eff}. The above computed increments are then supplied to the program to get new crack tips. The analysis is then

run with dynamic relaxation algorithm for a tolerance of $1x10^{-4}$, and stress intensities are recomputed at the new crack tips.

The method discussed above, to generate the normalized plots, would turn out to be very handy when a designer would have to compute the strength, number of cycles it can withstand and the fatigue life, of a joint, which already has some crack growth. For example, if a structure with n cracks is considered and the total crack extension at any of the crack tips in that structure is measured, then with the help of $\bar{M}_c - \bar{e}$ and $\bar{N} - \bar{e}$ plots, it will be easy to compute the residual strength of the structure and the maximum number of cycles it can withstand.

For fatigue analysis six joint configurations are analyzed using FRANC2D. A simple form of fatigue evaluation is done without experiments, all based on numerical methods by using *Paris Law*. In an attempt to visualize the performance of the joints under a broad range of applied loads, maximum and threshold values are also considered. By assuming a threshold value of the stress intensity factor (ΔK_{th} = 5% of ΔK_c), applied threshold load amplitude (ΔM_{th}) is computed. These maximum and threshold values are utilized to predict the fatigue life of each joint configuration considered. It also helped in explaining that the crack will not grow at low loads, and thus defines the fatigue endurance limit of a particular joint under consideration. Two joint case studies are performed to clarify the normalization concept carried over throughout the chapter. These case studies develop a better understanding of converting the normalized results into practical use.

It has been seen in the literature (Anderson, 1995) that for more ductile materials, stress intensity approach would not be too appropriate and that ΔK in the *Paris Law*

needs to be replaced by ΔJ (a J-integral amplitude load). To add to this, before applying ΔJ, one may realize that the joint geometries discussed in this study produces mixed-mode crack propagation conditions. This area has a great potential for current and future research.

REFERENCES

ABAQUS/Standard documentation, 2005, version **6.6**, Abaqus Inc., RI.

Agrawal A., Karlsson A.M., 2006, Obtaining Mode Mixity for a Bimaterial Interface Crack using the Virtual Crack Closure Technique, *International Journal of Fracture*, **141**:75-98.

Anderson T.L., 1995, Fracture Mechanics: Fundamentals and Applications - second edition, *CRC Press Inc.*

Barsom J.M., 1971, Fatigue-Crack Propagation in Steels of Various Yield Strengths, *Journal of Engineering for Industry*, Transactions of ASME, Series **B**: 1190-1196.

Broek D., 1978, Elementary Engineering Fracture Mechanics, *Sijthoff & Noordhoff.*

Caccese V., Blomquist P.A., Berube K.A., Webber S.R., Orozco N.J., 2006, Effect of weld geometric profile on fatigue life of cruciform welds made by laser/GMAW processes", *Marine Structures*, **19**:1-22

Carmignani C., Mares R., Toselli G., 1999, Transient Finite Element Analysis of Deep Penetration Laser Welding Process in a Singlepass Butt-welded Thick Steel Plate, *Computer Methods in Applied Mechanics and Engineering*, **179**: 197-214.

Cao J., Grenestedt J.L., 2003, Test of a redesigned glass-fiber reinforced vinyl ester to steel joint for use between a naval GRP superstructure and a steel hull, *Composite Structures*, **60**: 439-445.

Cho S.K., Yang Y.S., Son K.J., Kim J.Y., 2004, Fatigue Strength in Laser Welding of the Lap Joint, *Finite Elements in Analysis and Design*, **40**:1059-1070.

Clifford S.M., Manger C.I.C., Clyne T.W., 2002, Characterization of a glass-fiber reinforced vinylester to steel joint for use between a naval GRP superstructure and a steel hull, *Composite Structures*, 57: 59-66.

Erdogan F., and Sih G.C., 1963, On the crack extension in plates under plane loading and transverse shear, *ASME Journal of Basic Engineering*, **85**, 519-527.

Fang H., Rais-Rohani M., Liu Z., Horstemeyer M.F., 2005, A Comparative Study of Metamodeling Methods for Multiobjective Crashworthiness Optimization, *Computers and Structures*, **83**:2121-2136.

Foreman R.G., Keart V.E. and Engle R.M., 1967, Numerical analysis of crack propagation in cycle-loaded structures, *Journal of Basic Engineering, ASME* **89**, pp. 459–464.

Gdoutos E.E., 2005, Fracture Mechanics an Introduction, Second Edition, *Springer*.

Gowhari-Anaraki A.R., Hardy S.J., Alipour R., 2005, Spot-welded Joints Subjected to Shear-tension Loading. Part 2: Mixed-mode Fracture Parameters, *Journal of Strain Analysis*, **40**: 755-774.

Griffith A.A., 1920, The Phenomena of Rupture and Flow in Solids, *Philosophical transactions*, Series **A**, Vol.**221**, pp 163-198.

Holland J., 1975, Adaptation in Natural and Artificial Systems, *University of Michigan Press*, Ann Arbor.

Hsu C., Albright C.E., 1991, Fatigue Analysis of Laser Welded Lap Joints, *Engineering Fracture Mechanics*, Vol 39, **3**:575-580.

Inglis C.E., 1913, Stresses in a Plate Due to the Presence of Cracks and Sharp Corners, *Transactions of the Institute of Naval Architects*, Vol. **55**, pp 219-241.

Irwin G.A, Paris P.C., Tada H., 1985, The Stress Analysis of Cracks Handbook, *Del Research Corporation*, Bethlehem, PA.

Irwin G.R., 1956, Onset of Fast Crack Propagation in High Strength Steel and Aluminum Alloys, *Sagamore Research Conference Proceedings*, Vol. 2, pp. 289-305.

Jin R., Chen W. and Simpson T.W., 2001, Comparative studies of metamodeling Techniques under Multiple Modeling Criteria, *Structural and Multidisciplinary Optimization*, 23, 1-13.

Krishnamurthy T, 2003, Response surface approximation with augmented and compactly supported radial basis functions, The 44th AIAA/ASME/ASCE/AHS/ASC structures, structural dynamics, and materials conference, Norfolk, VA.

Krueger R., 2002, The Virtual Crack Closure Technique: History, Approach and Applications, *NASA ICASE Report no. 2002-10, Langley Research Center, Virginia.*

Melograna J.D., Grenestedt J.L., 2002a, Adhesion of stainless steel to fiber reinforced vinyl ester composite, *Journal of Composites Technology & Research*, **24**:254-260.

Melograna J.D., Grenestedt J.L., 2002b, Improving joints between composites and steel using perforations, *Composites: Part A – Applied Science and Manufacturing*, **33**: 1253-1261.

Paris P.C. and Erdogan F., 1960, A Critical Analysis of Crack Propagation Laws, *Journal of Basic Engineering*, Vol. **85**, pp. 528-534.

Qian J., Fatemi A., 1996, Mixed Mode Fracture Crack Growth: A Literature Survey, *Engineering Fracture Mechanics*, Vol **55**, No. **6**, pp. 969-990.

Rice J.R., 1968, A Path Independent Integral and the Approximate Analysis of Strain Concentration by Notches and Cracks, *Journal of Applied Mechanics*, Vol. **35**, pp. 379-386.

Rybicki E.F., Kanninen M.F., 1977, A Finite Element Calculation of Stress Intensity Factors by a Modified Crack Closure Integral, *Engineering Fracture Mechanics*, **9**:931-938.

Smith I., Landis E., Gong M., 2003, Fracture and Fatigue in Wood, *John Wiley & Sons Ltd.*

Sumpter J.D.G., 1996, Fracture Toughness of Laser Welds in Ship Steel, *Advanced Performance Materials*, **3**:393-405.

Sun C.T., 2001, Fracture Mechanics, School of Aeromautics and Astronautics, *Purdue University*, West Lafayette, Indiana.

Suo Z., Hutchinson J.W., 1990, Interface Crack between Two Elastic Layers, *International Journal of Fracture*, **43**: 1-18.

Terasaki T., Kitamura T., 2004, Prediction of Static Fracture Strength of Laser welded Lap joints by Numerical Analysis, *Welding International*, Vol 18, No.7, pg.524-530.

Unden H., Ridder S.O., 1985, Load introducing armature as a component part of a laminated structural element, US Patent 4,673,606; 13 February 1985.

Wells A.A., 1961, Unstable Crack Propagation in Metals: Cleavage and Fast Fracture, *Proceedings of the Crack Propagation Symposium*, Vol. 1, Paper **84**, Cranfield, UK.

Westergaard H.M., 1939, Bearing Pressures and Cracks, *Journal of Applied Mechanics*, Vol. 6, pp. 49-53.

Yan X., 2007, Automated simulation of fatigue crack propagation for two-dimensional linear elastic fracture mechanics problems by boundary element method, *Engineering Fracture Mechanics*, **74**: 2225-2246.

Zalzala A.M.S., Fleming P.J., 1997, Genetic Algorithms in Engineering Systems, *The Institution of Electrical Engineers –London.*

Zhang X.R., Xu X., 2004, Finite Element Analysis of Pulsed Laser Bending: The Effect of Melting and Solidification, *Journal of Applied Mechanics*, **71**:321-326.

REPORT DOCUMENTATION PAGE

Form Approved
OMB No. 0704-0188

PLEASE DO NOT RETURN YOUR FORM TO THE ABOVE ADDRESS.

1. REPORT DATE *(DD-MM-YYYY)*	2. REPORT TYPE	3. DATES COVERED *(From - To)*
30-06-2008	Project Report	1-Jan-2006 to 31-Dec-2007

4. TITLE AND SUBTITLE

Design Optimization and Fatigue Analysis of Laser Stake Welded Connections

5a. CONTRACT NUMBER

5b. GRANT NUMBER

N00014-05-1-0735

5c. PROGRAM ELEMENT NUMBER

6. AUTHOR(S)

Singh, Anshuman
Vel, Senthil S.
Caccese, Vincent

5d. PROJECT NUMBER

5e. TASK NUMBER

5f. WORK UNIT NUMBER

7. PERFORMING ORGANIZATION NAME(S) AND ADDRESS(ES)

University of Maine
Office of Research and Sponsored Programs
5717 Corbett Hall
Orono, ME 04469-5717

8. PERFORMING ORGANIZATION REPORT NUMBER

C-2004-015-RPT-02

9. SPONSORING/MONITORING AGENCY NAME(S) AND ADDRESS(ES)

Office of Naval Research
Ballston Center Tower One
800 North Quincy St.
Arlington, VA 22217-5660

10. SPONSOR/MONITOR'S ACRONYM(S)

ONR

11. SPONSORING/MONITORING AGENCY REPORT NUMBER

12. DISTRIBUTION AVAILABILITY STATEMENT

Approved for Public Release, Distribution is Unlimited

13. SUPPLEMENTARY NOTES

14. ABSTRACT

This report summarizes research on the design and fatigue analysis of laser-stake welded connections performed at the University of Maine from January 2006 to December 2007 for the Structural Response of Hybrid Ship Connections Subjected to Fatigue Loads (HSCF) project.

Laser welding is a maturing technology that can be used to fabricate metal/composite hybrid connections wherein modular composite panels with embedded steel inserts are welded to a steel ship hull. The static and fatigue response of continuous laser welded steel connections for ship structures has been analyzed using finite element techniques. The stress analyses, which are based on the principles of linear elastic fracture mechanics, will enable engineers to design robust laser welded lap joints for prescribed loads. It is found that the overlap length, weld width and plate thicknesses play a major role in determining joint strength under different loading conditions. The fatigue response of laser welded lap joints is also investigated for different weld geometries and loading conditions using a fracture specific finite element program FRANC2D. It is found that the weld width has a significant effect on the crack trajectory and fatigue life of the joint.

15. SUBJECT TERMS

Hybrid Structures; Laser-stake Welding; Connection Design; Fatigue Response, Finite Element Analysis; Fracture Mechanics, Optimization of Connections

16. SECURITY CLASSIFICATION OF:			17. LIMITATION OF ABSTRACT	18. NUMBER OF PAGES	19a. NAME OF RESPONSIBLE PERSON
a. REPORT	b. ABSTRACT	c. THIS PAGE			Vincent Caccese
U	U	U	UU	145	19b. TELEPONE NUMBER *(Include area code)* (207) 581-2131

Standard Form 298 (Rev. 8-98)
Prescribed by ANSI-Std Z39-18